

**Investigating Frozen Ground Dynamics by
Using Global Navigation Satellite System
Interferometric Reflectometry**

ZHANG, Jiahua

A Thesis Submitted in Partial Fulfilment
of the Requirements for the Degree of
Doctor of Philosophy
in
Earth and Atmospheric Sciences

The Chinese University of Hong Kong
August 2021

Thesis Assessment Committee

Professor CHAN Man Nin (Chair)

Professor LIU Lin (Thesis Supervisor)

Professor YANG Hongfeng (Committee Member)

Abstract

of thesis entitled:

Investigating Frozen Ground Dynamics by Using Global Navigation Satellite System Interferometric Reflectometry

Submitted by ZHANG, Jiahua

for the degree of Doctor of Philosophy

at The Chinese University of Hong Kong in August 2021

The ground surface in a permafrost region is subject to uplift/subsidence, due to freezing/thawing of the active layer. Thus, surface elevation changes are closely linked with frozen ground dynamics. The Global Navigation Satellite System interferometric reflectometry (GNSS-IR) has been emerging as a new technique to measure surface elevation changes in permafrost areas. It can also estimate snow depth and surface soil moisture. Currently, a large number of GNSS stations have been continuously operating in permafrost areas. However, not all of them are suitable for GNSS-IR studies, as this technique requires the ground surface to be open and relatively horizontal and smooth. Moreover, only one site, i.e., SG27 in Utqiagvik, Alaska, was assessed to be suitable for using GNSS-IR to measure surface elevation changes. Furthermore, the commonly-used GNSS-IR algorithm for estimating soil moisture has not been evaluated in permafrost areas.

In this thesis, we screened the major GNSS networks and identified 23 suitable

sites from 186 in the Arctic permafrost areas. Most of them are located in northern Canada and Alaska, and a few are scattered in the Eurasian permafrost areas. We also obtained their reflector heights by GNSS-IR, which can be converted into surface elevation changes in snow-free seasons, otherwise snow depth.

We used the GNSS-IR-estimated vertical surface movement at Alert, Resolute Bay, Repulse Bay, Baker Lake, and Iqaluit in the Canadian Arctic to investigate their multi-year linear trends. The ground surface underwent subsidence at these sites, except Repulse Bay, whose trend was not statistically significant. We also found that Alert, Resolute Bay, and Baker Lake had warming thawing seasons. It implies that the subsidence at these three sites was possibly caused by near-surface permafrost degradation induced by warming air temperatures. On the contrary, Iqaluit had cooling summers. The impact of air temperature at this site might be moderated by other environmental variables, such as vegetation, soil moisture, and ground ice near the permafrost table. Therefore, Iqaluit still underwent subsidence in cooling thawing seasons.

In Resolute Bay, the end-of-thaw elevations were highly and negatively correlated with the square-root-of thawing indices during 2003–2012, whereas they were low in 2013 and 2014 with cool summers. The change of the correlation sign in 2013 and 2014 was postulated to be caused by the variations in soil properties and ground ice content near the permafrost table triggered by the extremely warm summer in 2011. Due to such changes, the heat still could penetrate into the deep frozen ground to cause large seasonal subsidence and low end-of-thaw elevations in 2013 and 2014.

In Utqiagvik, Alaska, by comparing seasonal subsidence with the square-root of thawing index, we found that their slope was $0.43 \pm 0.04 \text{ cm}\cdot(\text{ }^{\circ}\text{C}\cdot\text{day})^{-1/2}$ during 2004–2008, whereas $0.18 \pm 0.01 \text{ cm}\cdot(\text{ }^{\circ}\text{C}\cdot\text{day})^{-1/2}$ during 2009–2018. We hypothesized that this significant change was caused by the active layer drying and followed changes in the soil thermal properties. In situ measurements of soil moisture content validated it by showing a decreasing trend in the soil down to 35 cm depth during

2004–2008 and keeping the relatively dry state during 2009–2016.

We also improved the commonly-used GNSS-IR algorithm for estimating surface soil moisture in permafrost areas, by introducing modeled surface elevation changes to mitigate the biases introduced by the seasonal surface vertical deformation. We validated our method by using the SNR data and in situ observations at a permafrost site QLBG in the northeastern Qinghai-Tibet Plateau (QTP). As a result, the root mean square error and correlation coefficient between the GNSS-IR estimates and the in situ ones improved from 1.85% to 1.51% and 0.71 to 0.82, respectively. We also proposed a three-in-one framework to integrate the GNSS-IR estimates of surface elevation changes, soil moisture, and snow depth at one site and illustrated it by using QLBG as an example.

This thesis provides numerous usable GNSS sites, filling some spatial gaps of the existing permafrost monitoring programs and providing the GNSS-IR measurements to complement the core observations, such as active layer thickness and ground temperature. The multi-year, continuous, and daily GNSS-IR measurements contribute to quantifying frozen ground dynamics and providing new insights. The improved GNSS-IR algorithm helps to estimate soil moisture in permafrost regions reliably. The three-in-one framework can be extended to other suitable sites, such as the ones in the Arctic.

摘要

全球多年冻土在过去的几十年一直在变暖。多年冻土的退化对地貌、水文、生态和基础设施产生严重的影响。由于活动层的冻结/融化，多年冻土区域的地面可能会隆起/下沉。因此，地表高程变化和冻土的内在变化机制有着紧密的关联。全球导航卫星系统干涉反射法 (GNSS interferometric reflectometry, GNSS-IR) 是近年来出现的一种利用直接信号和反射信号之间的干涉图样来估算环境变量的技术。它可以用米来测量地表高程变化、雪深和地表土壤湿度。

目前，多年冻土区域有大量的 GNSS 连续运行观测站。由于 GNSS-IR 要求站点周围的环境开阔无遮挡且地面相对平坦，所以并非所有的站点都适合于应用 GNSS-IR。另外，截至本论文前，只有一个站点，即位于 Utqiagvik, Alaska 的 SG27，应用 GNSS-IR 测量地表高程变化来研究多年冻土。此外，用于估算地表土壤水分的 GNSS-IR 算法在多年冻土区的效果尚未经过评估。

在本文中，通过检查全球主要的 GNSS 网，我们从位于北极多年冻土区域的 186 个站点中识别出 23 个适合于应用 GNSS-IR 的站点。其中，大多数站点位于加拿大北部和阿拉斯加，还有一些分散在欧亚大陆的多年冻土区域。我们还获得了它们的天线高数据，这些数据可以转化为地表高程变化和雪深。

基于连续逐日的 GNSS-IR 数据，我们计算了加拿大北极地区 Alert、Resolute Bay、Repulse Bay、Baker Lake 和 Iqaluit 地表高程变化的多年线性趋势。除了 Repulse Bay 无显著变化之外，其他站点都出现了下沉。我们还发现 Alert, Resolute Bay 和 Baker Lake 的融化季节在变暖。这意味着它们的地表沉降可能是由于气

温升高引起的多年冻土退化造成的。相反，Iqaluit 的融化指数呈降低趋势。在该地，气温对于多年冻土的影响可能受到其他环境变量（例如植被、土壤湿度）的调节。因此，即便融化指数在下降，地表也出现下沉趋势。

在 Resolute Bay，融化季末期的地面高程和融化指数的平方根于 2003–2012 年呈高度负相关；而在融化指数较低的 2013 和 2014 年，融化季末期的地面高程也比较低。于 2013–2014 年出现的相关性改变的这种现象可能是由于 2011 年极端炎热的夏季触发的活动层土壤性质和近地表多年冻土的冰含量的变化所致。由于这些变化，热量仍然可能传递到深层冻土中，导致较大的季节性沉降和较低的地表高程。

在 Utqiagvik，季节性沉降与融化指数的平方根的比率在 2004–2008 年期间为 $0.43 \pm 0.04 \text{ cm} \cdot (\text{°C} \cdot \text{day})^{-1/2}$ ，而在 2009–2018 年期间为 $0.18 \pm 0.01 \text{ cm} \cdot (\text{°C} \cdot \text{day})^{-1/2}$ 。这一显着变化可能是由活动层土壤湿度下降及由此引起的土壤热学性质改变而引起的。基于实测数据，我们发现，在活动层深至 35cm 的土壤中，土壤含水量在 2004–2008 年间呈现出下降趋势，在 2009–2016 年间保持相对干燥的状态。

我们还改进了常用于估算表层土壤湿度的 GNSS-IR 算法。将模拟的地表高程变化引入常用的算法可以消除多年冻土区域可能会出现的季节性偏差。我们使用位于青藏高原东北部的站点 QLBG 的 SNR 数据和实测数据验证我们的方法。GNSS-IR 估算的土壤含水量与实测数据的均方根误差从 1.85% 降至 1.51%，相关系数从 0.71 提高到了 0.82。此外，我们还提出了一个三合一的框架：在一个 GNSS 站点上利用 GNSS-IR 测量地表高程变化、土壤湿度和积雪深度；并以站点 QLBG 为例进行说明。

本文提供了适合于应用 GNSS-IR 的多个站点，这些站点可以填补现有多年冻土监测网难以覆盖的区域。这些站点所提供的 GNSS-IR 数据可以作为多年冻土核心观测值（例如活动层厚度和地温）的补充。多年连续逐日的 GNSS-IR 数据有助于量化多年冻土的变化并提供关于冻土变化机制的新见解。改进的 GNSS-IR 算法有助于可靠地估算多年冻土地区的表层土壤湿度。我们所提出的三合一框架可以应用到其他合适的站点，例如北极地区的可用站点。

Acknowledgement

First of all, I would like to thank my supervisor, Prof. Liu, for providing me the opportunity to work with him and on this interesting project. In this four-year journey, I have grown a lot in not only the knowledge of permafrost and GNSS reflectometry but the courage for exploring and the resilience and perseverance for facing failures. I cannot make it without the patience and guidance of Prof. Liu. He has always done his best to keep me thinking positively and focusing on the big picture.

I am very thankful for my collaborators, Drs. Yufeng Hu, Tao Che, Lei Su, Kang Wang, Tingjun Zhang, and Mr. Guanxin Wang. Thanks for the support you have provided, the insightful discussion we have had, and the fieldworks we have conducted.

Next, I thank my current and past colleagues – Xiyu Chen, Enze Zhang, Yan Hu, Carol Xingyu Xu, Summer Zhuoxuan Xia, Billy Ho Ming Tsang, Lingcao Huang, Jie Chen, Jiangjun Ran, Kenneth Ho, Bao Zhang. Thank you for creating a professional, inspiring, and lively atmosphere in our office. I have enjoyed the time with you.

This research would not have been possible without the fundings and support from the Chinese University of Hong Kong, Hong Kong Research Grants Council (CUHK14305618), and National Science Foundation of China.

Contents

Abstract	i
摘要	iv
Acknowledgement	vi
Contents	vii
List of Figures	xi
List of Tables	xviii
Symbols and Acronyms	xix
1 Introduction	1
1.1 Permafrost	1
1.2 Ground surface elevation changes in permafrost areas	3
1.2.1 Ground surface elevation changes	3
1.2.2 Stefan equation	5
1.3 GNSS-IR	6
1.3.1 Principles	8
1.3.2 Signal-to-noise ratio (SNR)	10
1.3.3 Converting SNR metrics into environmental variables	11

1.3.4	Merits and limitations	15
1.4	Contributions	16
1.5	Roadmap	18
2	Suitable sites in the Arctic permafrost areas for GNSS-IR studies	19
2.1	Introduction	19
2.2	Methodology	21
2.2.1	A framework to identify usable sites in permafrost areas	21
2.2.2	GNSS networks	22
2.3	Results	24
2.4	Discussion	31
2.4.1	Error sources of the GNSS-IR measurements of surface elevation changes	31
2.4.2	Merits of usable sites and their GNSS-IR measurements	35
2.4.3	Limitations of the suitable sites in non-continuous permafrost areas	36
2.5	Conclusion	38
3	Investigating frozen ground dynamics in the Canadian Arctic by GNSS-IR-estimated surface elevation changes	40
3.1	Introduction	40
3.2	Study sites	41
3.3	Results	46
3.4	Discussion	53
3.4.1	Multi-year linear trends of surface elevation changes	53
3.4.2	Seasonal surface elevation changes	55
3.4.3	End-of-thaw elevations in Resolute Bay	64
3.5	Conclusion	66

4 A moist-to-dry shift of active layer during 2004–2018 in Utqiagvik, Alaska revealed by GNSS-IR-estimated seasonal subsidence	68
4.1 Introduction	68
4.2 Study site	71
4.3 Methodology	72
4.3.1 Seasonal subsidence estimated by GNSS-IR	72
4.3.2 The ratio between seasonal subsidence and square-root-of thawing index	74
4.4 Results	74
4.5 Discussion	76
4.5.1 A moist-to-dry shift of the active layer from 2004–2008 to 2009–2018	76
4.5.2 Limitations of surface elevation changes in revealing permafrost degradation/aggradation	79
4.6 Conclusion	81
5 Improving the GNSS-IR algorithm for estimating surface soil moisture in permafrost areas	83
5.1 Introduction	83
5.2 Study site	85
5.3 Improving the default algorithm of estimating soil moisture	86
5.3.1 Limitation of the default algorithm	86
5.3.2 Solution of introducing modeled surface elevation changes	88
5.3.3 Data	90
5.4 Results	91
5.4.1 Ground surface elevation changes	91
5.4.2 Validation of the improved method and soil moisture	92
5.4.3 Snow depth	94

5.5	Discussion	95
5.5.1	Monument stability	95
5.5.2	Error sources of the improved method	99
5.5.3	Impact of surface reflectivity on snow depth	101
5.5.4	Benefits of the three-in-one framework	103
5.6	Conclusion	104
6	Conclusion	105
6.1	Contributions	105
6.2	Future work	108
6.2.1	Supersites for monitoring permafrost areas	108
6.2.2	Synergy between GNSS-IR and SAR/InSAR	111
A	Output	115
A.1	Publication	115
A.2	Conference paper and presentation	116
A.3	Data	117
	Bibliography	118

List of Figures

1.1	Permafrost distribution in the Northern Hemisphere based on Brown et al. (1997). The type of permafrost zonation is indicated by variously shaded colors of blue.	2
1.2	Schematic diagram of the GNSS-IR geometry of the receiver antenna, reflecting surface, direct signal, and reflected signal. We draw the image antenna with respect to the ground surface and the image propagation path of the reflected signal for clarifying its additional path. We use the symbols, including V , S , P , and V' , to denote the vertical positions of antenna, ground surface, monument anchor point, and image antenna, respectively. H is the vertical distance between antenna and surface. e is the satellite elevation angle.	9
1.3	(a) Time series of SNR observations corresponding to the satellite track of GPS PRN02 on DOY 18 in 2017 recorded by the GNSS station BAKE in Baker Lake, Canada. (b) The residuals after removing the high-order polynomial fit of the SNR observations. The dashed rectangles mark the observations at low elevation angles, which have sinusoidal shapes.	11

1.4	(a) SNR interferograms within the azimuth range of 90–180 degrees on DOY 210 in 2019 recorded by SG27 in Utqiagvik, Alaska. The red sine curve is created by using the average values of the dominant frequencies, amplitudes, and phases of the SNR series. (b) Frequency spectrums of the SNR interferograms. The frequency has been converted into reflector height. The red vertical line is the mean value of the reflector heights with peak amplitudes. The scale of SNR data has been converted from dB to volts/volts.	13
1.5	Schematic diagram showing the reflector heights in snow-cover and snow-free conditions. The snow depth is the difference between the reflector height in snow-season (H_{snow}) and the one for ground (H_{snow}) as reference.	15
2.1	(a) A ground photo of SG27 in Utqiagvik, Alaska. (b) A piece of SNR interferogram at the satellite elevation angles of 5–20° recorded by SG27. The second-order polynomial fit of the SNR observations has been removed. (c) and (d) are similar to (a) and (b) correspondingly but for YELL in Yellowknife, Canada. The monument heights of SG27 and YELL are marked as well.	22
2.2	Locations of the open-data GNSS sites in the Arctic permafrost areas north of 50° N.	25
2.3	Percentages of the unsuitable sites for the causes, including obstruction, undulated surface, and insufficient SNR interferogram.	31
2.4	Tropospheric biases of the GNSS-IR-estimated surface elevation changes in Resolute Bay in the thawing season (i.e., DOY 192–250) of 2014. They are the mean values of the tropospheric biases of all satellite tracks. Their standard deviations are indicated by error bars.	33

2.5	Locations of the identified usable GNSS sites in the Arctic permafrost areas. We also present the CALM and TSP sites.	37
3.1	Ground photos of the GNSS sites of ALRT, RESO, REPL, BAKE, and IQAL.	42
3.2	SNR observations and their corresponding LSP spectrums at ALRT, RESO, REPL, BAKE, and IQAL. The frequency has been converted into reflector height. The red vertical line denotes the mean value of the dominant reflector heights with peak amplitudes.	43
3.3	Time series of surface elevation changes in Alert, Resolute Bay, Repulse Bay, Baker Lake, and Iqaluit. For each site, the reference is the mean value of the measurements over the entire data time span. We also present the best linear fits of the measurements and their slopes for each site.	47
3.4	Surface elevation changes in each thawing season with the reference as their mean value during 2012–2018 in Alert.	48
3.5	Similar to Fig. 3.4 but for Resolute Bay.	49
3.6	Similar to Fig. 3.4 but for Repulse Bay.	50
3.7	Similar to Fig. 3.4 but for Baker Lake. Data gaps exist in 2011 and 2013.	51
3.8	Similar to Fig. 3.4 but for Iqaluit.	52
3.9	Scatter plot of surface elevation changes versus square-root-of thawing indices in each thawing season during 2012–2018 in Alert. We also build their best linear fits as dashed lines and show their correlation coefficients (R) and slopes.	56
3.10	Similar figure to Fig. 3.9 but for Resolute Bay.	57
3.11	Similar figure to Fig. 3.9 but for Repulse Bay.	58
3.12	Similar figure to Fig. 3.9 but for Baker Lake.	59
3.13	Similar figure to Fig. 3.9 but for Iqaluit.	60

3.14 Average seasonal variations of surface elevations (as red dots) at each Canadian Arctic site. The black lines refer to the 10-day moving averages.	62
3.15 Comparison between average seasonal surface elevation changes and average normalized square-root-of thawing indices at each Canadian Arctic site. The correlation coefficients are presented as well.	63
3.16 (a) Time series of end-of-thaw elevations and square-root-of thawing indices during 2003–2014 in Resolute Bay. (b) Scatter plot between end-of-thaw elevations and \sqrt{DDT} during 2003–2014. (c) Similar plot to (b) but for measurements during 2003–2012. The correlation coefficient and root mean square error (RMSE) are presented as well.	65
3.17 Ground temperatures at the depths of 0.5 m, 1.0 m, and 1.5 m between June 2008 and June 2012 in Resolute Bay. We mark that the ground temperature at 1.0 m depth was warmer than 0 °C in 2011.	66
4.1 (a) The geological location of SG27 in Alaska. Permafrost zonation categories are indicated by variously shaded colors of blue (Brown et al., 1997). (b) A digital elevation map at the site of SG27. The dashed-outlined fan delineates the coverage of the GNSS-IR measurements. (c) A photo shows the locations of SG27 and U1-1. (d) A ground photo of SG27. This figure is modified from Liu and Larson (2018).	73
4.2 (a) Time series of seasonal subsidence and \sqrt{DDT} during 2004–2020. (b) Scatter plot of seasonal subsidence versus \sqrt{DDT} during 2004–2020. The correlation coefficient and slope of the linear regression line with the unit of $\text{cm} \cdot (\text{°C} \cdot \text{day})^{-1/2}$ are presented.	75

4.3	Scatter plots between seasonal subsidence and \sqrt{DDT} during (a) 2004–2008, (b) 2009–2018, (c) 2019–2020, respectively. The measurement in 2015, marked as a red dot, is excluded as an outlier. The correlation coefficient (R), slope of the linear regression line, and root mean square error (RMSE) are presented as well.	76
4.4	(a) In situ volumetric water content at 5 cm during 2004–2016. The brown solid squares and error bars represent the mean values and standard deviations of soil moisture content in each thawing season. The best linear fits of the mean values during 2004–2008 and 2009–2016 have the slopes of $-0.05 \pm 0.02 \text{ cm}^3 \cdot \text{cm}^{-3} \cdot \text{yr}^{-1}$ and $0.01 \pm 0.01 \text{ cm}^3 \cdot \text{cm}^{-3} \cdot \text{yr}^{-1}$, respectively. (b) and (c) are for in situ soil moisture content at 20 cm and 35 cm, respectively. We do not calculate the mean values of soil moisture content at 35 cm depth, as they are nearly constant during 2004–2016.	78
4.5	The ratios of DDT derived from ground temperature (DDT_{ground}) to that from air temperature (DDT_{air}) during 2004–2016 at the depths of 5, 20, and 35 cm, respectively.	80
5.1	(a) Location of the study site, Binggou, in the northeastern Qinghai-Tibet Plateau. (b) Ground photo of the GNSS station QLBG. (c) Orthophoto of the Binggou site showing the surface condition, QLBG (red triangle), and the integrated weather station. Red elliptic curves indicate the footprints of the reflected L1 GPS signals at the satellite elevation angle of 5°	87
5.2	(a) Simulated SNR with $H+d$ and their fits based on $H+d$ and H , respectively. In this simulation, H and d are fixed as 2 m and 2 cm, respectively. The inset plot shows that the phases of these two fits are different. (b) The simulated phase bias when using various d	89

5.3	(a) Presence of SNR observations of the GPS L1 C/A code recorded by QLBG. (b) SNR observations with the elevation angles of 5–15 degrees of the GPS PRN02 satellite on DOY 220 in 2018. The second-order polynomial has been removed.	91
5.4	(a) Time series of GPS-IR measurements of ground surface elevation changes and the simulated ones based on the model parameters s and d_0 in (b) during DOY 182–243 in 2018. (b) Scatter plot between the ground surface elevation changes and the normalized thermal indices and their best linear fit as a dashed line. s and d_0 are the slope and intercept of this fit line.	92
5.5	(a) Time series of the phases derived by our method during DOY 182–243 in 2018. Error bars denote their uncertainties. (b) Scatter plot between phases in (a) and in situ soil moisture and their best linear fit shown as a dashed line. The slope and intercept of the fit line are presented. We also show the correlation coefficient as R. (c) and (d) are similar to (a) and (b) correspondingly but for the results of the default method. The data gap during DOY 203–206 is due to the absence of SNR data.	93
5.6	Time series of in situ soil moisture content and those measured by (a) our method and (b) the default method. The shaded areas denote the uncertainties of GNSS-IR estimates. The RMSE and correlation coefficient are presented.	94
5.7	(a) Bar plots of snow depth measured by GNSS-IR and manually. We do not show the error bars for clarity. (b) Scatter plots of these two datasets and their best linear fit as a dashed line. We also show the correlation coefficient, RMSE, and bias.	95

5.8	Positioning observations of QLBG in the (a) north, (b) east, and (c) up directions during DOY 182–243 in 2018. They are referenced to their mean values individually.	96
5.9	Surface deformation due to (a) atmospheric loadings and (b) continental hydrological loadings, respectively, during DOY 182–243 in 2018. They are referenced to their mean values individually.	97
5.10	(a) Time series of the vertical monument movement during DOY 182–243 in 2018. Their best linear fit line is also presented as a dashed line with the slope of $0.003 \pm 0.004 \text{ cm}\cdot\text{day}^{-1}$. (b) Histogram of the vertical monument movements and their normal distribution fit (red curve). The mean (μ) and standard deviation (σ) of this normal fit are 0 cm and 0.42 cm, respectively.	98
5.11	Scatter plot between the square root of normalized thawing index and the vertical monument movement during DOY 182–243 in 2018. . . .	99
5.12	Tropospheric biases of surface elevation changes during DOY 182–243 in 2018. They are the mean values of the biases of all satellite tracks, whose standard deviations are represented by error bars.	101
5.13	(a) Simulated SNR observations with the reflector of wet soil (black curve) and snow (blue curve). (b) Frequency spectrums of the simulated SNR observations. The frequency has been converted into reflector height. The dominant reflector height with peak power is 2.03 m for wet soil, whereas 1.99 m for snow.	102

List of Tables

2.1	Basic information of the usable sites in the Arctic permafrost areas.	26
2.2	Mean and standard deviation of the uncertainties of the GNSS-IR measurements in July and August over the data time span at each site.	30
3.1	Basic information of the study sites.	45
3.2	Statistics of the annual DDT in Alert, Resolute Bay, Repulse Bay, Baker Lake, and Iqaluit.	54
4.1	Ratios of DDT derived from the ground temperatures (DDT_{ground}) and that from air temperatures (DDT_{air}) in each year during 2004–2016 at 5 cm, 20 cm, and 35 cm depth, respectively.	80
5.1	Key parameters for SNR simulations with surface elevation changes.	88
5.2	Parameters for SNR simulations in snow-free and snow-cover conditions.	102

Symbols and Acronyms

Specialized symbols and key acronyms are defined as follows:

θ	volumetric water content
λ	wavelength of the GNSS signal
ρ_i	density of ice
ρ_w	density of water
τ	time
ϕ	phase of the SNR oscillation
ϕ_u	phase of the received signal
Δl	additional propagation path of the reflected signal
Φ	phase offset of the reflected signal
$d(\tau)$	vertical surface deformation
e	satellite elevation angle
f	frequency of the SNR oscillation
k	wavenumber
m	a scaling factor, equal to 86400 s·day ⁻¹
n_T	n-factor, the ratio between ground surface and air temperature
u	received signal
$z(\tau)$	thawing depth
A	amplitude of the SNR oscillation
A_{signal}	amplitude of the background noise

A_u	amplitude of the received signal
D	vertical surface deformation versus square-root-of thawing index
H	reflector height
H_0	constant reflector height
H'_0	time-varying reflector height
H_{ground}	reflector height of ground surface
H_{snow}	reflector height of snow surface
K_T	thermal conductivity of the thawed soil
L	monument length
L_f	latent heat for fusion
P	vertical position of the monument anchor point
S	vertical position of the ground surface
V	vertical position of the antenna
V'	vertical position of the image antenna

CALM	Circumpolar Active Layer Monitoring
CYGNSS	Cyclone Global Navigation Satellite System
DDT	Degree Days of Thawing (thawing index)
DOY	Day Of Year
ECMWF	European Centre for Medium-Range Weather Forecasts
GLONASS	Global Navigation Satellite System
GNSS	Global Navigation Satellite System
GNSS-IR	GNSS interferometric reflectometry
GNSS-R	GNSS reflectometry
GPS	Global Positioning System
LSE	Least Square Estimation
LSP	Lomb-Scargle Periodogram
NDVI	Normalized Difference Vegetation Index
PRN	Pseudorandom Noise
QTP	Qinghai-Tibet Plateau
RINEX	Receiver Independent Exchange Format
SMAP	Soil Moisture Active Passive
SNR	Signal-to-Noise Ratio
STATSGO	State Soil Geographic Dataset
TDS-1	TechDemoSat-1
TSP	Thermal State of Permafrost
UK-DMC	UK Disaster Monitoring Constellation

Chapter 1

Introduction

1.1 Permafrost

Permafrost, alternatively called perennially frozen ground, refers to the ground whose temperature remains at or below 0 °C for at least two consecutive years. On the top of permafrost is a layer undergoing seasonal freezing and thawing, conventionally called the active layer. The permafrost usually occurs in the polar and alpine regions (e.g., Qinghai-Tibet Plateau (QTP)) with cold climates. It is underlain in nearly a quarter of the exposed land in the Northern Hemisphere (Zhang et al., 2003). Figure 1.1 shows the permafrost distribution in the Northern Hemisphere. Based on the percentage of permafrost occurrence in an area, the permafrost zonation is categorized into continuous (> 95%), discontinuous (50–95%), and sporadic (< 50%) ones. This categorization provides a first-order estimation of permafrost existence.

In the last several decades, permafrost has been observed to be warming and thawing globally, based on ground temperature measurements in boreholes (Biskaborn et al., 2019; Vasiliev et al., 2020; Zhao et al., 2020). Thawing permafrost releases the carbon previously stored in the frozen soil and leads to positive feedback between permafrost degradation and the warming climate (Schuur et al., 2015). Permafrost

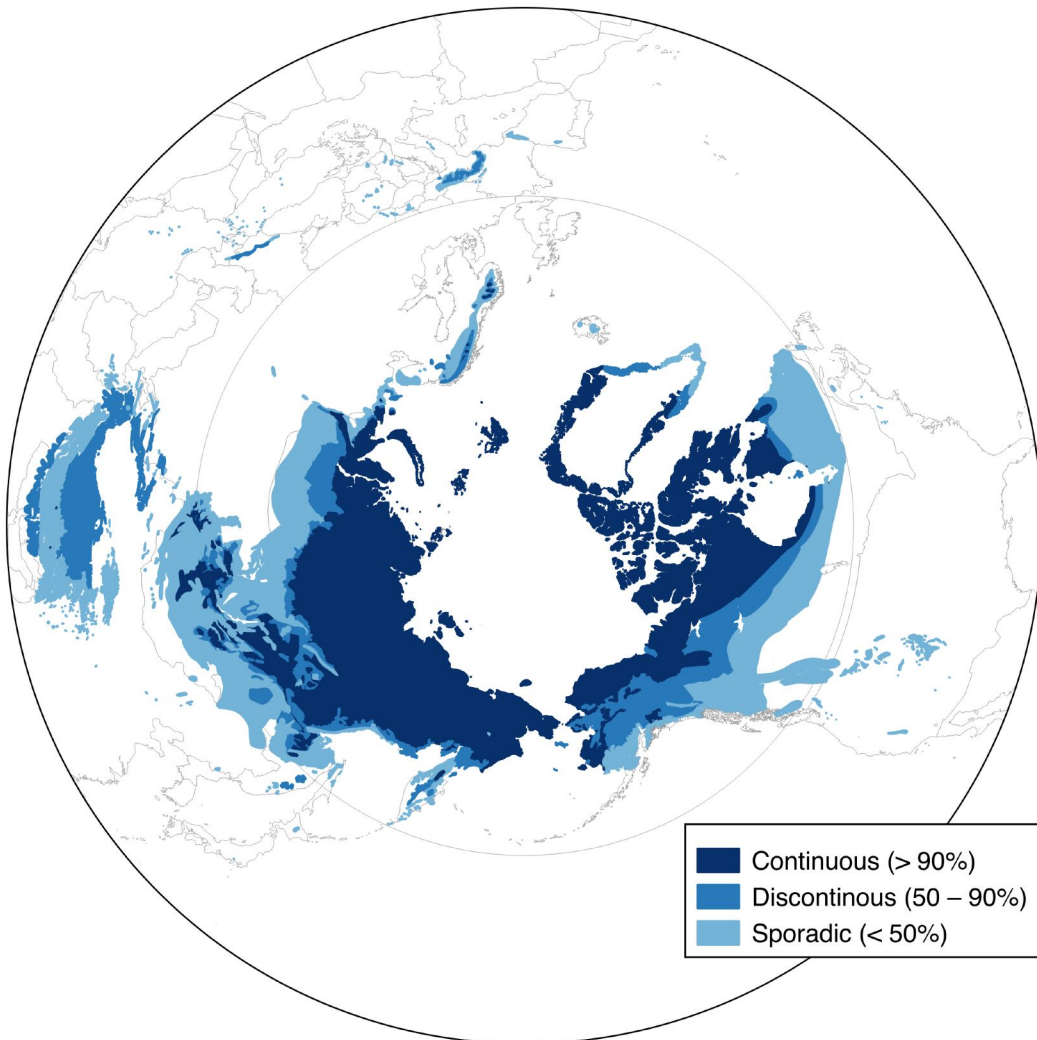


Figure 1.1: Permafrost distribution in the Northern Hemisphere based on Brown et al. (1997). The type of permafrost zonation is indicated by variously shaded colors of blue.

degradation also leads to ground ice melting near the permafrost table and affects hydrological processes (Ge et al., 2011; Walvoord and Kurylyk, 2016). In ice-rich permafrost regions, the widespread initialization and development of thermokarst landforms, such as active layer detachment and retrogressive thaw slump, have been observed (Kokelj and Jorgenson, 2013; Lewkowicz and Way, 2019; Luo et al., 2019).

Permafrost thawing also impacts the foundation stability of infrastructures, due to ground ice loss and geotechnical property changes in the near-surface permafrost (Hjort et al., 2018). To sum up, permafrost degradation influences the ecological, hydrological, geomorphological processes and infrastructures. Revealing dynamics of the active layer and near-surface permafrost is significant for predicting their future changes and making appropriate strategies and policies to accommodate the ever-changing permafrost environment.

To monitor permafrost changes and their response to climate change, the Global Climate Observing System initiated the project of Global Terrestrial Network for Permafrost (GTN-P) (Burgess et al., 2000). The GTN-P comprises two programs as Circumpolar Active Layer Monitoring (CALM) and Thermal State of Permafrost (TSP). The CALM consists of more than 160 sites in the Northern Hemisphere and aims to observe and study the response of the active layer and near-surface permafrost to climate. The TSP records ground temperatures in boreholes. It consists of more than 800 boreholes, and many of them range between 25–100 m in depth.

1.2 Ground surface elevation changes in permafrost areas

1.2.1 Ground surface elevation changes

Ground surface elevation changes are closely linked with frozen ground dynamics, in addition to the core observations of ground temperature and active layer thickness. The ground surface in a permafrost area is subject to uplift/subsidence, mainly due to the phase changes between ice and water in the active layer freezing/thawing. Therefore, we can use the surface elevation changes to probe into the thermal and hydrological variations in the active layer and near-surface permafrost.

Surface elevation changes can be measured by either traditional benchmark-based methods and modern geodetic and remote sensing ones. The traditional method uses vertical tubes or pipes, anchored deep into the permafrost, as references of ground surface for repeat leveling surveys (Mackay, 1983). The traditional approaches usually provide point measurements and have coarse temporal resolutions. Modern methods include Interferometric Synthetic Aperture Radar (InSAR), Light Detection and Ranging (LiDAR), and Global Navigation Satellite System (GNSS) positioning. InSAR has been used to measure surface deformation in various permafrost landforms (Liu et al., 2010, 2014a, 2015). It can provide accurate measurements, whose uncertainties are on the order of several millimeters. However, InSAR suffers from coarse temporal intervals (from the finest of 6 days to months) and interferometric coherence loss. It also requires a reference point which has no deformation or is assumed to be stable. More characteristics of InSAR are presented in section 6.2.2. LiDAR has been also used to construct differential elevation models to investigate surface deformation (Jones et al., 2015). However, LiDAR surveys are usually conducted at annual or multi-annual intervals. GNSS positioning has been used to quantify vertical surface movement (Little et al., 2003; Shiklomanov et al., 2013; Streletskiy et al., 2017). Those GNSS surveys are usually conducted at the end of seasons and provide point measurements. Overall, the modern methods usually have relatively coarse temporal sampling rates. Gruber (2020) invented an inclinometer, aligned to a monument anchored deep into the permafrost, to record surface elevation changes continuously. This instrument provides point measurements.

GNSS interferometric reflectometry (GNSS-IR) is a relatively new technique to measure surface elevation changes. It can provide continuous and daily measurements with intermediate spatial coverages between point observations and remote sensing ones, compared with the methods mentioned above. A detailed description of the principles and applications of GNSS-IR is presented in section 1.3.

1.2.2 Stefan equation

The Stefan equation can estimate thawing and freezing depths. It has been used to study the dependence of active layer thickness on air temperatures at a single site and the spatial variability in the response of frozen ground to air temperatures among sites (French, 2007; Smith et al., 2009). In a thawing season, surface subsidence mainly depends on the moisture content within the thawed layer. Therefore, the Stefan equation is also capable of characterizing surface elevation changes (Liu et al., 2012).

The Stefan equation is based on the key assumptions that (1) the soil is homogeneous with uniform properties, (2) the heat transfer is through conduction and the sensible heat is negligible, and (3) the temperature profile is linear in the thawed (frozen) soil in a thawing (freezing) season. It is expressed by

$$z(\tau) = \sqrt{\frac{2mK_Tn_TDDT(\tau)}{L_f\rho_w\theta}}, \quad (1.1)$$

where $z(\tau)$ is the thawing depth at the time instance τ ; K_T is the thermal conductivity of the thawed soil ($\text{J}\cdot\text{m}^{-1}\cdot\text{s}^{-1}\cdot\text{K}^{-1}$); m is the scaling factor converting a day to seconds, which equals to $86400 \text{ s}\cdot\text{day}^{-1}$; n_T is the n-factor, the ratio of ground surface temperature to air temperature; DDT, degree days of thawing, denotes the thawing index as the accumulation of air temperatures above 0°C since the onset of thawing ($^\circ\text{C}\cdot\text{day}$); L_f is the latent heat for fusion ($\text{J}\cdot\text{kg}^{-1}$); ρ_w is the density of water ($\text{kg}\cdot\text{m}^{-3}$); and θ is the volumetric water content ($\text{m}^3\cdot\text{m}^{-3}$).

Surface subsidence is the integration of volume changes caused by ice melting within a soil column with a unit area. Based on the Stefan equation, we can derive

$$d(\tau) = \frac{\rho_w - \rho_i}{\rho_i} \theta z(\tau) = \frac{\rho_w - \rho_i}{\rho_i} \sqrt{\frac{2m\theta K_T n_T DDT(\tau)}{L\rho_w}}, \quad (1.2)$$

where ρ_i is the density of ice. Contrarily with the thawing depth $z(\tau)$, surface de-

formation $d(\tau)$ varies positively with soil moisture content θ . We can rewrite this formula into

$$d(\tau) = \frac{\rho_w - \rho_i}{\rho_i} \sqrt{\frac{2m\theta K_T n_T}{L\rho_w}} \sqrt{DDT(\tau)}. \quad (1.3)$$

The above equation can be simplified into

$$d(\tau) = D \sqrt{DDT(\tau)}, \quad (1.4)$$

with the ratio D of

$$D = \frac{\rho_w - \rho_i}{\rho_i} \sqrt{\frac{2m\theta K_T n_T}{L}}. \quad (1.5)$$

The equation 1.4 have been widely used to fit surface elevation changes to estimate seasonal subsidence (Liu et al., 2012, 2014a,b, 2015; Hu et al., 2018; Chen et al., 2018). We hereafter call it the simplified Stefan model. The ratio D is generally a function of soil moisture and positively varies with it, as the thermal conductivity of the thawed soil, K_T , roughly positively changes with moisture content (Cosenza et al., 2003) and the n-factor, n_T , keeps relatively constant within the thawing season (Klene et al., 2001; Woo, 2012). Therefore, given its dependence on moisture content, the ratio D can be used to investigate the hydrological changes in the active layer.

1.3 GNSS-IR

The GNSS-IR is a type of GNSS reflectometry (GNSS-R) referring to the techniques exploiting reflected navigation satellite signals. In practice, we usually use GNSS-IR to denote the method using the interference pattern between the direct and reflected signals, and GNSS-R to the one directly utilizing reflected signals. The concept of GNSS-R was first proposed by Martin-Neira (1993) for ocean altimetry. Then, multiple fixed-platform and aircraft-based experiments were conducted to explore the feasibility of GNSS-R (Anderson, 1996; Treuhaft et al., 2001; Martin-Neira et al., 2002;

Lowe et al., 2002). The space-borne missions, including UK Disaster Monitoring Constellation (UK-DMC), TechDemoSat-1 (TDS-1), and Cyclone GNSS (CYGNSS), have been launched to monitor the tropical cyclones, near-surface soil moisture, in-land water level changes, and sea ice (Unwin et al., 2003; Gleason et al., 2005; Foti et al., 2015; Carreno-Luengo et al., 2017; Chew and Small, 2018; Li et al., 2017, 2018). A few GNSS-R attempts have been also conducted to estimate ground surface deformation. Yang et al. (2019) explored the feasibility of GNSS-R in monitoring slope movement. They used a two-antenna receiver, consisting one right-hand-circular-polarization antenna in the up direction to receiver direct signals and one left-hand-circular-polarization antenna in horizontal to capture reflected signals. The phase delays between the direct and reflected signals were calculated and converted in turn to surface deformation and used for monitoring slope stability. Li et al. (2021) used a similar antenna configuration to obtain phase delays to estimate surface deformation. They used Beidou geostationary-orbit (GEO) satellite signals. Such geometry between the GEO satellite and receiver keeps stable and observe nearly the same area. As for soil moisture content, Camps et al. (2016) initially investigated the sensitivity of the reflected signals captured by the TDS-1 mission. They found a large sensitivity to soil moisture in areas with low NDVI (normalized difference vegetation index). With increases of vegetation cover, the reflectivity and the sensitivity to soil moisture decrease. Chew and Small (2018) found that the power of the dominant reflected signals intercepted by CYGNSS is highly correlated to the Soil Moisture Active Passive (SMAP) soil moisture observations. By linear mappings and SMAP data, they converted the CYGNSS reflections to soil moisture measurements. Chew et al. (2017) also used the reflected signals received by the SMAP radar sensor to detect the freeze and thaw states in the Arctic.

The interference pattern utilized by GNSS-IR is imprinted in the signal-to-noise ratio (SNR) data, one of the observables recorded by receivers. Georgiadou and Kleus-

berg (1988) first observed the quasi-sinusoidal oscillation of the SNR observations. Dr. Larson (<https://www.kristinelarson.net>) and her collaborators dedicated to use the SNR data to estimate surface soil moisture, snow depth, vegetation growth condition, and water level changes (Larson et al., 2008b, 2009, 2013; Larson and Small, 2014; Larson, 2019). Liu and Larson (2018) was the first to use the SNR data to measure surface elevation changes in Utqiagvik, Alaska. Forward models have been also developed to simulate the reflected signals and SNR data in various surface conditions (Zavorotny et al., 2010; Nievinski and Larson, 2014; Chew et al., 2014, 2015).

In this thesis, GNSS-IR is used to measure surface elevation changes, soil moisture, and snow depth in permafrost areas. In the remainder of this section, we describe its principles, applications, and merits and limitations.

1.3.1 Principles

The global navigation satellites, such as GPS, GLONASS, Galileo, and Beidou, broadcast signals. Some of the incoming signals propagate directly from the satellite to the receiver antenna, whereas some reflect off an object, such as ground and snow, before being received by antennas. A typical GNSS-IR geometry of the antenna, signals, and a horizontal and flat ground surface as a reflector is presented in Fig. 1.2.

Compared with the direct one, the reflected signal has a phase offset, denoted by Φ , when reaching the antenna phase center. It depends on the additional path of the reflected signal Δl and the carrier wavelength λ , which can be written in

$$\Phi = k\Delta l, \quad (1.6)$$

where k is the wavenumber and equals to $2\pi/\lambda$. The path difference Δl is

$$\Delta l = 2H \sin e, \quad (1.7)$$

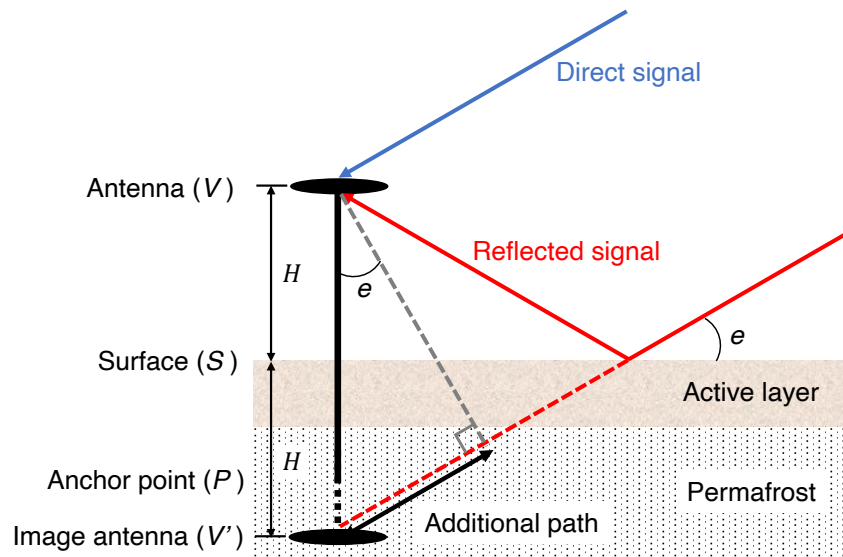


Figure 1.2: Schematic diagram of the GNSS-IR geometry of the receiver antenna, reflecting surface, direct signal, and reflected signal. We draw the image antenna with respect to the ground surface and the image propagation path of the reflected signal for clarifying its additional path. We use the symbols, including V , S , P , and V' , to denote the vertical positions of antenna, ground surface, monument anchor point, and image antenna, respectively. H is the vertical distance between antenna and surface. e is the satellite elevation angle.

where H is the vertical distance between the antenna and reflector, conventionally called reflector height and e is satellite elevation angle. Introducing equation 1.7 into 1.6, we can obtain

$$\Phi = 2kH \sin e. \quad (1.8)$$

Due to the modulation of the reflected signal on the direct one, the received signal can be expressed by a sinusoidal function as

$$u = A_u(e) \sin(\Phi + \phi_u(e)) = A_u(e) \sin\left(\frac{4\pi H}{\lambda} \sin e + \phi_u(e)\right), \quad (1.9)$$

where $A_u(e)$ and $\phi_u(e)$ are the oscillation amplitude and phase of the received signal caused by modulation, respectively. In addition to the GNSS-IR geometry, the inci-

dent signal also interacts with the reflector. Surface reflectivity and roughness affect the incident signal and imprint their effect in the reflected signal. Their impact for the navigation signal varies with the elevation angle. The receiver antenna is usually designed to have a nonuniform gain pattern along the elevation angle, to favor receiving the direct signal and suppressing the reflected one. Therefore, A_u and ϕ_u are variables of elevation angle.

1.3.2 Signal-to-noise ratio (SNR)

The power of the received signal is recorded as signal-to-noise ratio (SNR) data. SNR is calculated by

$$SNR = 10 \log_{10} \frac{A_u}{A_{noise}}, \quad (1.10)$$

where A_u and A_{noise} are the amplitudes of the received signal and background noise, respectively. As the SNR data can reflect the interference pattern, it can be expressed simply by

$$SNR = A(e) \sin\left(\frac{4\pi H}{\lambda} \sin e + \phi(e)\right), \quad (1.11)$$

where $A(e)$ and $\phi(e)$ are the amplitude and phase of SNR oscillation, respectively, mainly depending on surface reflectivity, surface roughness, and antenna gain pattern. When taking $\sin e$ as an independent variable, the oscillation frequency is

$$f = \frac{2H}{\lambda}. \quad (1.12)$$

SNR can be retrieved from the observation files in the RINEX (receiver independent exchange) format generated by the receivers. In Fig. 1.3, we present an example of SNR observations corresponding to a satellite track of GPS PRN02 on the day of year (DOY) 18 in 2017 recorded by the GNSS station BAKE in Baker Lake, Canada. The SNR data present a clear sinusoidal shape at low elevation angles.

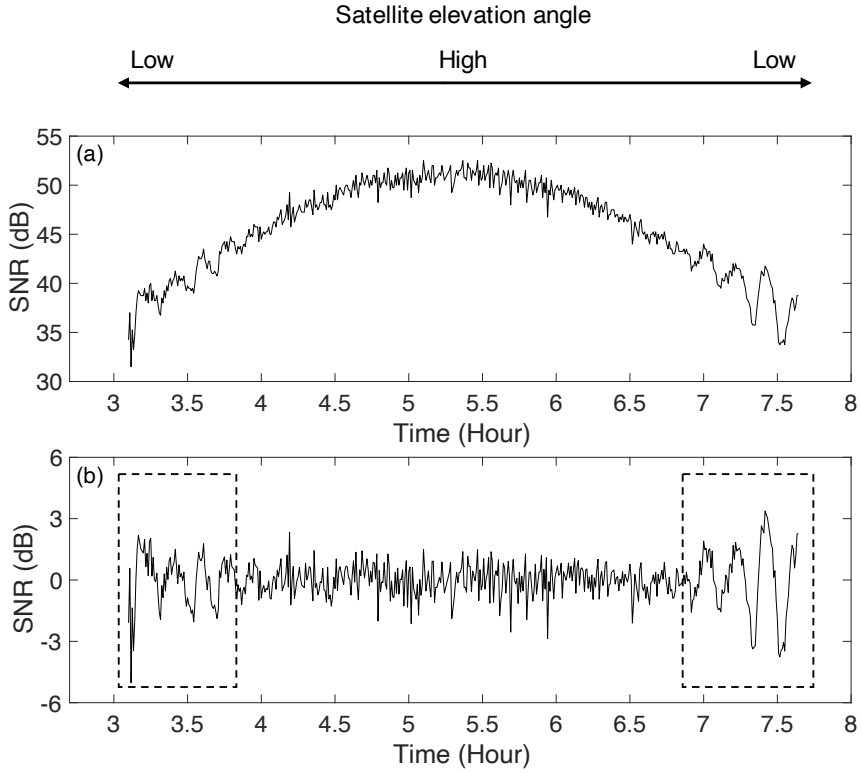


Figure 1.3: (a) Time series of SNR observations corresponding to the satellite track of GPS PRN02 on DOY 18 in 2017 recorded by the GNSS station BAKE in Baker Lake, Canada. (b) The residuals after removing the high-order polynomial fit of the SNR observations. The dashed rectangles mark the observations at low elevation angles, which have sinusoidal shapes.

1.3.3 Converting SNR metrics into environmental variables

The metrics of a piece of SNR series (alternatively called SNR interferogram) are its dominant frequency, phase, and amplitude. The frequency can be converted into reflector height, which is in turn used to estimate snow depth, water level changes, and surface elevation changes ([Larson et al., 2009, 2013; Liu and Larson, 2018](#)). The phase is mainly determined by the soil moisture in the layer of 0–5 cm depth when the GNSS-IR geometry keeps stable and the vegetation is short ([Larson et al., 2008b, 2010; Chew et al., 2014](#)). They are nearly proportional to each other. The amplitude is sensitive to the moisture content in the soil and vegetation ([Larson et al., 2008a; Small](#)

et al., 2010). In this section, we describe the steps to retrieve SNR metrics, convert the frequencies to surface elevation changes in snow-free season and snow depth on snow-cover days, and map the phases to surface soil moisture content.

Retrieving SNR metrics

For any given SNR series corresponding to a rising/setting satellite track at low elevation angles (e.g., 5–30 degrees), we first remove its low-order polynomial fit and use the residuals, which are mainly contributed by the interference between the direct and reflected signals. We then conduct Lomb-Scargle Periodogram (LSP) analysis on the residuals to derive its frequency spectrum. LSP has the advantage of processing unequally spaced samples (Lomb, 1976). From the frequency spectrum, we can find the one with peak power to be the dominant frequency of SNR data, which is then converted into reflector height by equation 1.12. Multiple navigation satellites (e.g., 32 GPS satellites to date) orbit around the Earth. On any given day, numerous satellite tracks and SNR interferograms are available. We can obtain the reflector heights from all of the available SNR data and use their mean to be the daily measurement. The standard deviation of the mean value (i.e., the standard deviation of samples divided by the square-root-of sample size) is taken as the uncertainty. The program of Roesler and Larson (2018) is used for data processing.

To obtain the phase, we initially need to prescribe an *a priori* reflector height H_0 . For any given SNR interferogram on any given day, we fix the reflector height to be H_0 and use the Least Square Estimation (LSE) to determine the phase. Then, we offset the phase time series of each satellite track over the data time span by subtracting the mean value of their lowest 15% (Chew et al., 2016). This step aims to avoid the impact of anomaly low phase data caused by vegetation or random noise. Then, on any given day, we use the average phase to be the daily measurement. The standard deviation of the mean value is used to be the uncertainty. In previous studies, for a given time

span, the mean value of the daily reflector heights is taken to be the H_0 .

In Fig. 1.4, we show the SNR data within the azimuth range of 90–180 degrees on DOY 210 in 2019 recorded by SG27 in Utqiagvik, Alaska, and their LSP spectrums. We can observe that the dominant frequencies of these SNR data are significant and consistent, which implies that the reflector height of the ground surface in the azimuth mask can be determined reliably. A sinusoidal fit of the SNR data by using the retrieved reflector height, phase, and amplitude is presented as well.

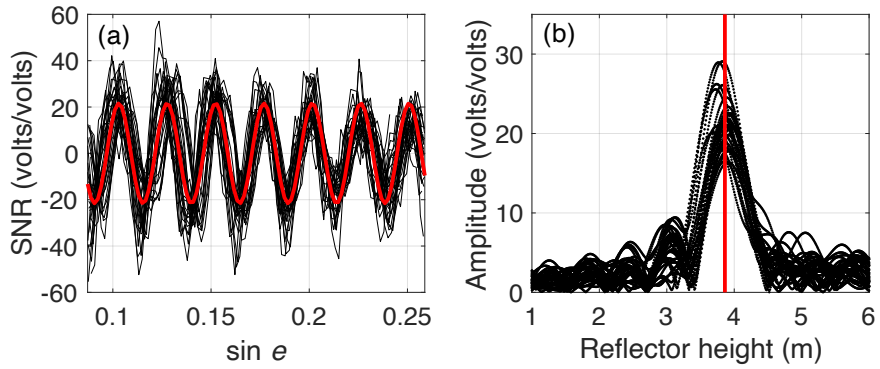


Figure 1.4: (a) SNR interferograms within the azimuth range of 90–180 degrees on DOY 210 in 2019 recorded by SG27 in Utqiagvik, Alaska. The red sine curve is created by using the average values of the dominant frequencies, amplitudes, and phases of the SNR series. (b) Frequency spectrums of the SNR interferograms. The frequency has been converted into reflector height. The red vertical line is the mean value of the reflector heights with peak amplitudes. The scale of SNR data has been converted from dB to volts/volts.

Surface elevation changes

On snow-free days, the variations of reflector heights reflect surface elevation changes. Considering the GNSS-IR geometry (Fig. 1.2), with respect to an arbitrary reference in the deep permafrost, the reflector height H is the difference between the antenna position V and ground surface S , which is in the expression of

$$H = V - S. \quad (1.13)$$

Given the monument with a length of L , the monument anchoring position is

$$P = V - L. \quad (1.14)$$

By introducing equation 1.14 into 1.13, we can obtain that

$$H = L + P - S. \quad (1.15)$$

When the monument is stable relative to the permafrost and its length L keeps constant, the reflector heights are reversed with surface elevation changes. In other words, the increase (decrease) of reflector height means surface subsidence (uplift). In practice, we remove the mean value of the negative daily reflector heights and use the residuals to represent surface elevation changes.

Snow depth

Snow surface acts as the reflector when the ground is covered by snow. The reflector heights in snow seasons can be converted into snow depth. In Fig. 1.5, we present a schematic diagram to show the concept of retrieving snow depth, which is the difference between the reflector height of snow surface (denoted by H_{snow}) and the one for ground (H_{ground}) serving as the reference. In previous studies, the mean of daily reflector heights in snow-free seasons is usually used to be the reference. However, in permafrost areas, the surface is subject to subsidence in summer. Using the mean reflector height in summer may introduce a bias. Thus, in this thesis, we use the average reflector height at the beginning of thawing season.

Surface soil moisture

The phases of SNR interferograms are nearly proportional to the soil moisture content in the 0–5 cm layer. Several methods are available to map the phases to soil moisture

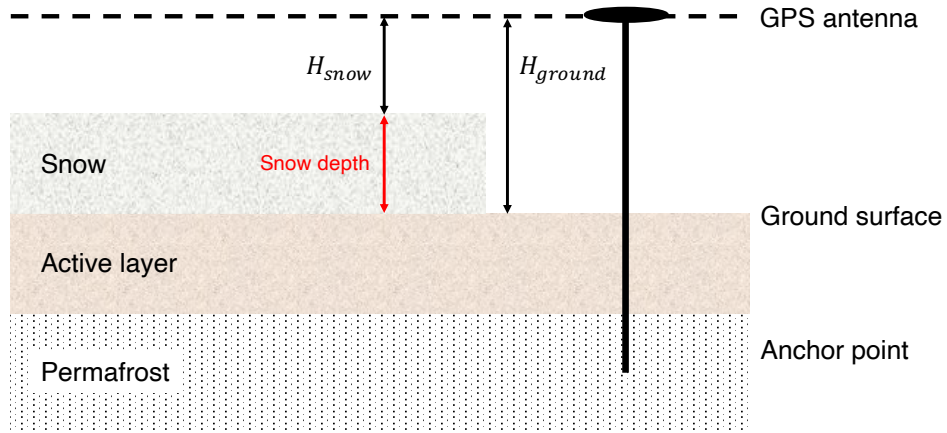


Figure 1.5: Schematic diagram showing the reflector heights in snow-cover and snow-free conditions. The snow depth is the difference between the reflector height in snow-season (H_{snow}) and the one for ground (H_{ground}) as reference.

content. The direct one is to compare in situ measurements and the phases to obtain their linear mapping parameters, i.e., slope and intercept (called residual soil moisture content in literature).

An alternative method is to use the simulated slope and residual soil moisture content. [Chew et al. \(2014\)](#) conducted simulations to obtain the slope of $1.48 \text{ cm}^3 \cdot \text{cm}^{-3} \cdot \text{deg}^{-1}$, in the conditions without significant vegetation. The residual soil moisture content can be estimated based on soil type and texture, which are available in public datasets, such as STATSGO of US Geological Survey ([Schwarz and Alexander, 1995](#)).

1.3.4 Merits and limitations

The GNSS-IR can provide continuous and daily measurements at permanently operating stations. Such a feature helps investigate the changes in permafrost areas at various temporal scales and provides new insights into frozen ground dynamics. In addition, the GNSS-IR measurements have intermediate spatial coverages on the order of 1000 m^2 , which can bridge the point in situ observations and remote sensing ones with regional coverages. Given the fine temporal resolutions and local scales,

the GNSS-IR measurements can also calibrate and validate the air and space-borne remote sensing observations (see more details in 6.2.2). Furthermore, the GNSS-IR measurements of surface elevation changes are free of solid earth movement, such as glacier isostatic adjustment and plate movement (Liu and Larson, 2018).

Some challenges exist when using GNSS-IR. This technique has a strict requirement on surface conditions. It only works when the reflecting surface is open and nearly horizontal and smooth, ensuring sufficient coherent reflections to interfere with the direct signals. As for estimating soil moisture, in situ measurements are usually in absence to determine the mapping parameters. The simulated scale factor from Chew et al. (2014) is specified for a certain kind of antenna. A bias may be introduced when using a different antenna. Moreover, the simulated residual moisture content by using soil type and texture may deviate significantly from the true value.

1.4 Contributions

For the first time, we screened the major GNSS networks and identified 23 sites in the Arctic permafrost regions and one site in QTP, which are suitable for GNSS-IR studies. We also obtained their reflector heights, which can be converted into surface elevation changes in snow-free seasons and snow depth on snow-cover days. The usable sites have been published in Zhang and Liu (2021) and their GNSS-IR results have been archived in Zenodo (Zhang and Liu, 2020). The permafrost areas are extensive but with scarcely and unevenly distributed monitoring sites, such as CALM sites and boreholes. Our suitable sites can fill some spatial gaps. Their GNSS-IR measurements complement the core observations, including active layer thickness and ground temperature, and provide new insights into frozen ground dynamics. The daily and continuous GNSS-IR measurements can be used to calibrate/validate those from the air and space-borne sensors.

We used the GNSS-IR-estimated surface elevation changes at five sites in the Canadian Arctic, i.e., Alert, Resolute Bay, Repulse Bay, Baker Lake, and Iqaluit, to analyze their multi-year linear trend, interannual variability, and seasonal variations, to probe into frozen ground dynamics. The ground surface underwent subsidence in Alert, Resolute Bay, and Baker Lake with warming thawing seasons. Whereas, Iqaluit presented a subsidence trend in cooling summers. The ground surface in Repulse Bay did not have a significant trend. The air temperature might be the driver of permafrost degradation in most sites in the Canadian Arctic. In Iqaluit, the air temperature's impact was possibly moderated by other environmental variables, such as vegetation and soil moisture. In Resolute Bay, the end-of-thaw elevations during 2003–2012 were negatively related to the square-root of thawing indices, whereas they were low in 2013 and 2014 with cool summers. This change might be caused by the variations in soil properties and ground ice content near the permafrost table. As for seasonal variations, they were irregular from the typical pattern of progressive subsidence in most of the years at each site. Most of the data analysis and interpretation have been published in [Zhang et al. \(2020\)](#).

We used the GNSS-IR-measured seasonal subsidence to infer the moist-to-dry shift of the active layer in Utqiagvik, Alaska. By comparing seasonal subsidence and square-root-of thawing index, we observed a significant drop of their ratios from 2004–2008 to 2009–2018. The seasonal subsidence was more sensitive to air temperature during 2004–2008. The sharp ratio decrease was hypothesized to be caused by the active layer drying and induced changes in soil thermal properties, which was validated by in situ measurements of soil moisture and ground temperatures. This study is the first to use surface elevation changes to investigate soil moisture changes in the active layer. It reveals the importance of soil moisture in affecting the response regime of the frozen ground through a new perspective. It also implies the necessity to evaluate the contribution of soil moisture when using vertical surface movement

to infer permafrost degradation and aggradation.

We also improved the commonly-used GNSS-IR algorithm for estimating surface soil moisture in permafrost areas. This improvement can mitigate the impact of seasonal surface elevation changes. We also proposed a three-in-one framework to integrate the GNSS-IR measurements of surface elevation changes, soil moisture, and snow depth at the same site. The framework can fully utilize the potential of GNSS-IR in permafrost studies. It can be extended to the usable sites in the Arctic. We have published this study in [Zhang et al. \(2021b\)](#).

1.5 Roadmap

The remainder of the thesis is organized as follows. In Chapter 2, we present the usable sites in permafrost areas for GNSS-IR studies and the unsuitable sites and their causes. We also provide a detailed discussion of the possible error sources of GNSS-IR measurements of surface elevation changes. Then, in Chapter 3, we use the GNSS-IR-estimated surface elevation changes at selected sites to study the changes in the frozen ground. In Chapter 4, we use the GNSS-IR-measured seasonal subsidence and its relationship with thawing index to study hydrological dynamics of the active layer during 2004–2018 in Utqiagvik, Alaska. In Chapter 5, we improve the commonly-used GNSS-IR algorithm of estimating soil moisture to correct the impact of the seasonal surface deformation in permafrost areas. We conclude this thesis by Chapter 6.

End of chapter.

Chapter 2

Suitable sites in the Arctic permafrost areas for GNSS-IR studies¹

2.1 Introduction

Since the 1990s, thousands of GNSS stations have been installed and maintained to monitor solid earth movement, measure precipitable water vapor in the troposphere, and estimate total electron content in the ionosphere. Nearly 200 of them are located in the permafrost regions in the Arctic (referring to the area north of the latitude 50° N in this study). However, not all of them are suitable for GNSS-IR studies, as this technique requires the ground surface to be open and relatively smooth and horizontal. Moreover, only one site, i.e., SG27 in Utqiagvik, Alaska, was assessed and proved to be useful for GNSS-IR applications by Liu and Larson (2018). Thus, in this study, our objectives are (1) identifying the suitable sites in the Arctic permafrost areas by

¹This chapter is based on Jiahua Zhang and Lin Liu (2021). Mining noise data for monitoring Arctic permafrost by using GNSS interferometric reflectometry. Polar Science. 100649. <https://doi.org/10.1016/j.polar.2021.100649>

screening the major GNSS networks, (2) estimating the GNSS-IR measurements of surface elevation changes at the usable sites, and (3) analyzing the dominant causes for the unsuitable sites in the permafrost areas.

Permafrost has been observed to be warming and thawing in the Arctic in the last decade ([Biskaborn et al., 2019](#); [Vasiliev et al., 2020](#)). Permafrost degradation has a significant impact on climatic, ecological, geomorphological, and hydrological processes and infrastructures. Monitoring and quantifying the changes in permafrost areas are crucial for understanding frozen ground dynamics and predicting its future changes. However, the monitoring sites, such as the CALM sites and TSP boreholes, are still limited and unevenly distributed in the extensive permafrost areas in the Arctic. This study can provide usable GNSS sites to fill some spatial gaps. The GNSS-IR observations can complement active layer thickness and ground temperature and provide new insights into frozen ground dynamics. Moreover, the GNSS-IR observations can be used to assess the risk of permafrost degradation on the infrastructures and help making appropriate policies and strategies to increase the resilience of residential communities and adapt to the ever-changing environment.

In section [2.2](#), we present the steps to identify usable GNSS stations in permafrost areas. We also briefly describe the GNSS networks screened in this study. The results are presented in section [2.3](#), which shows the basic information of the suitable stations and dominant reasons for the unsuitable ones. In section [2.4](#), we discuss the possible error sources of the GNSS-IR measurements of surface elevation changes. We then present the merits of the usable sites and their GNSS-IR measurements. We also raise concerns when using the measurements at the sites in non-continuous permafrost areas. We conclude this study in section [2.5](#).

2.2 Methodology

2.2.1 A framework to identify usable sites in permafrost areas

We have proposed a three-step framework to identify usable GNSS sites from the existing ones ([Zhang et al., 2020](#)), which is described as follows:

- The first step is to select the GNSS stations in the Arctic permafrost areas. We use the permafrost map compiled by [Brown et al. \(1997\)](#). This map has been well applied in permafrost studies. It gives a first-order estimation of permafrost existence at a site.
- The second step is to assess surface conditions at the selected sites. We use ground photos to evaluate whether the surrounding area is open and the ground surface is relatively horizontal and smooth. A site surrounded by obstructions or with a rugged surface will be regarded as unsuitable and discarded. Otherwise, the azimuth range with an open and relatively homogeneous and horizontal surface will be determined. The SNR data within this azimuth mask will be used. The ground photos are usually kept as a part of metadata and can be obtained from the corresponding maintainer. The Google Earth images can be used alternatively if the ground photos are not available. Figure [2.1](#) presents the ground photos and SNR observations of SG27 in Utqiagvik, Alaska and YELL in Yellowknife, Canada. SG27 is located on a relatively smooth and flat surface, and its SNR data present a quasi-sinusoidal pattern. Whereas, YELL is surrounded by trees and located on the undulated ground, therefore no clear sinusoidal pattern can be observed from its SNR observations.
- The last step is to examine the sufficiency of SNR interferograms with clear sinusoidal patterns on a daily basis. To ensure the acceptable quality of the GNSS-IR measurements, we require the minimum number of the usable SNR

series to be five. This number is determined empirically and adopted by Chew et al. (2016) as well. A site will be excluded if the usable SNR data is less than five on most of the days over the entire data time span.

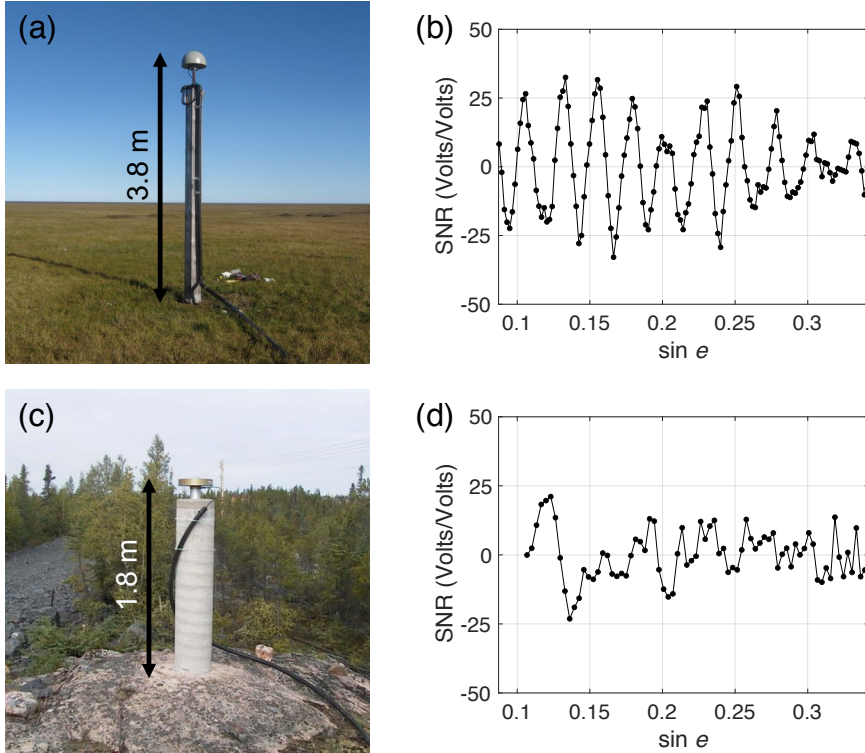


Figure 2.1: (a) A ground photo of SG27 in Utqiagvik, Alaska. (b) A piece of SNR interferogram at the satellite elevation angles of $5\text{--}20^\circ$ recorded by SG27. The second-order polynomial fit of the SNR observations has been removed. (c) and (d) are similar to (a) and (b) correspondingly but for YELL in Yellowknife, Canada. The monument heights of SG27 and YELL are marked as well.

2.2.2 GNSS networks

In this section, we briefly summarize the open-data GNSS networks considered in this study, including the International GNSS Service (IGS), the Plate Boundary Observatory (PBO), the Canadian Active Control System (CACS), the Portable Observatories for Lithospheric Analysis and Research Investigating Seismicity (POLARIS), the

Canadian High Arctic Ionospheric Network (CHAIN), the EUREF Permanent GNSS Network (EPN), and the Greenland Network (GNET).

The **IGS** is a program of the International Association of Geodesy, which is dedicated to offering the highest-quality GNSS data and products to support the terrestrial reference frames, positioning, navigation, timing, environmental research, and other applications benefiting society (Dow et al., 2009). The IGS network has more than 500 continuously operating sites to date, which are distributed globally. Twenty-five IGS stations are located in the Arctic permafrost areas.

The **PBO** is maintained by a non-profit university-governed consortium (UNAVCO). It consists of 1100 GPS stations continuously operating in the United States. The PBO stations have been used to monitor solid earth movement, estimate precipitable water vapor, measure ionospheric electron content, and observe other environmental variables such as snow water equivalent and surface soil moisture content. Fifty-three PBO sites are in the Arctic permafrost regions, and most of them are in Alaska.

The **CACS** is a network across Canada and maintained by the Geodetic Survey Division and Geological Survey of Canada (Lahaye et al., 2001). It was initialized for constructing and maintaining the Canadian Spatial Reference System for surveying and mapping. The CACS comprises five sub-networks, including the National Network, Reginal Network, Western Canada Deformation Array, Nova Scotia Active Control Network, and Montreal Active Control Network. The CACS has 130 continuously operating sites. Twenty-three of them are located in the permafrost areas.

The POLARIS network is located in Canada as well, which consists of seven GPS stations. It was initially designed to map the solid earth structure and assess the earthquake hazards (Eaton et al., 2005). The POLARIS is maintained by the University of Western Ontario. Two of them are located in the permafrost areas.

The **CHAIN** is also distributed in Canada. It was originally built for studying the ionosphere and the influence of solar activity on the planetary environment (Jay-

achandran et al., 2009). The CHAIN is maintained by the University of New Brunswick. It has 25 GPS stations. The sites of KUGC, REPC, and QIKC share antennas with the CACS sites, namely KGLK, REPL, and QIKI, correspondingly. Twenty-four of the CHAIN sites are in the Arctic permafrost regions.

The EPN is a network across the European continent (Bruyninx et al., 2019). It has more than 330 stations, 30% of which belong to the IGS network. The EPN was initiated to support and maintain the Europe Terrestrial Reference System and its realizations. It has been also used to investigate solid earth movement and environmental changes. Three EPN stations are in the Arctic permafrost areas.

The GNET is distributed across Greenland. It is currently maintained by the Danish Agency for Data Supply and Efficiency. The GNET has been used to conduct precise navigation and study climate, meteorology, and space weather. This network consists of 59 stations to date. All of them are located in the permafrost regions.

Figure 2.2 shows the locations of GNSS sites in the Arctic permafrost areas. We can observe that most of them are located in Alaska, northern Canada, and Greenland and a few scattered in the Eurasian permafrost regions.

2.3 Results

We identified 23 usable stations from 186 in the Arctic permafrost areas. The SG27 in Utqiagvik, Alaska, has been published in Liu and Larson (2018), and the CACS and CHAIN sites have been reported in Zhang et al. (2020). At these usable sites, the ground surface within the determined azimuth range is open and relatively flat and horizontal, and the number of usable SNR interferograms is sufficient. The basic information of the usable stations, such as geographical coordinates, permafrost zonation, corresponding network, monument type, reflector height, azimuth range, elevation angle, has been summarized in Table 2.1.

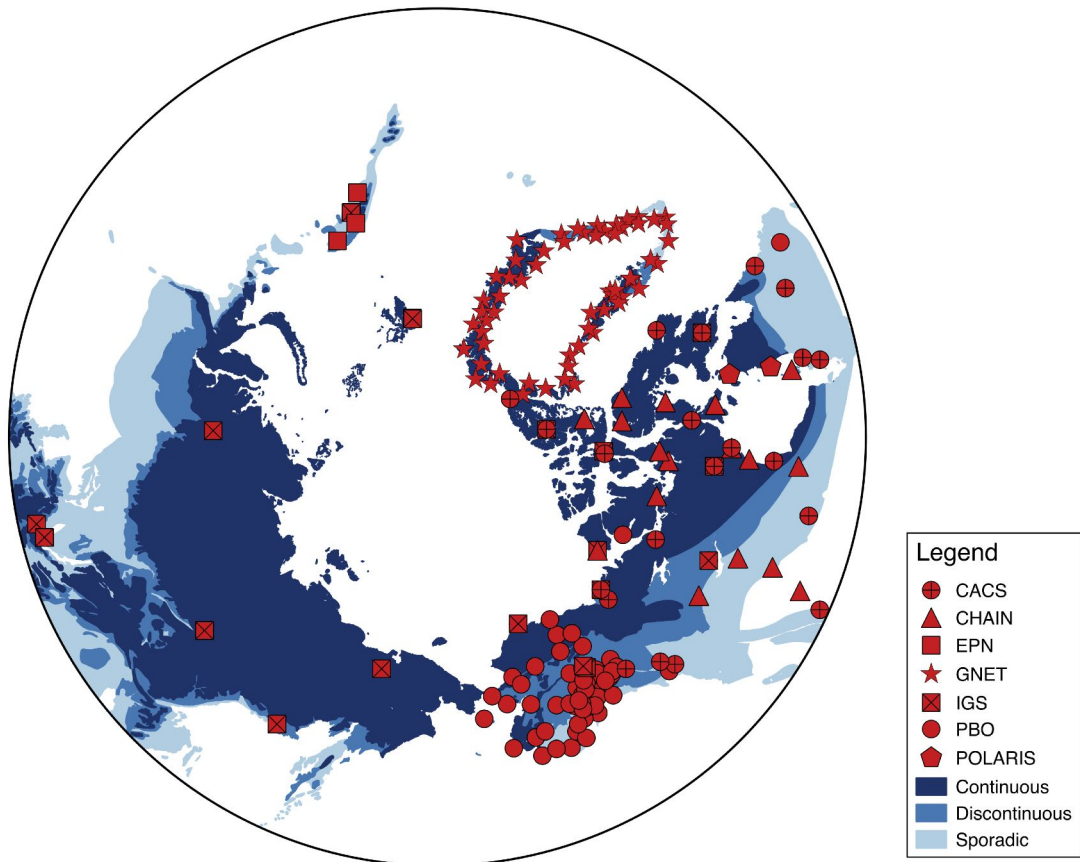


Figure 2.2: Locations of the open-data GNSS sites in the Arctic permafrost areas north of 50° N.

Table 2.1: Basic information of the usable sites in the Arctic permafrost areas.

ID	Site name	Latitude (degree)	Longitude (degree)	Permafrost zonation ²	Network	Monument type ³	Reflector height (m)	Azimuth range (degree)	Elevation angle (degree)
ALRT	Alert, Canada	82.494	-62.340	C	CACS	Galvanized steel pipe	1.9	250–360	8–20
BAKE	Baker Lake, Canada	64.318	-96.002	C	CACS	Stainless steel pillar	1.2	0–360	7–20
IQAL	Iqaluit, Canada	63.756	-68.510	C	CACS	Aluminium cylinder	1.8	30–120	8–20
REPL	Repulse Bay, Canada	66.524	-86.231	C	CACS	Aluminium pillar	2.0	150–250	5–20
RESO	Resolute Bay, Canada	74.691	-94.894	C	CACS	Steel pipe	2.3	0–360	5–20
FSIC	Fort Simpson, Canada	61.757	-121.228	D	CHAIN	Building	3.9	150–330	5–20
FSMC	Fort Smith, Canada	60.026	-111.933	S	CHAIN	Building	4.1	30–120	5–20

IQAC	Iqaluit, Canada	63.737	-68.540	C	CHAIN	Building	4.0	170–340	10–20
PONC	Pond Inlet, Canada	72.693	-77.955	C	CHAIN	Building	4.5	150–240	5–18
RANC	Rankin Inlet, Canada	62.825	-92.115	C	CHAIN	Building	3.8	150–300	5–20
SANC	Sanikiluaq, Canada	56.536	-79.231	D	CHAIN	Building	3.3	135–225	5–20
AB39	Fort Yukon, Alaska	66.559	-145.213	D	PBO	NA	2.1	0–360	8–18
AC07	Buckland, Alaska	65.961	-161.287	D	PBO	NA	1.5	0–360	5–20
AC71	Delta Junction, Alaska	64.049	-145.714	D	PBO	NA	1.8	150–300	5–20
AC78	Northway, Alaska	63.113	-142.028	D	PBO	NA	1.3	150–200	6–20
SG27	Utqiagvik, Alaska	71.323	-156.610	C	PBO	Wooden pillar	3.8	90–180	5–20

WIKR	Kantishna, Alaska	63.553	-150.922	D	PBO	NA	1.7	45–180	5–20
KIRU	Kiruna, Sweden	67.857	20.968	S	IGS	Concrete block	1.1	0–360	5–20
SACH	Sachs Harbour, Canada	71.990	-125.250	C	IGS	NA	3.0	0–360	8–20
UTQI	Utqiagvik, Alaska	71.323	-156.615	C	IGS	Steel Tube	7.0	140–250	5–20
JUBL	Jorgen Bronlund, Greenland	82.209	-31.004	C	GNET	NA	1.3	0–360	5–20
KMJP	Kap Morris Jessup, Greenland	83.643	-33.377	C	GNET	NA	0.9	130–230	5–20
SCBY	Kap Schoubye, Greenland	80.260	-59.594	C	GNET	NA	1.2	0–360	5–20

²C, D, and S stand for continuous, discontinuous, and sporadic permafrost regions, respectively.

³NA denotes that the monument type is not available from the log file kept by the maintainer.

The reflector heights at the usable sites have been obtained and published on ZENODO ([Zhang and Liu, 2020](#)). They can be converted into surface elevation changes in snow-free seasons and snow depth on snow-cover days. The uncertainties of surface elevation changes are on the order of a few centimeters. Table 2.2 presents the mean values and standard deviations of the uncertainties of the GNSS-IR results in July and August of each year over the data time span at each site.

As for the unsuitable sites, their fundamental reason is that no sufficient (i.e., less than five in this study) SNR interferograms with clear sinusoidal patterns are available on a daily basis. The obstructions and undulated surfaces are the main causes of irregular SNR data. We categorized the causes into three classes: obstruction, undulated surface, and insufficient SNR data at the sites with open and relatively horizontal and smooth areas (simplified as insufficient interferogram). Figure 2.3 shows the percentage of unusable sites due to each cause.

Sixty-eight percent of the unsuitable sites are due to undulated surfaces. The rough surface diffuses the incident signals, therefore, no sufficient coherent reflected signals interfere with the direct ones. The incoherent reflections also disturb the coherent components, leading to noisy SNR data. Twenty-five percent of the unusable sites are due to surrounding obstructions, such as buildings, trees, and tall shrubs. The obstructions block the incident signals at low elevation angles. On the other hand, the signals reflected off the obstructions interfere with the direct ones causing irregular SNR data. The sites located in residential communities, tall and dense shrubs, and boreal forests are usually unsuitable for GNSS-IR studies. Moreover, 7% of the unusable sites were due to insufficient usable SNR data, even though the azimuth ranges with open and relatively flat and smooth areas can be determined. A table of unusable sites and their corresponding causes can be found in [Zhang and Liu \(2021\)](#).

Table 2.2: Mean and standard deviation of the uncertainties of the GNSS-IR measurements in July and August over the data time span at each site.

Station	Mean of uncertainties (cm)	Std of uncertainties (cm)	Data time span
ALRT	1.51	0.24	2012-2019
BAKE	2.19	0.22	2010-2019
IQAL	2.85	0.53	2009-2019
REPL	2.63	1.31	2014-2019
RESO	2.10	0.27	2003-2014
FSIC	1.74	0.39	2014-2019
FSMC	1.62	0.25	2014-2019
IQAC	3.29	0.81	2009-2019
PONC	3.65	1.00	2009-2019
RANC	1.76	0.35	2014-2019
SANC	2.57	0.44	2009-2019
AB39	3.27	0.69	2009-2019
AC07	2.51	0.68	2008-2019
AC71	1.81	0.38	2007-2019
AC78	2.81	2.24	2010-2019
SG27	1.10	0.23	2004-2019
WIKR	2.49	0.54	2009-2019
KIRU	2.72	0.87	2003-2019
SACH	2.19	0.12	2003-2005
UTQI	4.80	3.80	2018-2019
JGBL	1.88	0.58	2009-2019
KMJP	3.44	0.81	2009-2019
SCBY	1.13	0.33	2008-2019

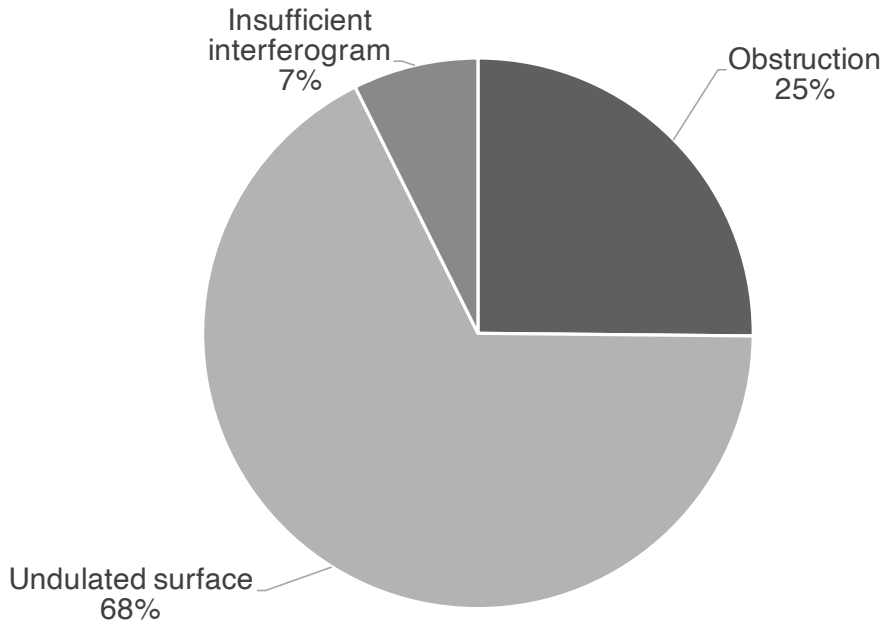


Figure 2.3: Percentages of the unsuitable sites for the causes, including obstruction, undulated surface, and insufficient SNR interferogram.

2.4 Discussion

2.4.1 Error sources of the GNSS-IR measurements of surface elevation changes

The identified GNSS sites are all located in the permafrost areas, which are remote and logistically hard to access. Thus, it is challenging for us to obtain in situ measurements to validate our GNSS-IR observations and assess their accuracy. We can have a general impression of the accuracy of GNSS-IR measurements from [Liu and Larson \(2018\)](#). They compared the GNSS-IR observations to the GPS positioning results at a nearby site and found that they have a good agreement.

We here focus on discussing the possible error sources of the GNSS-IR-estimated surface elevation changes. The errors are usually from the signal propagation through the atmosphere, receiver antenna, monument stability, and the interaction between

the incident signal and the ground.

Tropospheric delay

The incident signal suffers from the bending propagation path and velocity decrease due to refraction in the troposphere. Such influence is conventionally called tropospheric delay. In the framework of GNSS-IR, the reflected signal propagates an addition path, compared with the direct one (Fig. 1.2). The tropospheric delay of this additional path may introduce an error in the GNSS-IR measurement.

The magnitude of the tropospheric error dominantly depends on the water vapor content below the level of receiver antenna. A simple refraction correction model of [Bennett \(1982\)](#) can be used to quantify the tropospheric bias. It requires surface pressure and air temperature as input. In permafrost areas, the tropospheric bias is conceptually small for a typical several-meter high station, due to the dry climate with scarce precipitation.

In Resolute Bay, we calculated the tropospheric bias in the thawing season spanning DOY 192–250 in 2014 (Fig. 2.4). The magnitudes of the tropospheric errors are on the order of ~ 1.6 cm and nearly stable. As we focus on the temporal variations of surface elevation changes, the impact of tropospheric bias is limited. Another example at the site of QLBG in QTP can be found in section [5.5.2](#).

Antenna gain pattern

The GNSS receiver antenna is usually designed to have an asymmetric gain pattern along the elevation angle, for favoring the reception of direct signals and suppressing the direct ones with low elevation angles and the reflected signals. Given any piece of SNR interferogram, antenna gain pattern has a different impact on each data point. However, for the SNR interferograms with the same elevation angles, they suffer from the same impact from the gain pattern. Thus, the gain pattern's influence on the

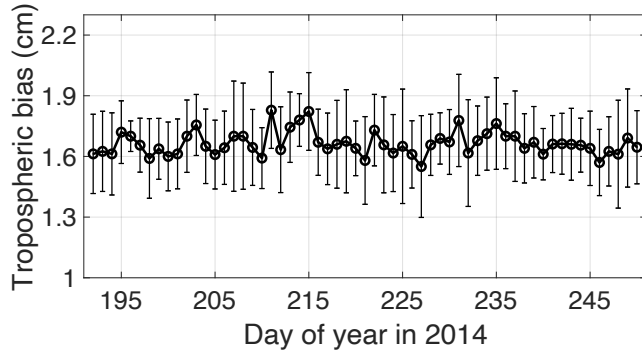


Figure 2.4: Tropospheric biases of the GNSS-IR-estimated surface elevation changes in Resolute Bay in the thawing season (i.e., DOY 192–250) of 2014. They are the mean values of the tropospheric biases of all satellite tracks. Their standard deviations are indicated by error bars.

metrics of SNR data, i.e., frequency and phase, can be regarded as a systematic bias. As we consider the temporal variations of the GNSS-IR measurements, the antenna gain pattern has a negligible impact.

Monument thermal expansion and contraction

The thermal expansion and contraction affect the monument length (L in equation 1.15) then the GNSS-IR geometry. It might introduce errors into the reflector heights and phase measurements, consequently affecting surface elevation changes, snow depth, and soil moisture content. The magnitude of the thermal deformation depends on monument material and ambient temperature.

The materials are mainly steel, aluminum, concrete, and wood for the identified usable sites with clear descriptions of monument types (Table 2.1). Their linear thermal deformation coefficients range from 3.0 to $23.1 \times 10^{-6} \text{ m}\cdot\text{m}^{-1}\cdot\text{}^{\circ}\text{C}^{-1}$ (https://www.engineeringtoolbox.com/linear-expansion-coefficients-d_95.html). Given a temperature range of $20\text{ }^{\circ}\text{C}$ in a thawing season, for a 2 m high monument, the magnitude of the thermal expansion is less than 1 mm , at least one order of magnitude smaller than the uncertainties of surface elevation changes. Therefore, the thermal

expansion and contraction's impact is negligible for the GNSS-IR measurements at these sites.

For the rest of the sites, detailed records of monument materials are needed for quantifying the thermal expansion and contraction.

Monument foundation stability

The stability of monument foundation (i.e., P in equation 1.15) also impacts the GNSS-IR geometry. The GNSS stations designed for geodetic applications, including the CACS, PBO, IGS, and GNET stations, usually have stable monuments anchored deep into the solid earth. Whereas, the CHAIN stations might have unstable monuments. Their receiver antennas are aligned to the walls of buildings or mounted on the roofs. The antenna might move along with the building foundation and impact the GNSS-IR geometry.

To quantify the monument stability, we can use the positioning results in the NEU (north, east, and up) reference system. The north and east coordinates indicate the monument inclination. The positioning results in the up direction are mainly contributed from atmospheric and hydrological loadings, solid earth movement, and foundation movement. We can obtain the foundation movement after removing the loadings and solid earth movement. An example can be found in section 5.5.1, where we assess the foundation stability of QLBG.

Soil moisture

Soil moisture affects reflector heights, then surface elevation changes. It plays a key role in determining surface reflectivity, which varies with respect to elevation angle. For any given SNR interferogram, soil moisture's impact on each data point is different, i.e., $\phi(e)$ is a variable. Taking $\phi(e)$ as a constant in data processing might introduce a bias into the reflector height, which is conventionally called compositional

reflector height.

The impact of compositional height can be simulated by the physical model of Nievinski and Larson (2014). Liu and Larson (2018) used it to simulate the compositional heights in Utqiagvik, Alaska, which were less than 2 cm and varied within the peak-to-peak range of less than 1 cm, given a change of soil moisture between 15% and 40%. In this study, the compositional heights and their variation ranges are expected to be limited, as the precipitation is light and scarce due to the cold and dry climates in permafrost areas. Moreover, as we focus on the temporal variations of surface elevation changes, we expect their negligible impact on our results.

Vegetation

Vegetation also affects the incident signal through its water content and structure. The feasibility of GNSS-IR depends on the vegetation type, when the vegetation is dense and higher than the wavelength of the L-band GNSS signals. Zhang et al. (2017b) found that the reflector was the interface between the air and wheat, when the wheat was higher than the wavelength of the GPS signal. Whereas, Small et al. (2010) found that the SNR data did not present a clear sinusoidal pattern when the corn was ~ 2 m tall. In these cases, GNSS-IR cannot estimate surface elevation changes.

The vegetation is short and sparse at the usable sites in permafrost areas, which is nearly transparent for the GNSS signals. Thus, it has negligible impact on the results of surface elevation changes.

2.4.2 Merits of usable sites and their GNSS-IR measurements

The usable sites can fill some spatial gaps of the current permafrost monitoring programs, such as CALM and TSP (Fig. 2.5). Though the development of CALM and TSP in the last decades, their sites are distributed unevenly and exhibit large gaps, which cannot fully represent the permafrost conditions. The identified usable sites

can fill some gaps, such as in northern Canada. The GNSS-IR measurements complement the core observations, including active layer thickness and ground temperature. They can reveal the changes of frozen ground in a different perspective and provide new insights into frozen ground dynamics. The usage of GNSS-IR-estimated surface elevation changes to investigate frozen ground in multi-year, interannual, and seasonal scales are presented in Chapter 3–5.

The GNSS-IR measurements of surface elevation changes can also be used to evaluate the potential risk on the infrastructures, such as buildings, roads, and pipelines, imposed by permafrost degradation. Large residential communities, for instance, Utqiagvik in Alaska and Yakutsk in east Siberia, are located in the thawing-permafrost-disturbed areas. Permafrost degradation can lead to ground settlement and slope failures, such as active layer detachment (Kokelj and Jorgenson, 2013). It negatively affects the living conditions and sustainable development of the local communities. The GNSS-IR measurements can serve as a first-order estimation of ground deformation at local scales, which can assess the severity of the potential damage to the infrastructures. Moreover, the simulations of surface subsidence and ground bearing capacity under the climate scenarios of the Intergovernmental Panel on Climate Change (IPCC) have been conducted to evaluate the potential hazard (Nelson et al., 2002; Shiklomanov et al., 2017; Streletsckiy et al., 2019). The GNSS-IR measurements can be used to validate the simulated results and contribute to calibrate the model parameters.

2.4.3 Limitations of the suitable sites in non-continuous permafrost areas

Seven usable GNSS sites are located in discontinuous permafrost areas, and two in sporadic regions. The discontinuous permafrost zonation indicates that 50–90% of the land is underlain by permafrost. Less than 50% of areas are underlain by permafrost

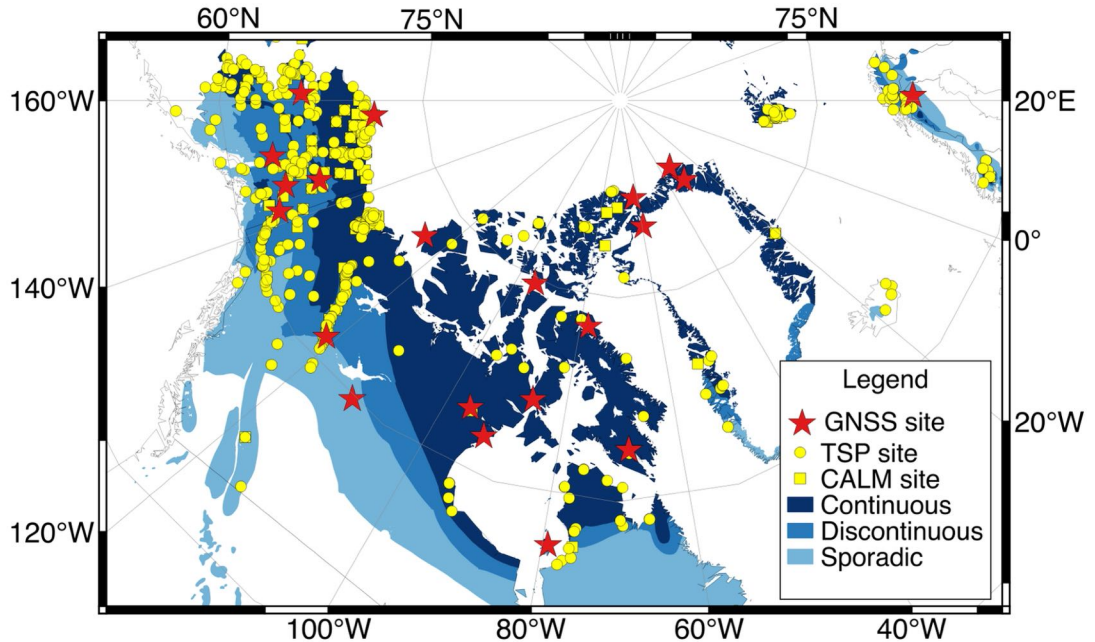


Figure 2.5: Locations of the identified usable GNSS sites in the Arctic permafrost areas. We also present the CALM and TSP sites.

in sporadic zones. In other words, it is unsure whether the permafrost exists at these nine sites.

In seasonally frozen ground regions, the soil underneath the layer undergoing seasonal freezing and thawing may have different geotechnical properties from those of permafrost. Surface elevation changes could be contributed by other processes except for the phase changes of soil moisture. Therefore, examining permafrost presence should be conducted initially. Empirical approaches can be used to have a first-order estimation. For instance, with a large possibility, the permafrost exists at a site when the mean annual air temperature (MAAT) is lower than -2°C (French, 2007). Numerical simulations can also predict the permafrost existence and active layer thickness, which, however, are complex and need ancillary data such as vegetation, snow depth, soil texture, and soil moisture. Instruments can then be installed to measure ground

temperature to validate the estimation.

Talik should be considered as well, which is a part of permafrost but in an unfrozen state. It usually occurs in discontinuous and sporadic permafrost zones. Due to its unfrozen state, its geotechnical properties might differ from the frozen ground, which possibly affect the volume changes of the freezing/thawing active layer. Surface elevation changes might not directly reflect the changes in the active layer.

2.5 Conclusion

In this study, we identified 23 usable sites, with nearly all of them located in northern Canada and Alaska. We also obtained and published their reflector heights, which can be converted into surface elevation changes on snow-free days and snow depth otherwise. Nine of these usable sites are in non-continuous permafrost zones, at which surface elevation changes might not directly reflect frozen ground dynamics, as it is unsure whether the permafrost exists.

The obstructions and undulated surfaces are the dominant reasons for the unusable sites. Sixty-eight percent of the unusable sites are located on the undulated surface, and 25% are surrounded by obstructions. The rest of 7% are due to insufficient usable SNR series, though they have open and relatively flat areas. Better location choices are recommended for installing GNSS sites in the future. We also urge that detailed information of the monument and surrounding environment can be recorded. The identified suitable and unsuitable sites and their features, including topography, landcover, and vegetation, can be utilized to build models, such as a machine-learning-based model, to automatically assess the suitability of a site for GNSS-IR applications.

The possible error sources of the GNSS-IR measurements of surface elevation changes, including tropospheric delay, antenna gain pattern, monument thermal ex-

tension and contraction, foundation stability, soil moisture variation, and vegetation are discussed in detail.

The usable sites can fill some spatial gaps of the existing permafrost monitoring programs and provide complementary measurements to active layer thickness and permafrost temperatures. The GNSS-IR measurements can provide new perspectives for studying frozen ground dynamics and assess the potential hazard of permafrost degradation to infrastructures. They also help making appropriate strategies and policies to increase the resilience of resident communities to adapt to the ever-changing permafrost environment.

End of chapter.

Chapter 3

Investigating frozen ground dynamics in the Canadian Arctic by GNSS-IR-estimated surface elevation changes¹

3.1 Introduction

Permafrost has been suffering from warming and thawing since the International Polar Year of 2007–2009 (Smith et al., 2009; Biskaborn et al., 2019). Based on in situ measurements, the ground temperature at or near the depth of zero annual amplitude increased by 0.39 ± 0.15 °C in the continuous permafrost and 0.20 ± 0.15 °C in the discontinuous one during 2007–2016. Permafrost degradation typically leads to ground ice melting, active layer thickening, ground settlement, and release of pre-

¹This chapter is based on Jiahua Zhang, Lin Liu, and Yufeng Hu. (2020). Global Positioning System interferometric reflectometry (GPS-IR) measurements of ground surface elevation changes in permafrost areas in northern Canada. *The Cryosphere*, 14(6), 1875–1888. <https://doi.org/10.5194/tc-14-1875-2020>

viously stored carbon, consequently affecting the hydrological, geomorphological, and biogeochemical processes (Shur and Jorgenson, 2007; Lantuit and Pollard, 2008; Kokelj and Jorgenson, 2013; Schuur et al., 2015; Hjort et al., 2018).

The ground surface in a permafrost area is subject to uplift/subsidence due to active layer freezing/thawing. Surface elevation changes are closely linked with water and heat changes in the active layer and near-surface permafrost. The GNSS-IR can provide daily and continuous vertical surface deformation at permanently operating stations. In Chapter 2, we have identified 23 sites which are located in the Arctic permafrost areas and usable for GNSS-IR studies. From them, we select five stations, namely ALRT in Alert, RESO in Resolute Bay, REPL in Repulse Bay, BAKE in Baker Lake, and IQAL in Iqaluit, in Canada. These sites are all located in continuous permafrost regions and have stable monuments deep anchored into the solid earth. Moreover, these sites have been operating for multiple years. The multi-year, continuous, and daily GNSS-IR measurements of vertical surface movement can be obtained to study frozen ground dynamics in various temporal scales.

In the rest of this chapter, we summarize the basic information of the five selected sites, including biomes and surficial materials in section 3.2. We then show the results of GNSS-IR-measured surface elevation changes in thawing seasons at each site in section 3.3. We then interpret the results to reveal frozen ground dynamics in various temporal scales in section 3.4. We conclude this study in section 3.5.

3.2 Study sites

The GNSS stations of ALRT, RESO, REPL, BAKE, and IQAL are located in open and relatively flat and horizontal areas. We show their ground photos in Fig. 3.1. Their surface conditions are favorable for coherent reflections and clear sinusoidal patterns of SNR observations. We exhibit the SNR observations within the determined az-

imuth range and their corresponding frequency spectrums of each site in Fig. 3.2 . We can observe that the SNR interferograms have clear sinusoidal patterns and their dominant reflector heights are consistent at all of these sites. The basic information of the GNSS sites has been presented in Table 2.1.

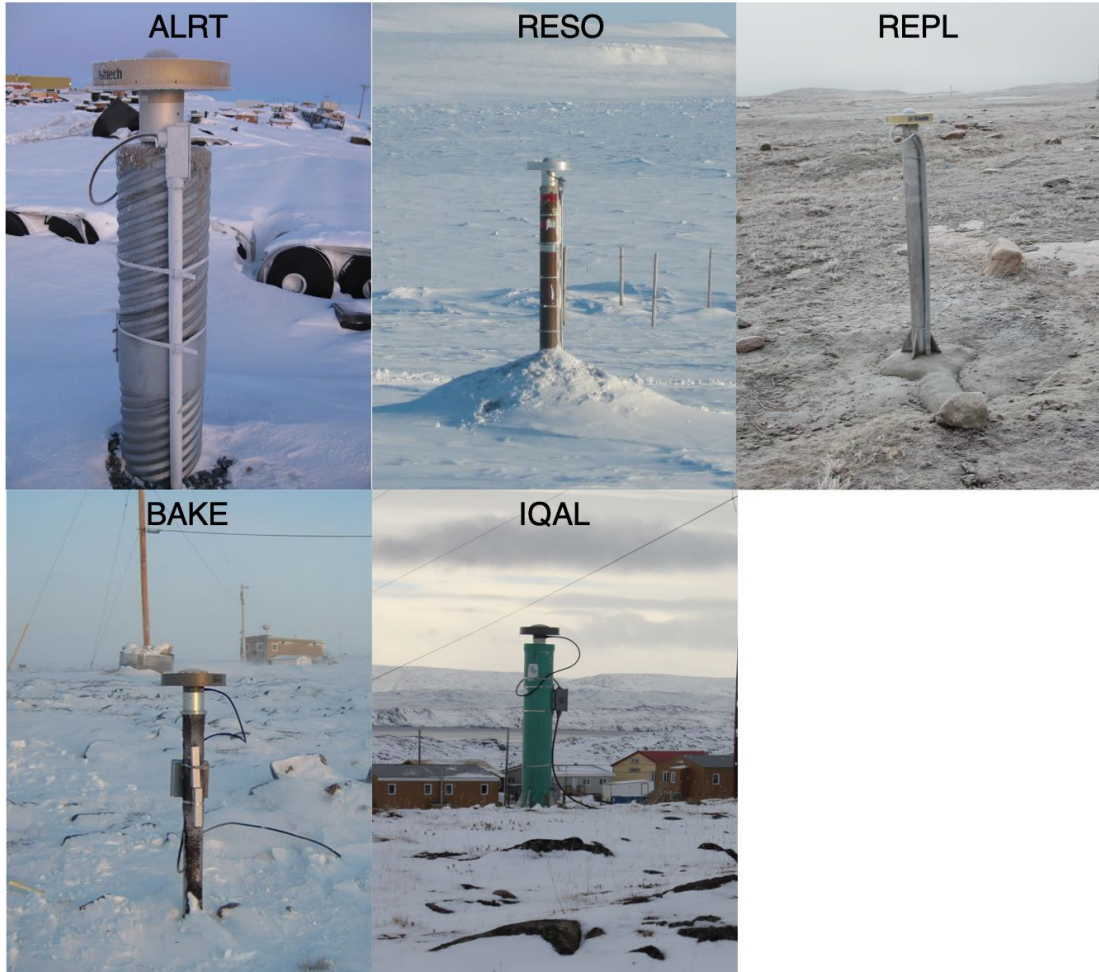


Figure 3.1: Ground photos of the GNSS sites of ALRT, RESO, REPL, BAKE, and IQAL.

These five sites are all located in the Canadian Arctic. Due to high latitude, the climate in this region is dominantly Polar climate. The biomes are mainly tundra and Arctic desert. The permafrost in this region is continuous, and its thickness normally increases with latitude. In the far north latitude of 75° N, the permafrost can be thicker

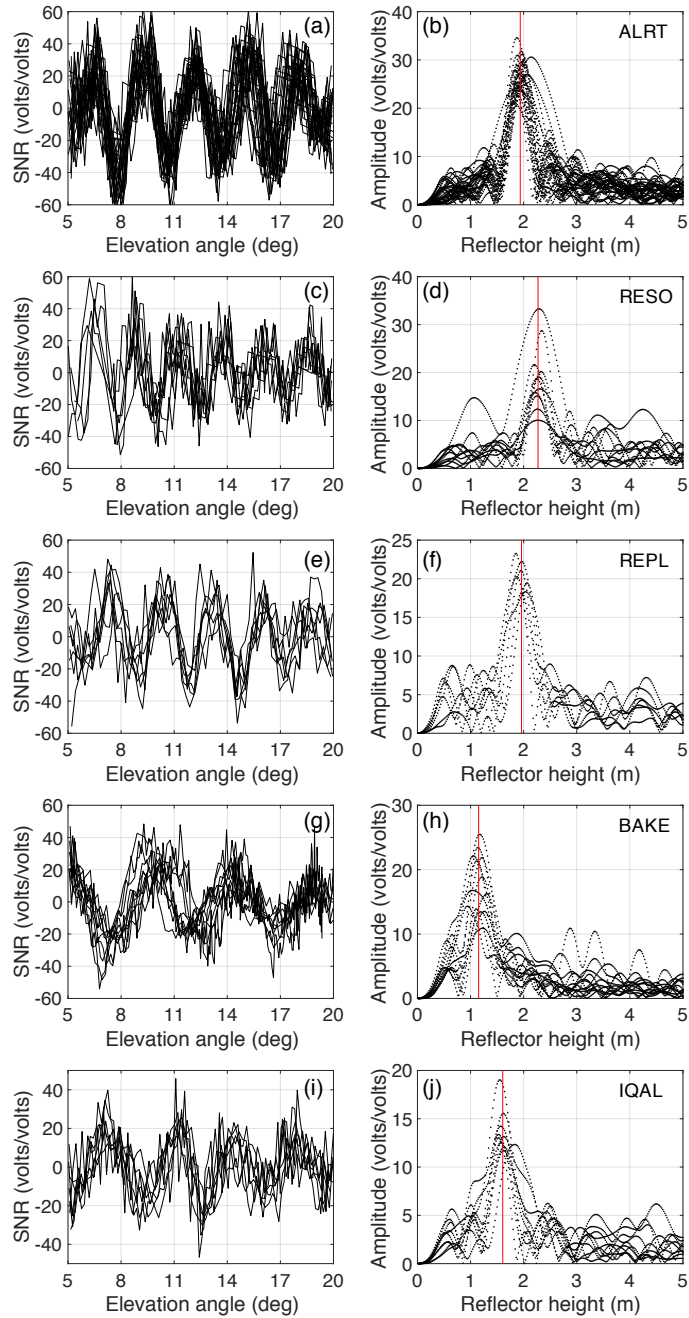


Figure 3.2: SNR observations and their corresponding LSP spectrums at ALRT, RESO, REPL, BAKE, and IQAL. The frequency has been converted into reflector height. The red vertical line denotes the mean value of the dominant reflector heights with peak amplitudes.

than 500 m (Sladen, 2011). Ground temperatures at or near the depth of zero annual amplitude range from colder than -15 °C to warmer than -2 °C, and they decrease northward in accordance with climate (Smith et al., 2013). During 2008–2014, ground temperatures at the depth of 15 m increased at an average rate of $\sim 0.17\text{ }^{\circ}\text{C}\cdot\text{yr}^{-1}$ at ten extensively distributed sites in the Canadian Arctic (Ednie and Smith, 2015).

We summarize the basic information of the five sites in Table 3.1, including biome, land cover, ground ice content of near-surface permafrost, MAAT, and mean annual ground temperature (MAGT). The MAAT was based on the air temperature records during 1981–2010 from Environment Canada (http://climate.weather.gc.ca/climate_normals/index_e.html). The MAGT was measured at or near the depth of zero annual amplitude (Smith et al., 2013; Ednie and Smith, 2015). The ground ice content was simulated by using surficial geology, deglaciation, paleo-vegetation, glacial lake and marine limits, and modern permafrost distribution (O’Neill et al., 2019). In Alert and Resolute Bay, the biomes are both Arctic Desert due to the high latitude. The biomes at the other three sites are all tundra. But, due to their specific locations, the ground surface is mainly bare soil in Repulse Bay, but covered by a peat layer in Baker Lake, and sparsely vegetated in Iqaluit.

Table 3.1: Basic information of the study sites.

Site	Alert	Resolute Bay	Repulse Bay	Baker Lake	Iqaluit
Biome	Polar desert	Polar desert	Tundra	Tundra	Tundra
Land cover	Mainly silts, sands, and shattered rocks filled with ice, ranging from 2.4 to 4 m thick (Taylor et al., 1982).	Rounded or angular gravels and shelly and fine-grained sands (Cruickshank, 1971).	Sands and silts ranging from 1 to 10 m thick (Dredge, 1994).	Coarse gravels and sands with low ice contents underneath a peat layer (Throop et al., 2010).	A thin till veneer with fairly well-developed soil, with sparse vegetation (Throop et al., 2010).
Ground ice content of near-surface permafrost	None	Negligible wedge ice and low segregated ice	None	Negligible wedge and segregated ice	Low wedge, segregated, and relict ice
MAAT (°C)	-18.0	-15.7	-12.1	-11.8	-9.8
MAGT (°C)	-11.1 to -14.4 (2007–2011)	-11.9 (2008–2012)	-8.2 (2009–2013)	-7.9 (2006–2006)	-5.6 to -7.1 (2003–2004 and 2011–2012)

3.3 Results

We used the reflector heights in thawing seasons to obtain surface elevation changes at each study site. In a thawing season, air temperature is above 0 °C, and the ground is not covered by snow. We present the multi-year time series of surface elevation changes at each site in Fig. 3.3. The surface elevation changes in each year at each site are presented in Figs. 3.4–3.8.

For the multi-year observations, we built their best linear fit and obtained the trend of vertical surface deformation. We found that the ground surface underwent a trend of settlement by $0.61 \pm 0.04 \text{ cm}\cdot\text{yr}^{-1}$ during 2012–2018 in Alert, $0.70 \pm 0.02 \text{ cm}\cdot\text{yr}^{-1}$ during 2003–2014 in Resolute Bay, $0.17 \pm 0.02 \text{ cm}\cdot\text{yr}^{-1}$ during 2010–2020 in Baker Lake, and $0.10 \pm 0.02 \text{ cm}\cdot\text{yr}^{-1}$ during 2010–2020 in Iqaluit. The rate for Repulse Bay was $0.01 \pm 0.04 \text{ cm}\cdot\text{yr}^{-1}$ during 2014–2020, which is not statistically significant (t-test, $\alpha = 0.05$).

As for the seasonal variation, the ground surface in a permafrost area typically subsides progressively in a thawing season and reaches its lowest position at the end of thaw. In Alert, we observed such typical variation in 2012 and 2014, whereas the surface kept relatively stable in 2013 and 2015. In other years, the measurements were noisy so that it is challenging to observe their seasonal trends. In Resolute Bay, the surface elevation changes were irregular as well. We only observed the typical seasonal subsidence in a few years, such as 2006 and 2012. Moreover, we found a significant uplift in the middle of the thawing season, for example, in 2003 and 2007. Regarding Repulse Bay, the summer heave could also be observed in 2015, 2016, 2019, and 2020. No significant vertical deformation occurred in 2017. The measurements in 2014 were noisy and obscured the seasonal variations. In Baker Lake, the typical seasonal variations could be found in 2010, 2012, 2016, 2017, and 2020. The ground surface was relatively stable in 2014, 2015, 2018, and 2019. Large data gaps existed in 2011 and 2013. In Iqaluit, we observed the typical trend in 2010, 2011, 2015, and

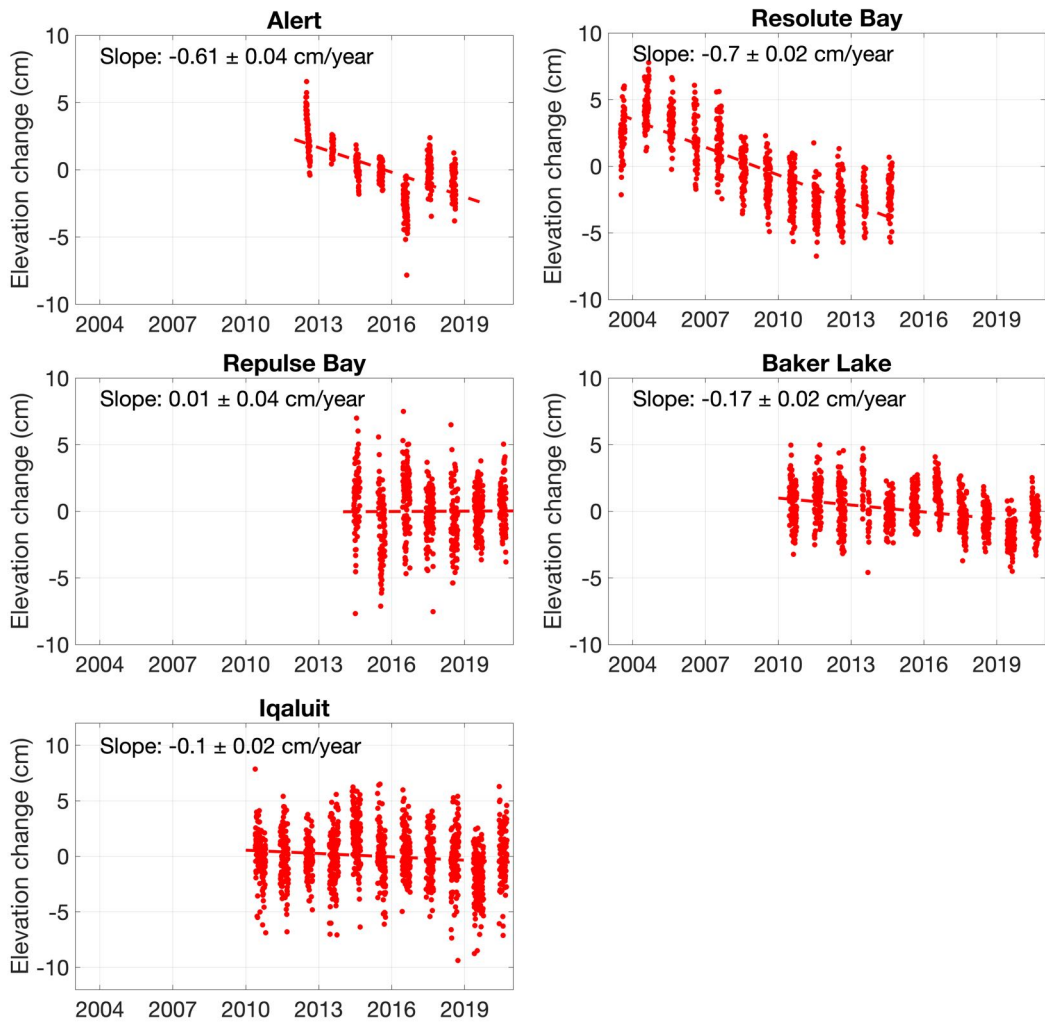


Figure 3.3: Time series of surface elevation changes in Alert, Resolute Bay, Repulse Bay, Baker Lake, and Iqaluit. For each site, the reference is the mean value of the measurements over the entire data time span. We also present the best linear fits of the measurements and their slopes for each site.

2016. The ground surface kept relatively steady in 2012, 2014, 2017, 2019, and 2020. The summer heave occurred in 2013 and 2018 as well. To sum up, at nearly all sites, the GNSS-IR measurements in most years were irregular and inconsistent.

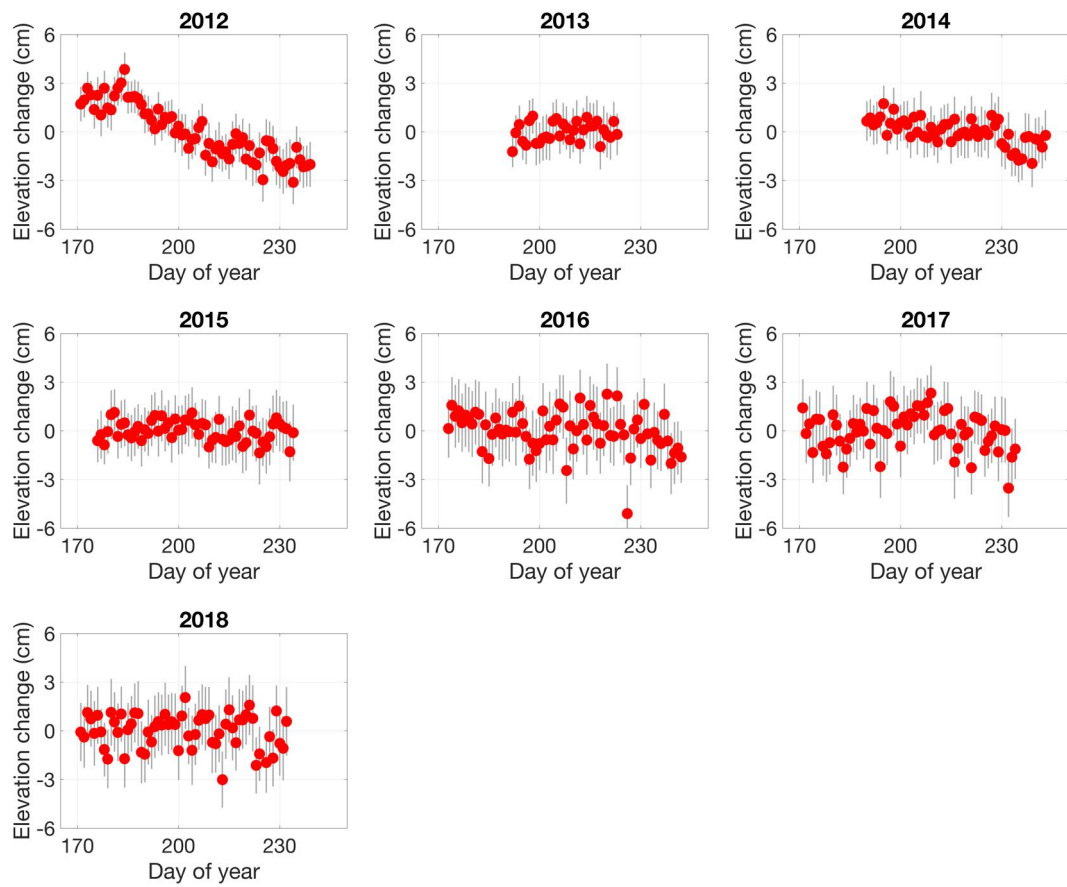


Figure 3.4: Surface elevation changes in each thawing season with the reference as their mean value during 2012–2018 in Alert.

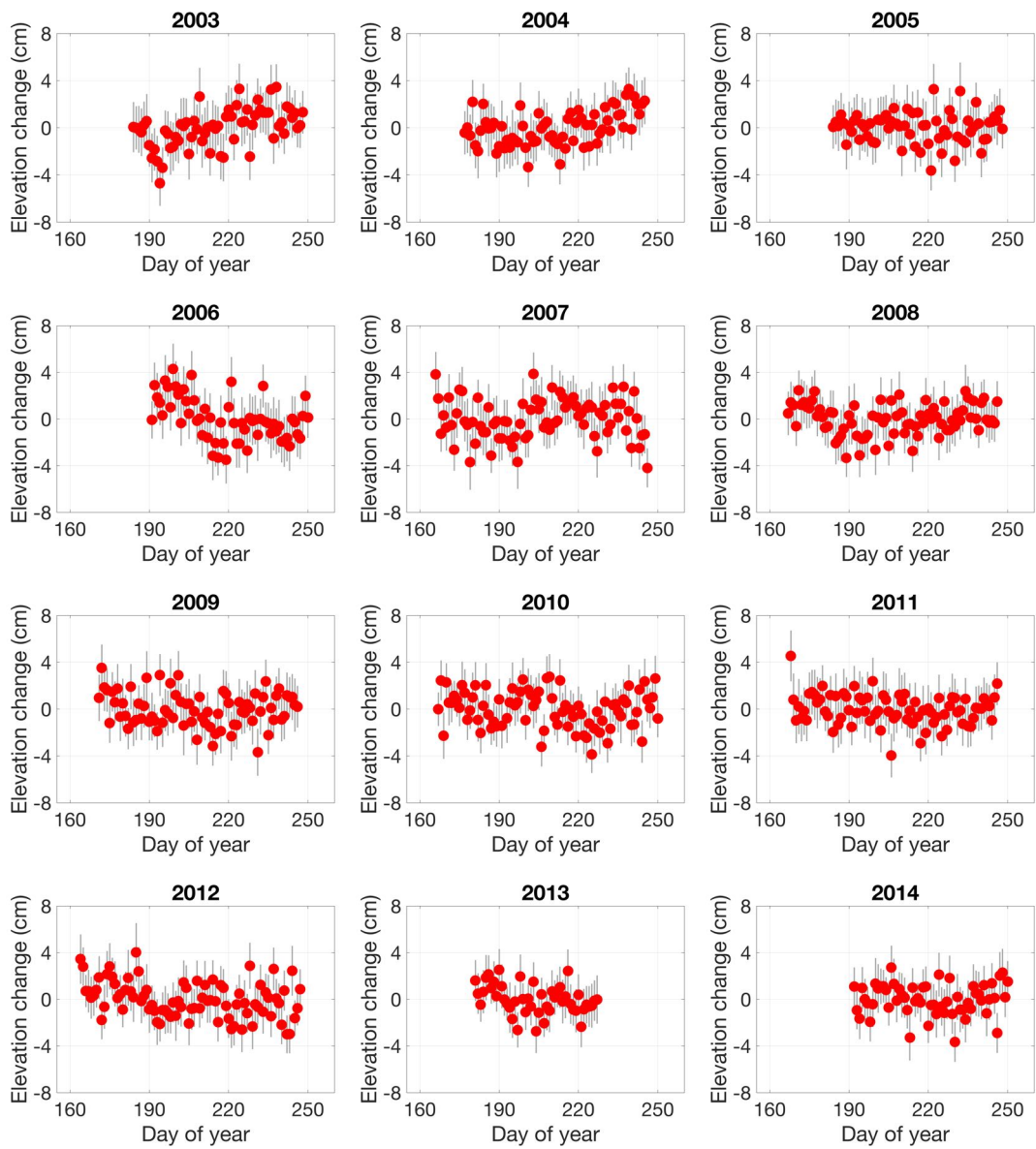


Figure 3.5: Similar to Fig. 3.4 but for Resolute Bay.

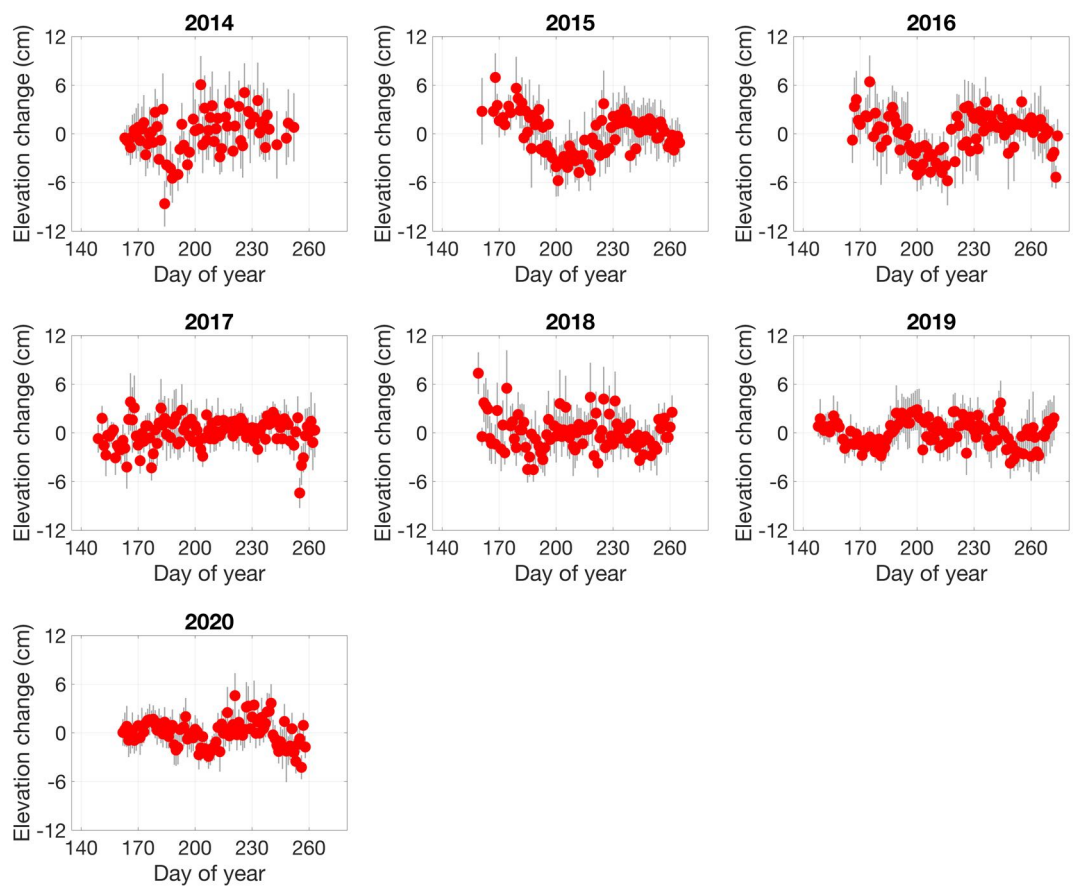


Figure 3.6: Similar to Fig. 3.4 but for Repulse Bay.

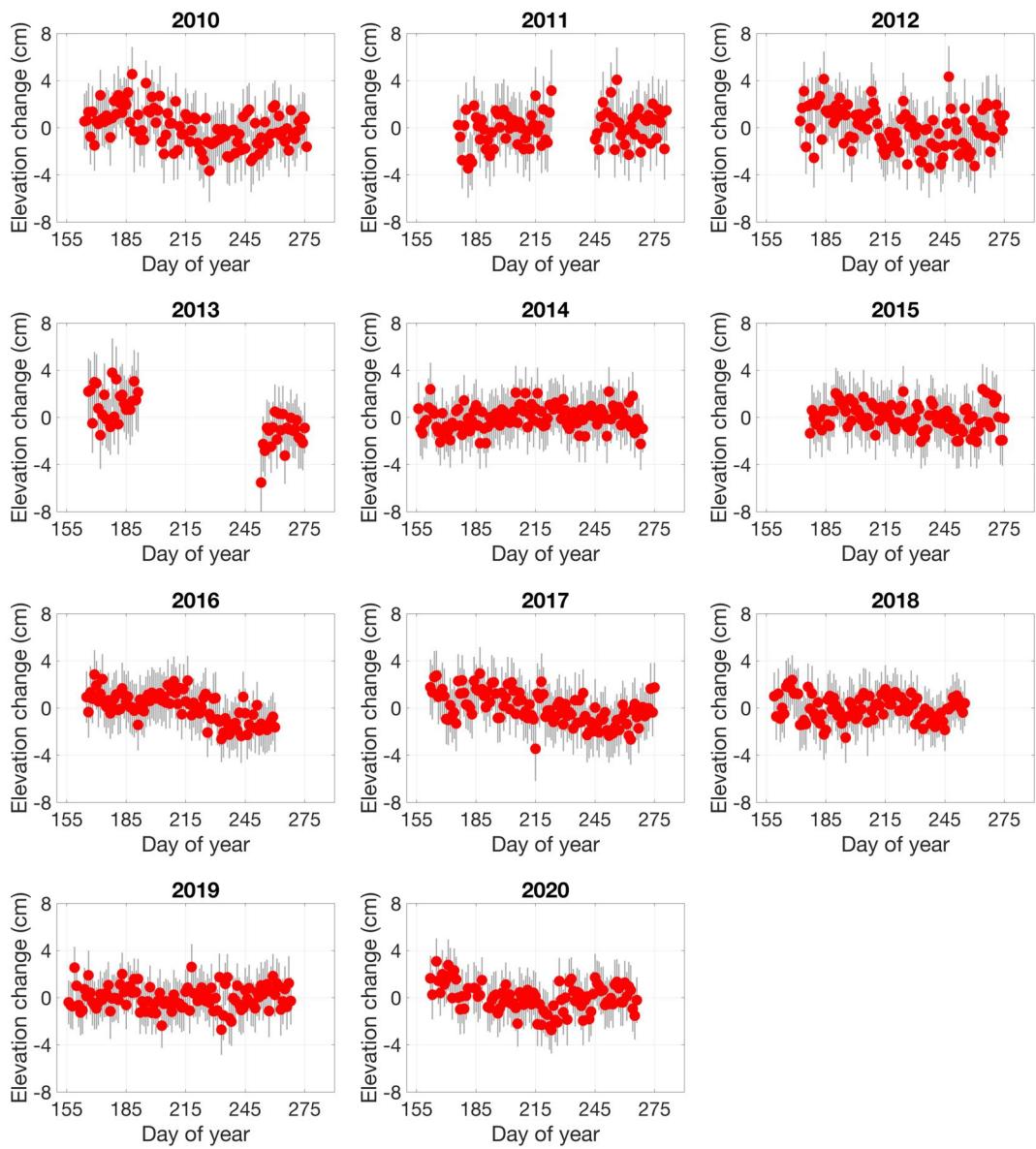


Figure 3.7: Similar to Fig. 3.4 but for Baker Lake. Data gaps exist in 2011 and 2013.

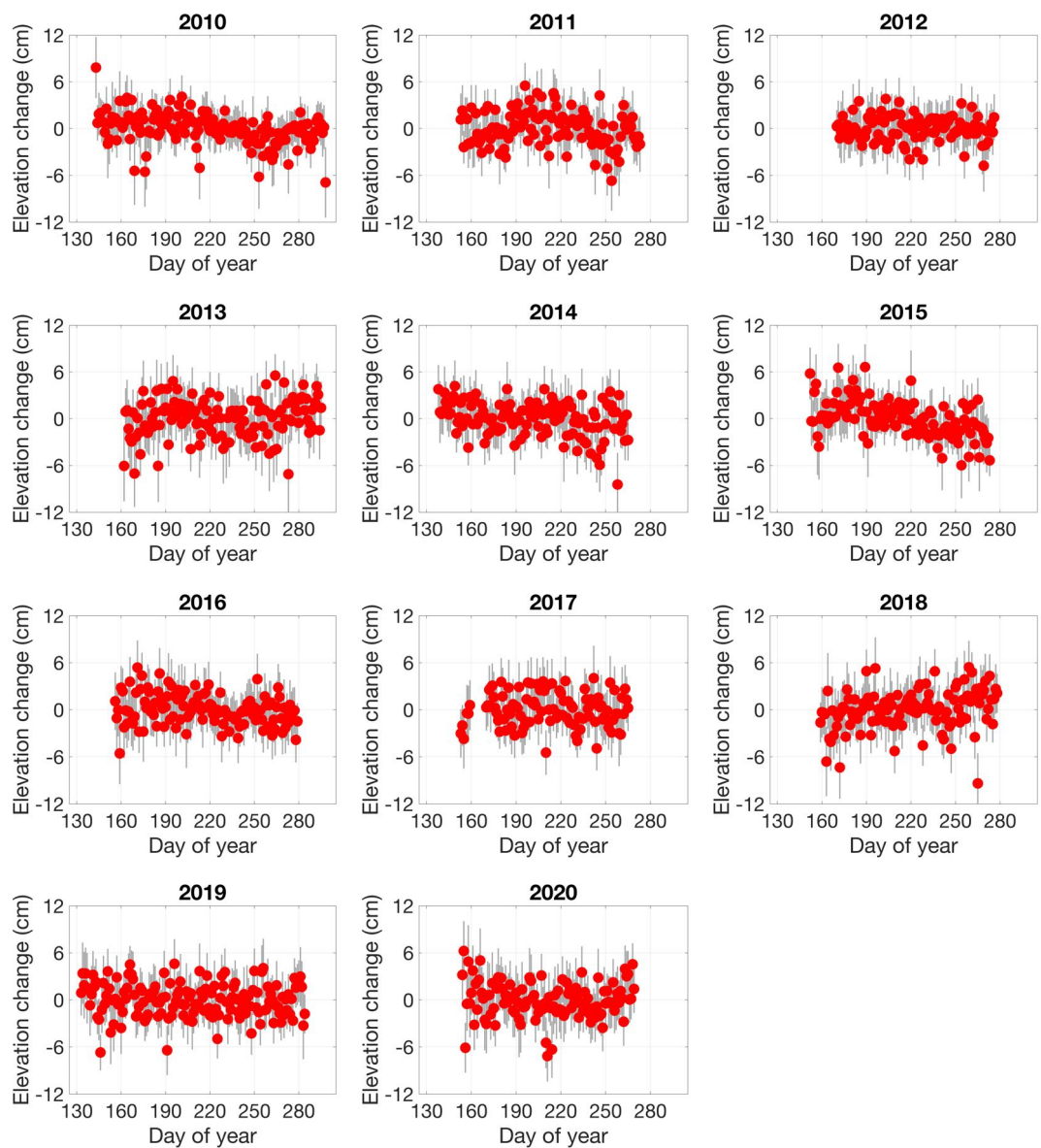


Figure 3.8: Similar to Fig. 3.4 but for Iqaluit.

3.4 Discussion

3.4.1 Multi-year linear trends of surface elevation changes

We here probe into the linkage between the multi-year linear trends of surface elevation changes and environmental variables, including air temperature, landcover, and ground ice content near the permafrost table. The Stefan equation in section 1.2.2 characterizes surface vertical deformation by soil properties and thawing index. At each site, we calculated the annual DDTs and their mean value and linear trend, by using the air temperatures recorded by the nearby weather station (Table 3.2). We found that the thawing seasons became warming by $9.35 \text{ }^{\circ}\text{C}\cdot\text{day}\cdot\text{yr}^{-1}$ during 2012–2018 in Alert, $8.17 \text{ }^{\circ}\text{C}\cdot\text{day}\cdot\text{yr}^{-1}$ during 2003–2014 in Resolute Bay, $59.33 \text{ }^{\circ}\text{C}\cdot\text{day}\cdot\text{yr}^{-1}$ during 2014–2020 in Repulse Bay, and $5.47 \text{ }^{\circ}\text{C}\cdot\text{day}\cdot\text{yr}^{-1}$ during 2010–2020 in Baker Lake. Whereas, Iqaluit underwent cooling summers by $-7.93 \text{ }^{\circ}\text{C}\cdot\text{day}\cdot\text{yr}^{-1}$.

The ground surface underwent multi-year linear subsidence under warming thawing seasons in Alert, Resolute, and Baker Lake. From Table 3.1, the biomes in Alert and Resolute Bay are Polar desert characterized by bare soil, and the ground ice content is limited based on the field surveys and model simulations. Such conditions facilitate the heat transfer from air into the frozen ground. In warming thawing seasons, the rising air temperature warms the frozen ground at the deeper depth (i.e., the transient layer freezing and thawing seasonally to centennially (Shur et al., 2005)), causing ground ice melting and surface settlement. Baker Lake is in a tundra environment. Its top material is dominantly coarse gravels filled with sand underneath a peat layer. Its ground ice content is negligible as well. Similar processes to those in Alert and Resolute Bay were supposed to happen to thaw the deeper frozen ground, melt the ground ice, and lead to surface subsidence. Contrarily, Iqaluit underwent ground settlement in cooling thawing seasons. Its top soil layer is a thin till veneer with fairly developed soil. The ground ice is low rather than negligible. The soil properties and

ground ice condition are the possible reasons for the multi-year subsidence in cooling summers. The linear trend of vertical surface movement in Repulse Bay is not discussed, as it is not statistically significant. Liu and Larson (2018) obtained surface elevation changes in July and August in each year during 2004–2015 at Utqiagvik, Alaska by using GNSS-IR, and found a subsidence trend of $0.26 \pm 0.02 \text{ cm}\cdot\text{yr}^{-1}$. Over the same time span, the thawing seasons had a warming trend of $4.79 \text{ }^{\circ}\text{C}\cdot\text{day}\cdot\text{yr}^{-1}$. It is consistent with our findings in Alert, Resolute, and Baker Lake: warming thawing seasons lead to surface subsidence.

In addition to air temperature, soil moisture content also has a significant influence on frozen ground dynamics (Wang et al., 2020). Göckede et al. (2019) observed a cooling effect in the active layer at a drainage site compared with a nearby saturated site. The soil moisture affects soil thermal properties, then active layer thickness, consequently surface elevation changes. However, it is challenging to evaluate the contribution of moisture changes to the surface deformation, as the records including soil moisture content, ground temperature, and active layer thickness, are not available. On the other hand, the study sites are all located in the continuous permafrost regions characterized by cold and dry climates. We do not expect that they underwent significant changes in soil moisture content.

Table 3.2: Statistics of the annual DDT in Alert, Resolute Bay, Repulse Bay, Baker Lake, and Iqaluit.

Site	Data time span	Mean ($^{\circ}\text{C}\cdot\text{day}$)	Trend of DDT ($^{\circ}\text{C}\cdot\text{day}\cdot\text{yr}^{-1}$)	Trend of surface elevation changes ($\text{cm}\cdot\text{yr}^{-1}$)
Alert	2012–2018	255.85	9.35	-0.61 ± 0.04
Resolute Bay	2003–2014	319.03	8.17	-0.70 ± 0.02
Repulse Bay	2014–2020	626.80	59.33	0.01 ± 0.04
Baker lake	2010–2020	1047.16	5.47	-0.17 ± 0.02
Iqaluit	2010–2020	725.17	-7.93	-0.10 ± 0.02

3.4.2 Seasonal surface elevation changes

The vertical surface movement was irregular in most years at each site (section 3.3). The Stefan equation is capable of characterizing surface elevation changes in permafrost areas. Here, we investigate the ability of the Stefan equation in explaining the seasonal surface vertical deformation at the study sites. We also use the average seasonal surface elevation changes to reveal the spatial heterogeneity of frozen ground among the Canadian Arctic sites.

We compared the surface elevation changes to square-root-of thawing indices in each thawing season over the data time span at each site. We also built their best linear fit and obtained the slope and correlation coefficient (Figs. 3.9–3.13). In Alert, surface elevation changes have negative correlations with \sqrt{DDT} in all years except 2013 with a coefficient of 0.21. Strong correlations exist in 2012 and 2014, which were -0.91 and -0.62, respectively. Whereas, in the other years except 2013, the correlations were weak and ranged from -0.24 to -0.11. The Stefan equation seems to have a good performance in 2012 and 2014, when surface elevation changes evolved accordingly with thawing indices. As for Resolute Bay, the correlations were positive in 2003, 2004, and 2007 whereas negative in the rest of the years. The negative correlation coefficients range from -0.02 to -0.53. The other sites present similar results. The Stefan equation cannot fully explain the surface elevation changes in most years at each study site.

The dominant reason for the failure of the Stefan equation in most years is possibly that the real conditions of the study sites cannot be represented by the simplifications which require the soil to be homogeneous and ignore the heat convection through moisture migration. Such inconsistency causes surface elevation changes deviating from the typical progressive settlement. Ancillary observations, such as the detailed description of soil profile, soil moisture, and ground ice content, are required to validate this postulation.

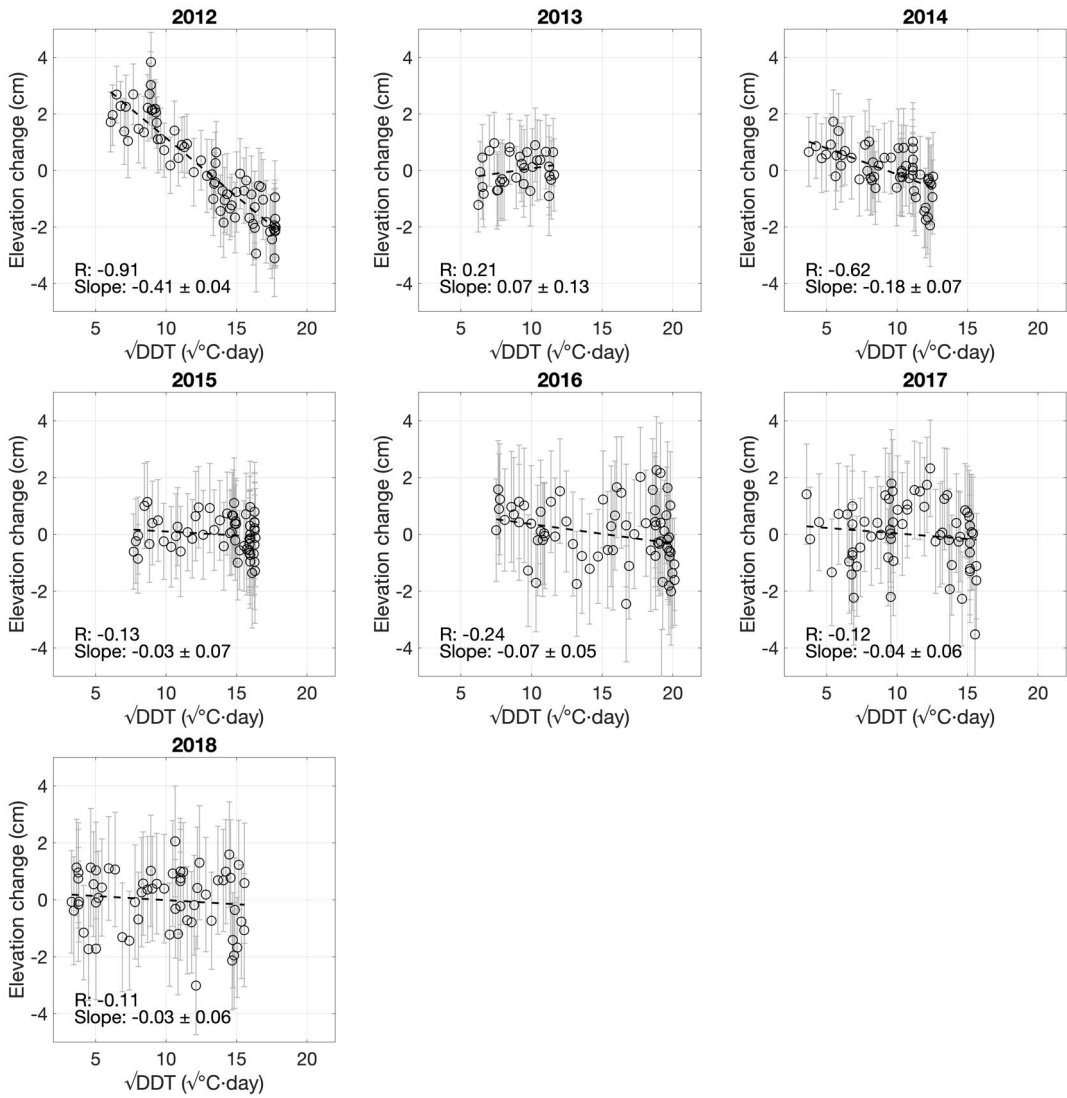


Figure 3.9: Scatter plot of surface elevation changes versus square-root-of thawing indices in each thawing season during 2012–2018 in Alert. We also build their best linear fits as dashed lines and show their correlation coefficients (R) and slopes.

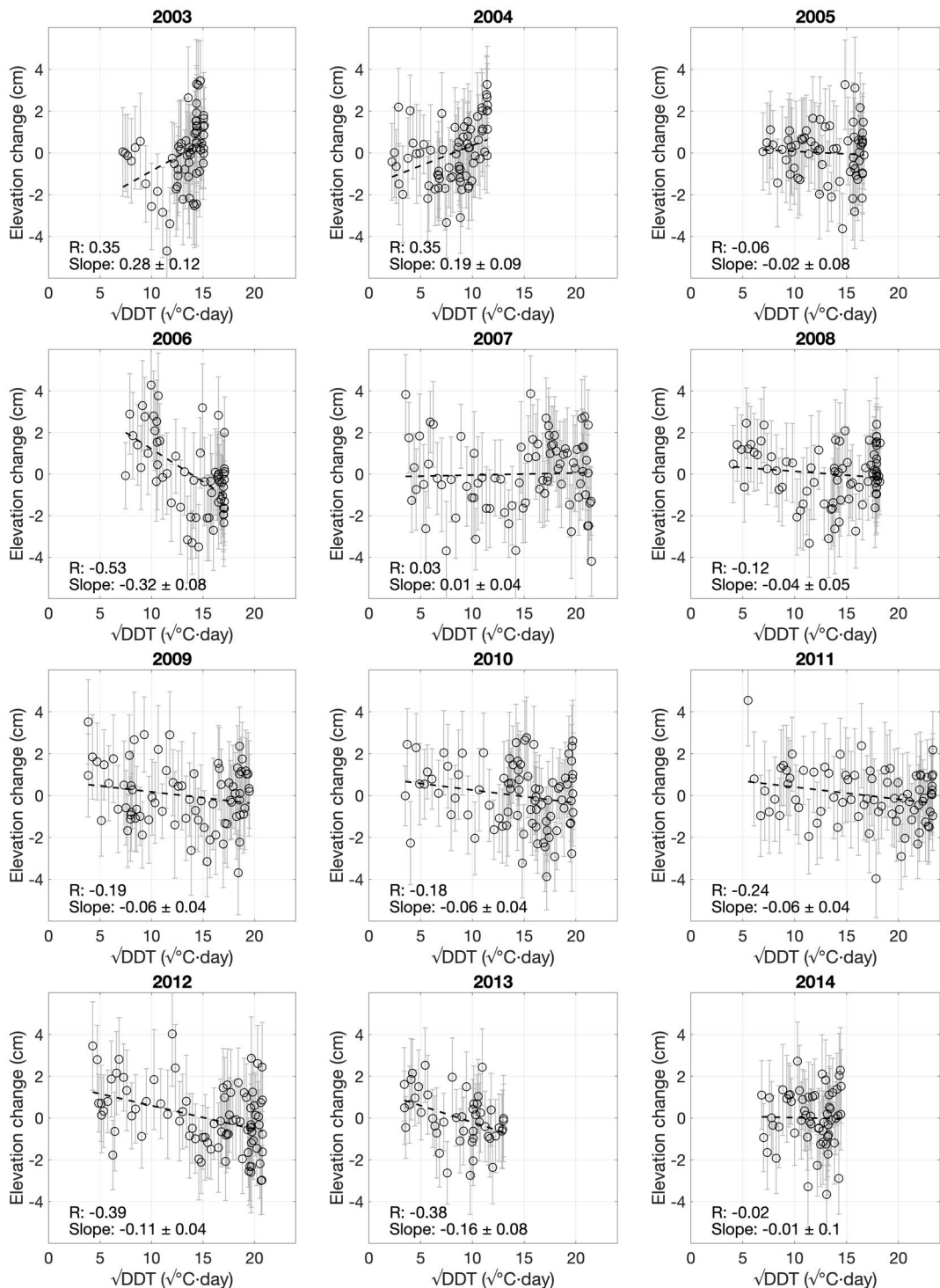


Figure 3.10: Similar figure to Fig. 3.9 but for Resolute Bay.

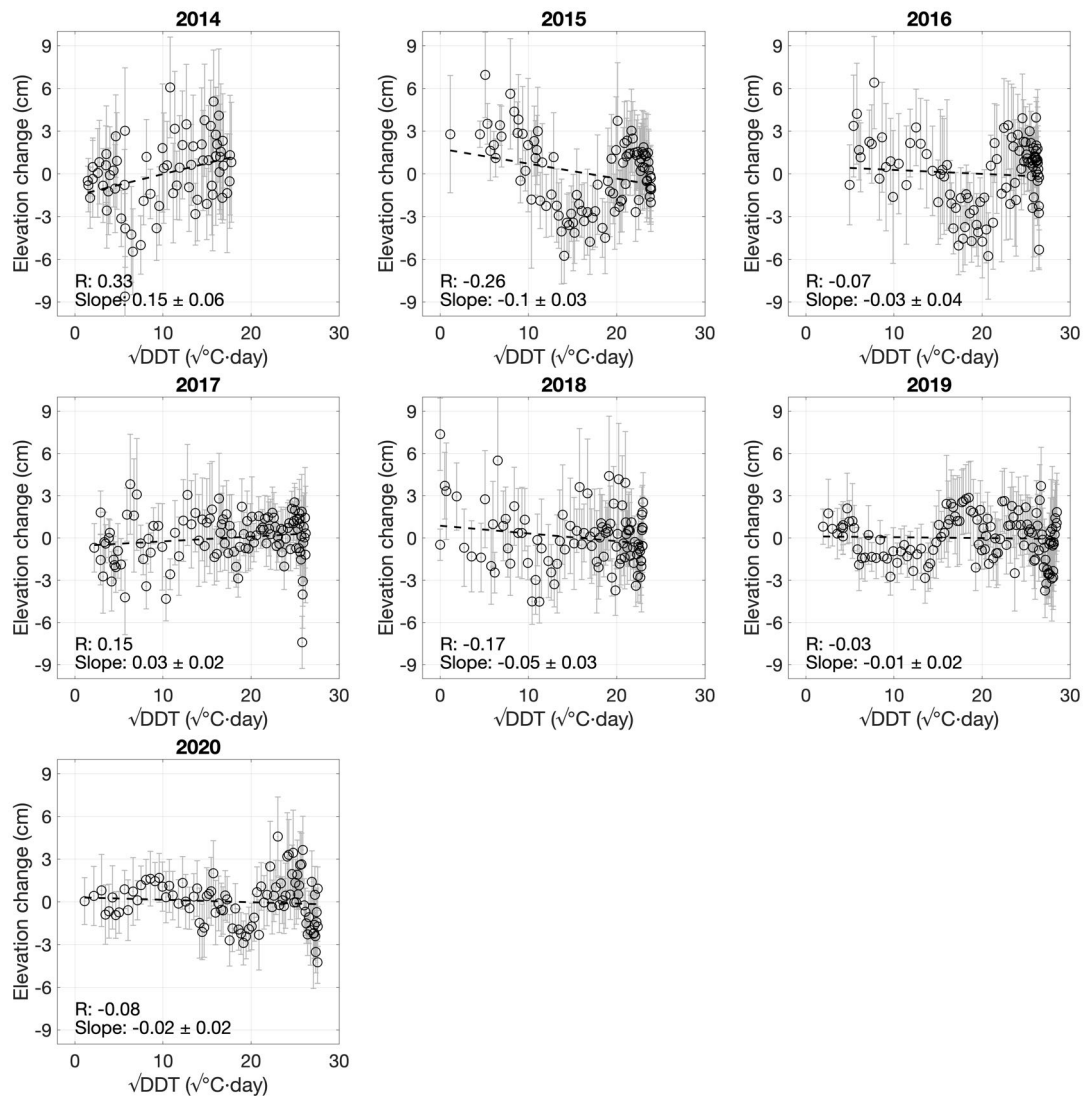


Figure 3.11: Similar figure to Fig. 3.9 but for Repulse Bay.

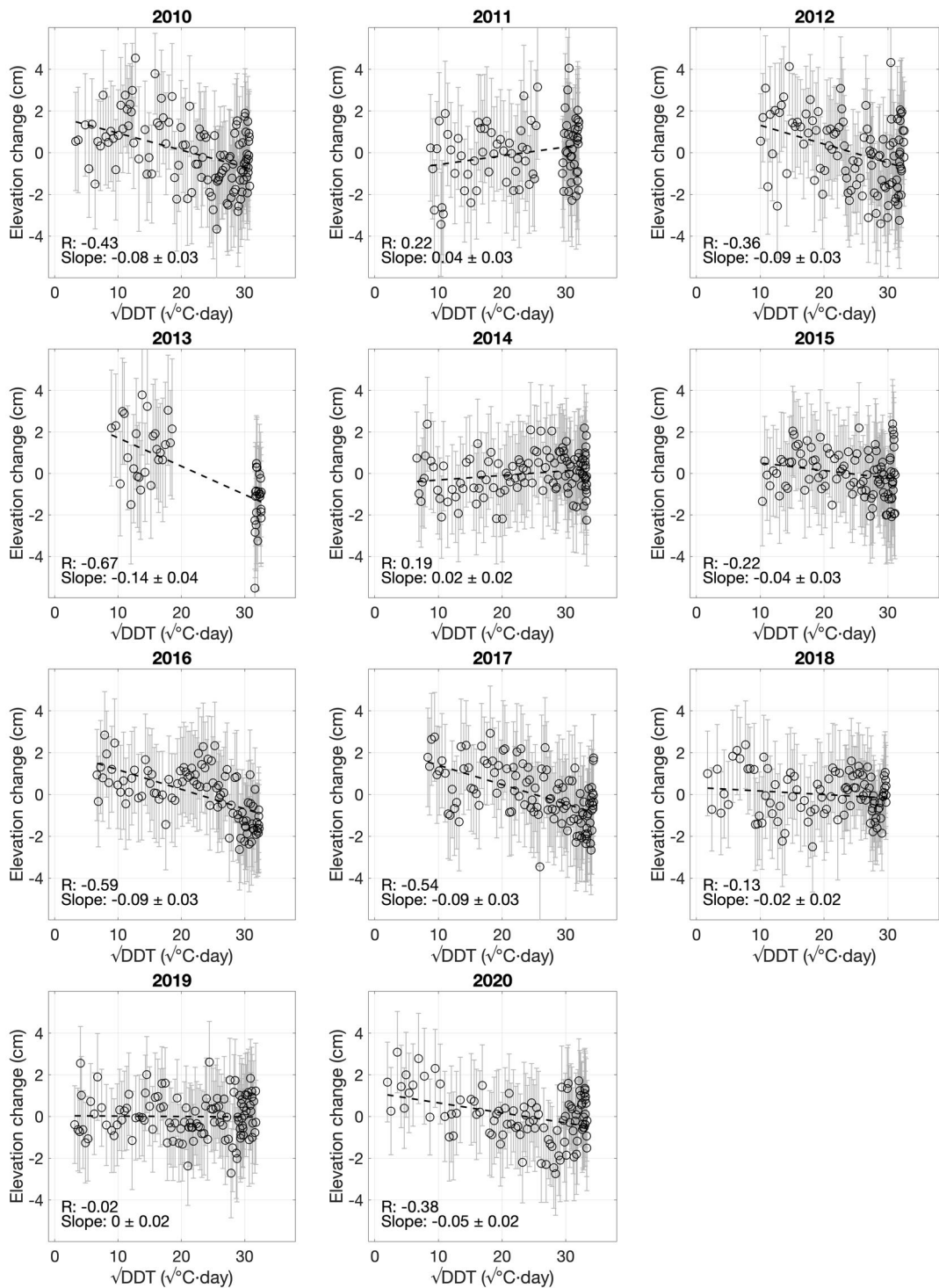


Figure 3.12: Similar figure to Fig. 3.9 but for Baker Lake.

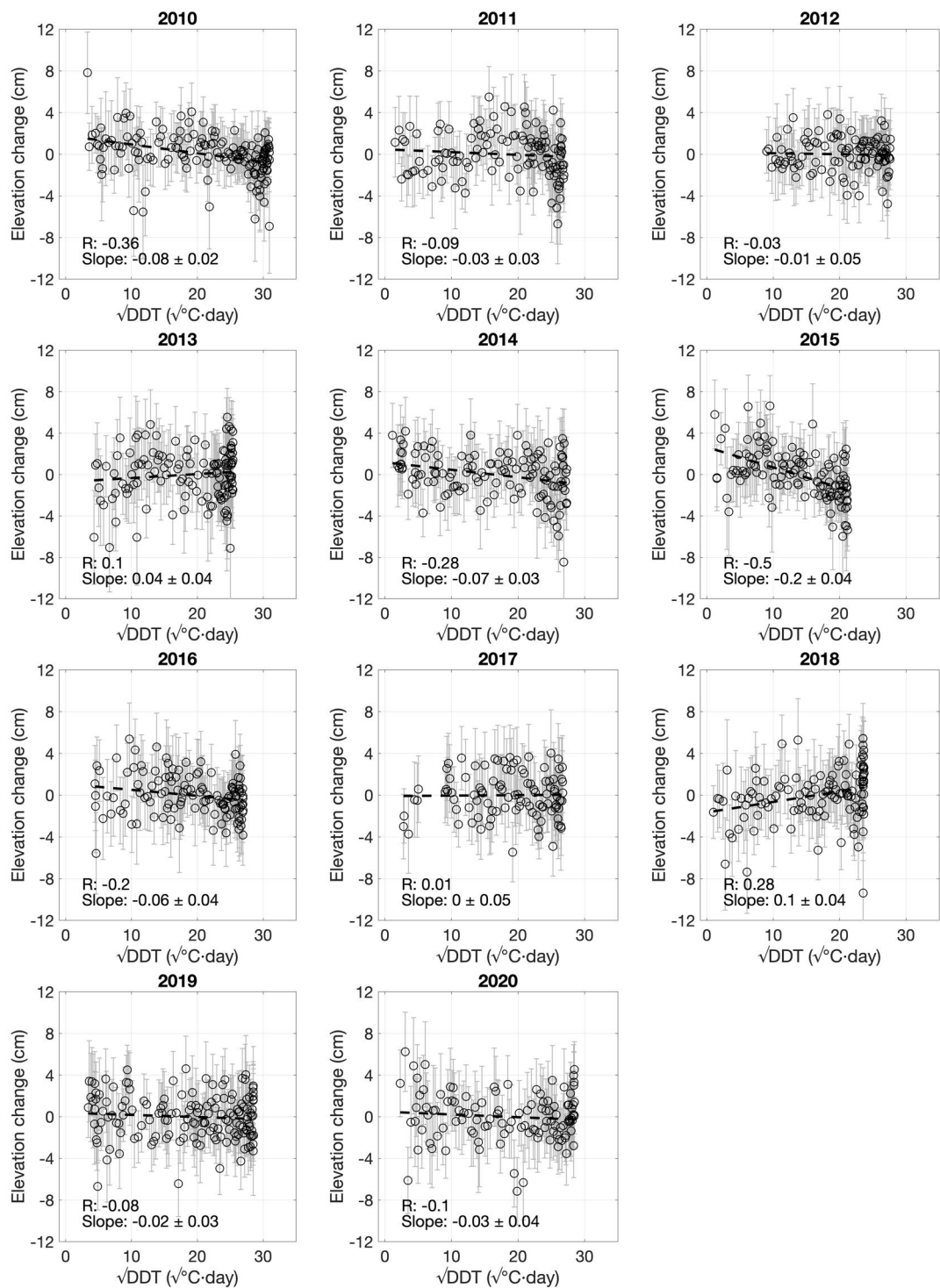


Figure 3.13: Similar figure to Fig. 3.9 but for Iqaluit.

We calculated the average seasonal surface elevation changes at each site. We first removed the multi-year linear trend then averaged them on a daily basis. We discarded the data point when the amount of samples was less than 5. The results are presented in Fig. 3.14. In Alert, the average seasonal variation show a typical progressive subsidence trend. The magnitude of the average seasonal subsidence is slightly less than 2 cm. As for Resolute Bay, the average seasonal variation present a summer heave. Moreover, an uplift occurs at the end of thawing. Regarding Repulse Bay, the average seasonal time series also present a strong summer heave. The ground surface first undergoes subsidence till the mid of thaw, then starts to uplift, subsequently subsides. For Baker Lake, the ground surface progressively subsides to the late thawing season, then slightly uplifts. In Iqaluit, the ground surface first uplifts slightly, then subsides, and heaves again slightly near the end of thawing.

We computed the average normalized square-root-of thawing indices at the study sites. At any given site, we first normalized the square-root-of thawing indices by their largest value in each season, then computed their mean values. We compared the average surface elevation changes and normalized \sqrt{DDT} . The results are presented in Fig. 3.15. The average surface elevation changes and normalized square-root-of thawing indices nearly have no correlation in Resolute Bay and Repulse Bay. Whereas, they are relatively strongly correlated in Alert and Baker Lake, with the correlation coefficients of -0.65 and -0.64, respectively. Iqaluit has a weak correlation of -0.34. Overall, the average seasonal surface movement in Alert and Baker Lake is relatively sensitive to air temperature, compared with Resolute Bay, Repulse Bay, and Iqaluit. The soil conditions in Alert and Baker Lake are possibly closer to the assumed one of the Stefan equation.

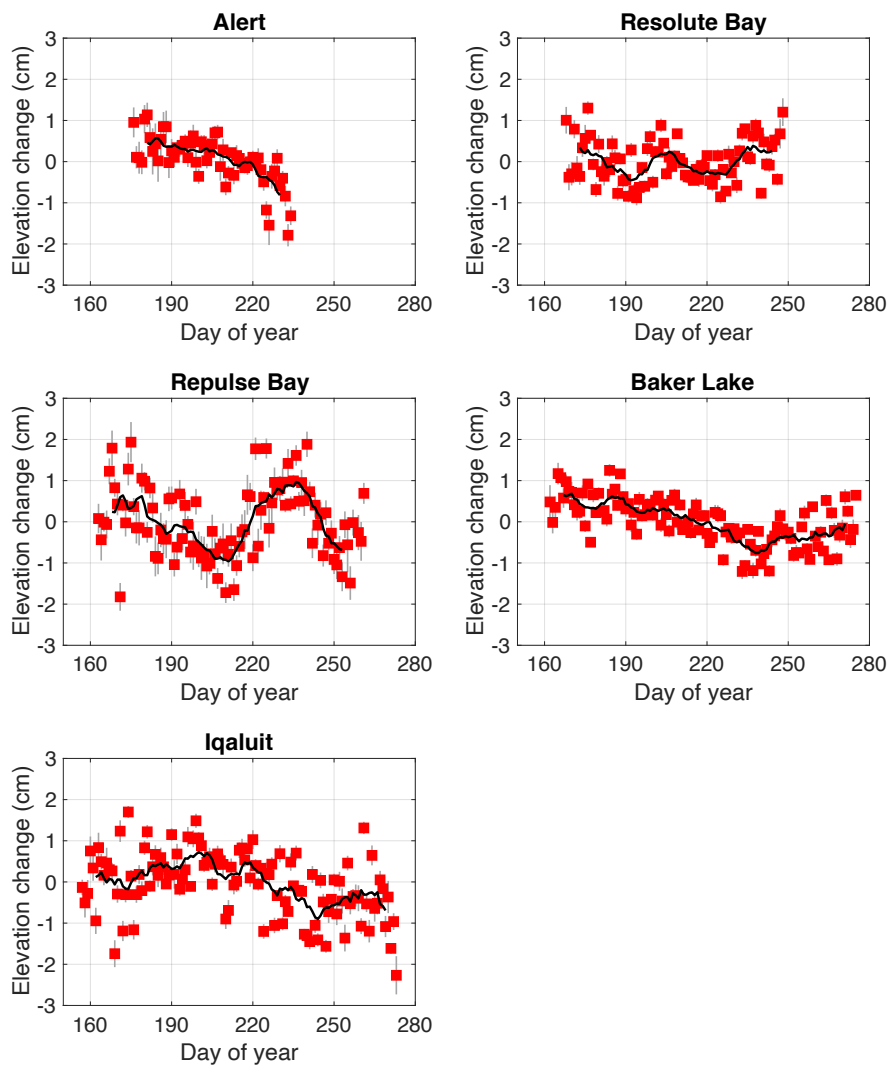


Figure 3.14: Average seasonal variations of surface elevations (as red dots) at each Canadian Arctic site. The black lines refer to the 10-day moving averages.

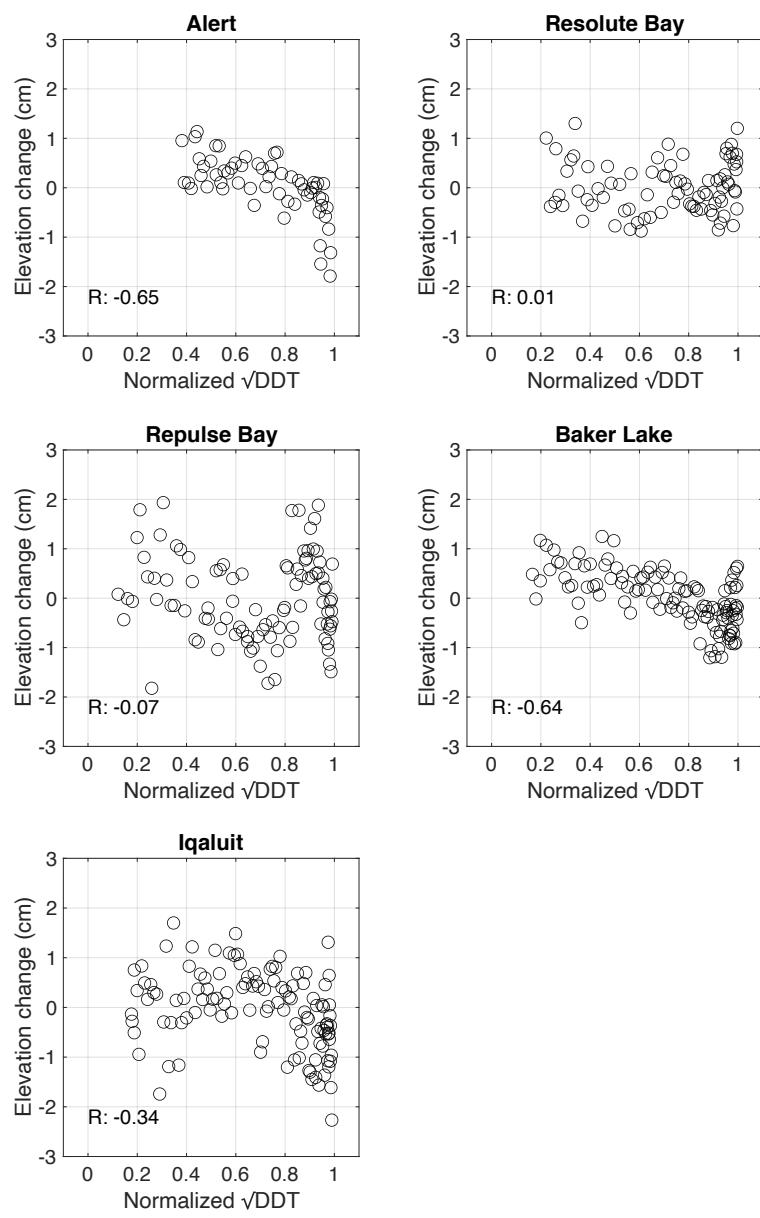


Figure 3.15: Comparison between average seasonal surface elevation changes and average normalized square-root-of-thawing indices at each Canadian Arctic site. The correlation coefficients are presented as well.

3.4.3 End-of-thaw elevations in Resolute Bay

Seasonal subsidence has the potential to reveal the thermal and hydrological changes of the frozen ground, as it mainly depends on the moisture content within the active layer. But, as shown in Figs. 3.4–3.8, it is challenging to obtain seasonal subsidence in most years at the study sites, due to the irregularity and inconsistency of surface elevation changes.

We alternatively use the end-of-thaw-season elevations to investigate frozen ground dynamics. The end-of-thaw elevation was derived as the mean value of the surface positions at the last seven days in a thawing season, since the thawing front moves slowly at the end of season and the further surface deformation is limited. Based on the Stefan equation, we compared the end-of-thaw elevations to the square-root-of thaw indices. In this section, we focus on the results in Resolute Bay, as they are the longest time series.

In Fig. 3.16(a), the end-of-thaw-season elevations and \sqrt{DDT} were highly negatively correlated between 2003 and 2012, whereas they were low in 2013 and 2014 with cool summers. To further investigate their correlation, we built a scatter plot of end-of-thaw-season elevations versus \sqrt{DDT} (Fig. 3.16(b)), but found that the linear line fitted poorly. After removing the measurements in 2013 and 2014, the R^2 and root mean square error (RMSE) of the best linear fit improves significantly, from 0.24 to 0.83 and 2.57 cm to 1.19 cm, respectively (Fig. 3.16(c)).

We postulated that the highly negative correlation during 2003–2012 was due to active layer thickening. A larger DDT indicates that more heat can penetrate into the deeper frozen ground, leading to thicker active layer, more ice melting, thus larger subsidence and lower surface elevation. This postulation of thickening active layer during 2003–2012 is consistent with the borehole ground temperatures during 2008–2012 (Fig. 3.17). The ground temperatures show that the thawing front (i.e., the 0 °C isotherm) deepened and exceeded 1 m depth in 2011.

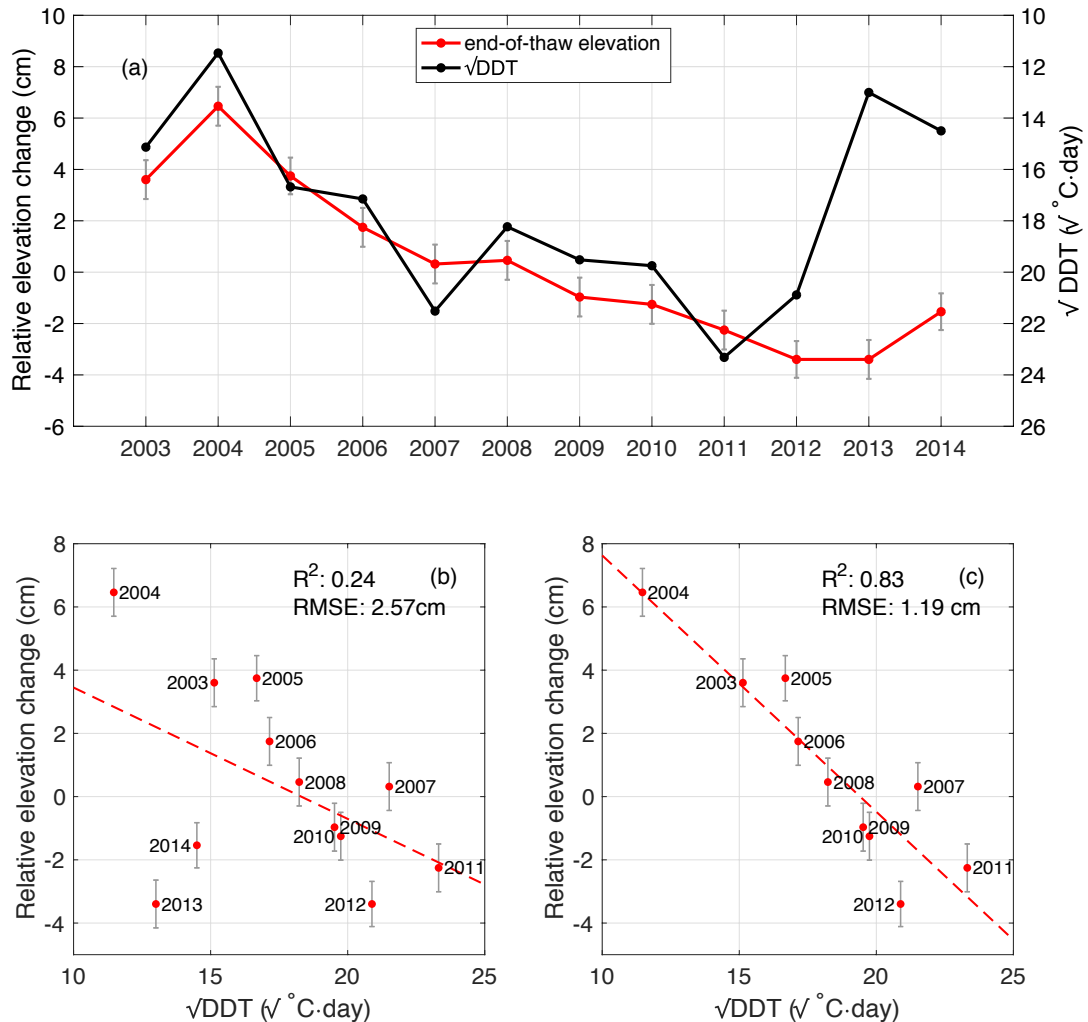


Figure 3.16: (a) Time series of end-of-thaw elevations and square-root-of thawing indices during 2003–2014 in Resolute Bay. (b) Scatter plot between end-of-thaw elevations and \sqrt{DDT} during 2003–2014. (c) Similar plot to (b) but for measurements during 2003–2012. The correlation coefficient and root mean square error (RMSE) are presented as well.

However, in 2013 and 2014, the end-of-thaw elevations were low, even in the relatively cool summers (corresponding to low DDT). This was possibly due to the changes in soil properties of the active layer and ground ice at the permafrost table, induced by the extremely warm summer in 2011, whose DDT was 542.9 $^{\circ}\text{C}\cdot\text{day}$, more than four times larger than that in 2004 with 132.3 $^{\circ}\text{C}\cdot\text{day}$. After 2011, the response of

the active layer to air temperatures may change. Therefore, even with low DDT, the maximal thaw depths were still larger than expected, resulting in low end-of-thaw-season surface elevations. Yet, ancillary data such as thermal properties, ice content, soil moisture, and active layer thickness are needed to test these postulated changes.

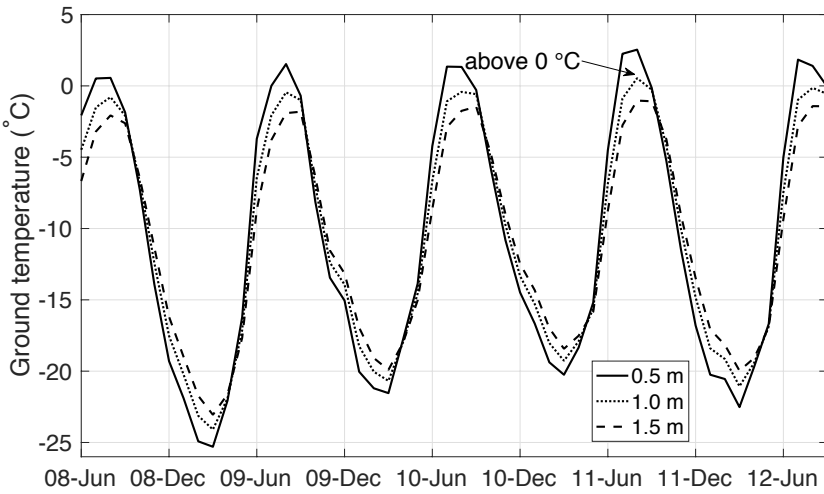


Figure 3.17: Ground temperatures at the depths of 0.5 m, 1.0 m, and 1.5 m between June 2008 and June 2012 in Resolute Bay. We mark that the ground temperature at 1.0 m depth was warmer than 0°C in 2011.

3.5 Conclusion

The ground surface underwent multi-year linear subsidence by $0.61 \pm 0.04 \text{ cm}\cdot\text{yr}^{-1}$ during 2012–2018 in Alert, $0.70 \pm 0.02 \text{ cm}\cdot\text{yr}^{-1}$ during 2003–2014 in Resolute Bay, $0.17 \pm 0.02 \text{ cm}\cdot\text{yr}^{-1}$ during 2010–2020 in Baker Lake, and $0.10 \pm 0.02 \text{ cm}\cdot\text{yr}^{-1}$ during 2010–2020 in Iqaluit. Repulse Bay had an insignificant uplift trend of $0.01 \pm 0.04 \text{ cm}\cdot\text{yr}^{-1}$ during 2014–2020. The trends at Alert, Resolute Bay, and Baker Lake are negatively correlated with those of annual thaw indices, i.e., warming thaw seasons lead to surface subsidence. It indicates that air temperature might be the dominant driver for the permafrost degradation in the Canadian Arctic.

We also observed that the seasonal surface elevation changes were irregular and inconsistent at most Canadian Arctic sites. The Stefan equation cannot fully explain the temporal evolution of vertical surface movement in most years at each site, by showing weakly negative or positive correlations between surface elevation changes and square-root-of thawing indices. The average seasonal surface elevation changes over the data time span generally show typical subsidence trends in Alert and Baker Lake. Their correlation coefficients with the average normalized square-root-of thawing indices are -0.65 and -0.64, respectively. Whereas, the average seasonal observations in Resolute Bay and Repulse Bay show significant summer heave. Their correlations with the average normalized square-root-of thawing indices are very weak. The frozen ground conditions in Alert and Baker Lake are closer to the assumed scenario of the Stefan equation.

In Resolute Bay, we found a highly negative correlation between the end-of-thaw elevations and the square-root-of thaw indices during 2003–2012 and postulated that it was possibly due to active layer thickening under the warming thawing seasons. The cause for the low end-of-thaw elevations in 2013 and 2014 with cool summers was possibly the changes in soil properties and ground ice content near the permafrost table triggered by the extremely warm summer in 2011. This hypothesis requires ground temperature, soil moisture, and ground ice content to validate.

End of chapter.

Chapter 4

A moist-to-dry shift of active layer during 2004–2018 in Utqiagvik, Alaska revealed by GNSS-IR-estimated seasonal subsidence

4.1 Introduction

The ground surface in a permafrost area is subject to uplift/subsidence seasonally, due to the active layer freezing/thawing. The magnitude of the seasonal subsidence dominantly depends on the soil moisture content within the active layer. A sensitivity test of active layer thickness to the climatic and environmental variables, such as air temperature, vegetation, and soil texture, has been conducted by Wang et al. (2020) using a process-based Kudryavtsev permafrost model. The air temperature and soil moisture content were found to be the most dominant factors determining the active layer

thickness. Therefore, the seasonal subsidence is closely linked with the thermal and hydrological conditions of the active layer. In section 1.2.2, we have elaborated that D , the ratio between surface elevation changes and square-root-of thawing indices, is generally a function of soil moisture content. Conceptually, the ratio of seasonal subsidence versus square-root-of annual thawing index has the potential to reveal the hydrological state of the active layer as a bulk.

Surface elevation changes have been measured by either the traditional leveling surveys or the modern geodetic and remote sensing techniques, such as GNSS positioning, InSAR, and LiDAR (see the details in Chapter 1). These approaches usually provide temporally coarse observations. For instance, the temporal intervals of the InSAR measurements range from 6 days to longer than a month. Such observations make it challenging to reliably determine seasonal subsidence. The simplified Stefan equation 1.4 has been frequently used to fit surface elevation changes to estimate seasonal subsidence (Liu et al., 2010, 2012, 2014a,b, 2015). However, considering the limited samples, the parameter D in the simplified Stefan equation was fixed to be a constant over the data time span. This implies an assumption of invariant moisture condition of the active layer. Moreover, the estimated seasonal subsidence might be biased, as the observations are so coarse that some processes might be overlooked (Liu et al., 2015).

The GNSS-IR can provide continuous and daily measurements of surface elevation changes, which give an opportunity to reliably estimate seasonal subsidence. Liu and Larson (2018) obtained the GNSS-IR observations during 2004–2015 in Utqiagvik, Alaska. They also used the simplified Stefan model to determine the seasonal subsidence. Similarly, Hu et al. (2018) used their proposed cyclic model, considering not only surface subsidence but also uplift, to fit the GNSS-IR measurements to estimate seasonal subsidence in Utqiagvik, Alaska as well. Since the GNSS-IR measurements are in daily intervals, we can directly use the observations at the beginning and end

of a thaw season to calculate the seasonal subsidence. In this manner, the estimated seasonal subsidence is not affected by the parameter determination of the simplified Stefan model. Liu and Larson (2018) and Hu et al. (2018) estimated D year by year. However, they did not recognize the indication of D for the hydrological state in the active layer.

In our study, we use the GNSS-IR-estimated seasonal subsidence to estimate D annually and explore its feasibility in inferring soil moisture changes of the active layer as a bulk. Our objectives of this study are (1) to derive the seasonal subsidence during 2004–2020 at Utqiagvik, Alaska by directly using the GNSS-IR measurements at the beginning and end of thaw seasons and (2) to use the estimated seasonal subsidence to reveal the hydrological changes in the active layer at Utqiagvik, Alaska.

This study provides a fresh perspective on the usage of surface elevation changes in permafrost studies. Surface elevation changes have been used to infer soil moisture migration from the thawed soil downward to the frozen ground (Mackay, 1983), quantify the magnitude of seasonal subsidence and multi-year linear trend of surface settlement in various permafrost landscapes (Liu et al., 2010, 2012, 2014a,b, 2015; Liu and Larson, 2018; Zhang et al., 2020), characterize the seasonal uplift in a freezing season with late snow (Hu et al., 2018), inverse active layer thickness (Liu et al., 2012; Schuur et al., 2015), correct active layer thickness in ice-rich permafrost regions (Shiklomanov et al., 2013; Streletskiy et al., 2017), and estimate ground ice loss (Daout et al., 2020). For the first time, our study uses the interannual variability of the seasonal subsidence to infer the hydrological changes of the active layer. The networks of soil moisture sensors distribute sparsely and unevenly, especially in the extensive permafrost regions. The remote sensing observations typically refer to the soil moisture content of the near-surface soil (e.g., the 0–5 cm layer for the Soil Moisture Active Passive products (Entekhabi et al., 2010) and GNSS-IR estimates (Larson, 2016)), which cannot fully characterize the soil moisture conditions in the active layer. Using

seasonal subsidence at least can reveal the shift of the hydrological state (moist to dry or dry to moist) of the active layer. Moreover, our study points out that the contribution of soil moisture variation to the surface elevation changes should be assessed when using them to study permafrost degradation and aggradation (e.g., [Zhang et al. \(2020\)](#)).

In section [4.2](#), we briefly describe the study site. Section [4.3](#) shows the derivation of seasonal subsidence by GNSS-IR and the ratio of seasonal subsidence and square-root-of thawing index. In section [4.4](#), we present the results of seasonal subsidence during 2004–2020 and their relationship with thawing indices. In section [4.5](#), we interpret the results by proposing and validating our hypothesis and discussing the physical mechanism behind our findings. We also discuss the limitation in using long-term surface deformation to study permafrost degradation and aggradation. We conclude this study in section [4.6](#).

4.2 Study site

The study site, Utqiagvik, Alaska, is located in the North Slope of Alaska ([Fig. 4.1\(a\)](#)). It has an Arctic maritime climate with cool and moist summer. The mean annual air temperature is around -9.7 °C. The precipitation is limited and around 60% deposits as rainfall in summer. This site is underlain by continuous permafrost with a thickness up to 400 m ([Brewer, 1958](#)). The active layer thickness is landscape specific, varying from 29 to 83 cm with an average of 36 cm ([Shiklomanov et al., 2010](#)). The near-surface permafrost is ice-rich, with an ice content of up to 75% in the top 2 m ([Brown and Sellmann, 1973](#)). The biome of this site is the graminoid-moss tundra. As for the soil profile, the near-surface layer is peat varying from 5 cm to 20 cm in thickness, which is underlain by silty soil ([Shiklomanov et al., 2010](#)).

The PBO GNSS station, SG27, has been continuously operating since 2002. Its

surrounding area is open and relatively smooth and horizontal (Fig. 4.1(b), (d)), which makes SG27 to be useful to measure surface elevation changes by GNSS-IR. SG27 has a wooden monument, which is ~ 3.8 m high above the ground surface and ~ 5 m deep into the ground. Such a deep foundation makes SG27 stable with respect to the solid earth. The receiver and antenna are SEPT POLARX5 and TRM59800.80 SCIS, respectively.

A soil climate station, U1-1, a component of the CALM site U1, exists close to SG27 (Fig. 4.1(c)). U1-1 measures ground temperature and soil moisture content at 5 cm, 20 cm, and 35 cm depths.

4.3 Methodology

4.3.1 Seasonal subsidence estimated by GNSS-IR

The seasonal subsidence s can be derived as the difference between the reflector heights at the beginning and end of a thaw season, which is expressed by

$$s = H_{eot} - H_{bot}, \quad (4.1)$$

where eot and bot denote the end and beginning of thawing, respectively. As the uncertainties of the daily reflector heights are on the order of several centimeters (Table 2.2), directly using the reflector heights on the first and last days of a thaw season may introduce a bias into the seasonal subsidence. Therefore, we use the mean value of the reflector heights on the first and last seven days of a thaw season.

We use the ground temperatures at the 5 cm depth and the reflector heights in the transitional period (freeze-to-thaw or thaw-to-freeze) to determine the duration of a thaw season. The near-surface ground temperature has to be above 1 °C and the ground should not be covered by snow in a thaw season. The threshold of 1 °C

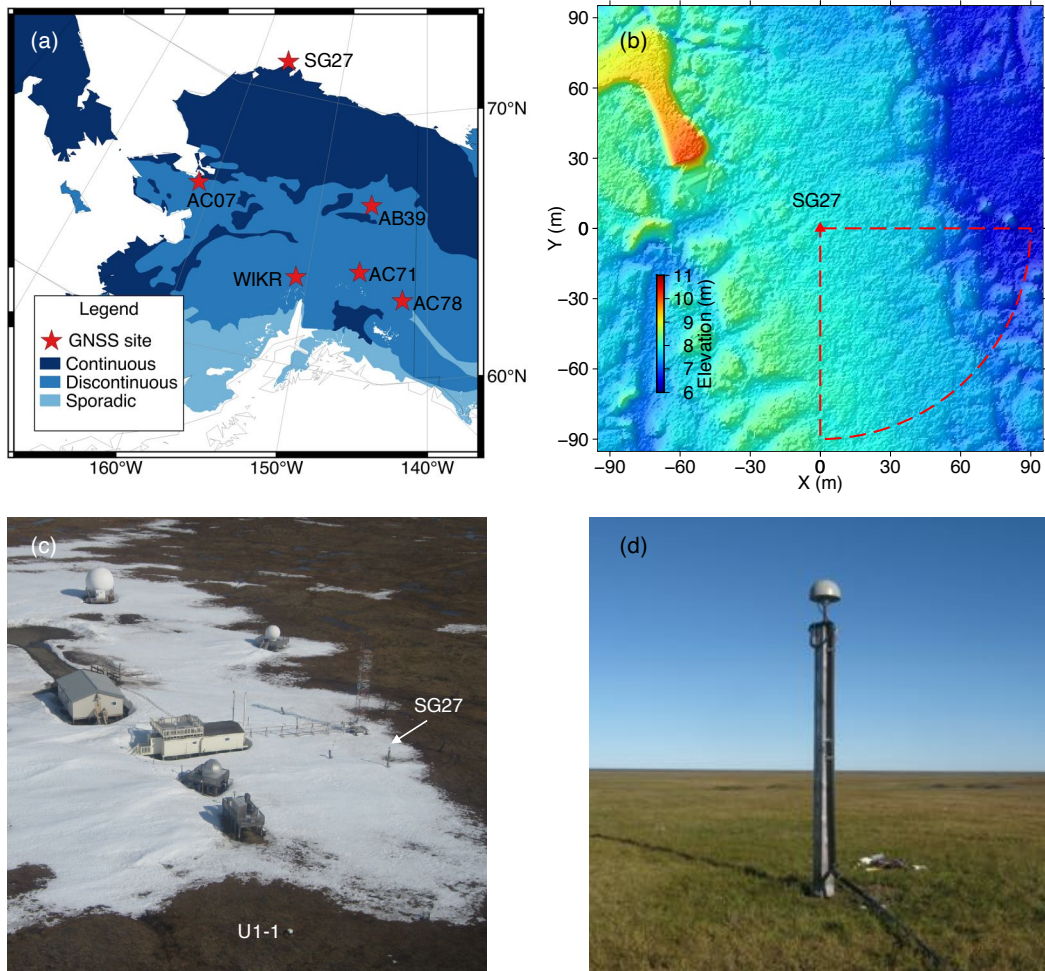


Figure 4.1: (a) The geological location of SG27 in Alaska. Permafrost zonation categories are indicated by variously shaded colors of blue (Brown et al., 1997). (b) A digital elevation map at the site of SG27. The dashed-outlined fan delineates the coverage of the GNSS-IR measurements. (c) A photo shows the locations of SG27 and U1-1. (d) A ground photo of SG27. This figure is modified from Liu and Larson (2018).

is chose empirically (Chew et al., 2017). We use the variations of reflector heights to infer the existence of snow cover, as the snow ablation (accumulation) causes an abrupt increase (decrease) in reflector heights.

4.3.2 The ratio between seasonal subsidence and square-root-of thawing index

The Stefan equation for surface deformation has been introduced in section 1.2.2. In this equation, surface elevation changes are proportional to the square-root-of thawing indices with a ratio D . This parameter D is generally a function of soil moisture content, which can be used to infer the hydrological changes in the active layer (see the details in section 1.2.2).

In a thaw season spanning from τ_{bot} to τ_{eot} , based on equation 1.3 and 1.5, we can derive the seasonal subsidence s as

$$s = d(\tau_{eot}) - d(\tau_{bot}) = D(\sqrt{DDT(\tau_{eot})} - \sqrt{DDT(\tau_{bot})}). \quad (4.2)$$

The ratio D can be estimated annually by the GNSS-IR-measured seasonal subsidence and the difference in the square-root-of thawing indices between τ_{bot} and τ_{eot} (hereafter called square-root-of thawing index for simplicity).

4.4 Results

We obtained the GNSS-IR-measured seasonal subsidence in each year during 2004–2020, which are presented in Fig. 4.2(a). We also present the time series of \sqrt{DDT} in the same period. Their scatter plot and the best linear fit are shown in Fig. 4.2(b).

The seasonal subsidence's magnitude underwent a decrease from 2004 to 2006, then increased sharply in 2007 and generally dropped in the following years till 2014. Subsequently, it rose again significantly in 2015 and descended till 2018. Then, the magnitude increased in 2019 and decreased in the following year. The correlation coefficient between the seasonal subsidence and \sqrt{DDT} over the entire time span is as moderate as 0.43. Moreover, in Fig. 4.2(b), the dots above the fit line indicate that

the seasonal subsidence is more sensitive to the thawing indices than those below the fit line. For example, thawing indices were similar in 2004 and 2010, however, the seasonal subsidence in 2004 was nearly twice of that in 2010.

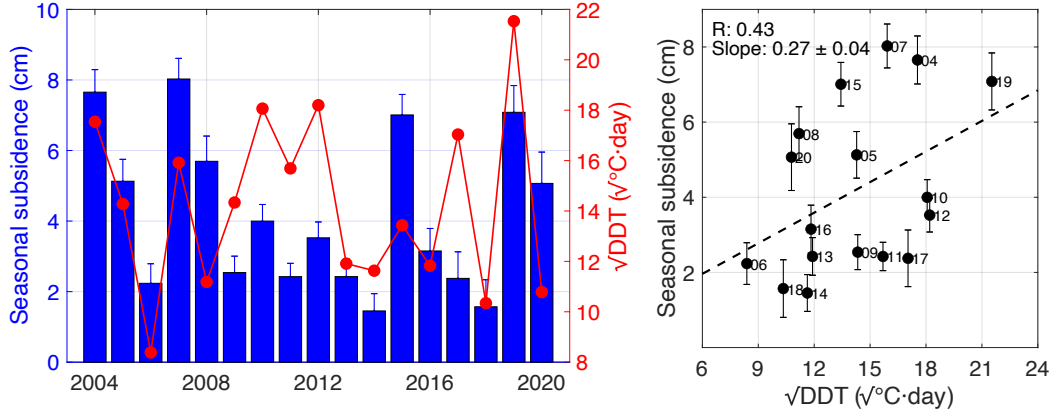


Figure 4.2: (a) Time series of seasonal subsidence and \sqrt{DDT} during 2004–2020. (b) Scatter plot of seasonal subsidence versus \sqrt{DDT} during 2004–2020. The correlation coefficient and slope of the linear regression line with the unit of $\text{cm}\cdot(\text{}^{\circ}\text{C}\cdot\text{day})^{-1/2}$ are presented.

Based on the distribution of the dots above/below the fit line in Fig. 4.2(b), we subdivided the time series of seasonal subsidence into three groups, i.e., during 2004–2008, 2009–2018, and 2019–2020. We then studied the correlation between the seasonal subsidence and \sqrt{DDT} in each group (Fig. 4.3). During 2004–2008, the seasonal subsidence and thawing indices had a correlation coefficient of 0.9, and the slope of the regression line was $0.43 \pm 0.04 \text{ cm}\cdot(\text{}^{\circ}\text{C}\cdot\text{day})^{1/2}$ (Fig. 4.3(a)). We hereafter use the slope to represent the statistically estimated ratio between seasonal subsidence and \sqrt{DDT} . By excluding the measurement in 2015 identified as an outlier, the seasonal subsidence and \sqrt{DDT} during 2009–2018 had a correlation coefficient of 0.7 and a slope of the regression line of $0.18 \pm 0.01 \text{ cm}\cdot(\text{}^{\circ}\text{C}\cdot\text{day})^{1/2}$ (Fig. 4.3(b)). The seasonal subsidence in 2015 deviated significantly from the regression line by showing an error larger than twice of the root mean square error. For the seasonal subsidence in 2019 and 2020, their regression line had a slope of $0.36 \pm 0.06 \text{ cm}\cdot(\text{}^{\circ}\text{C}\cdot\text{day})^{1/2}$ (Fig.

4.3(c)). We focus on the slopes during 2004–2008 and 2009–2018, as the slope during 2019–2020 might be biased due to limited samples. The slope during 2004–2008 was steeper than that of 2009–2018, which indicates that surface subsidence was more sensitive to air temperature during 2004–2008.

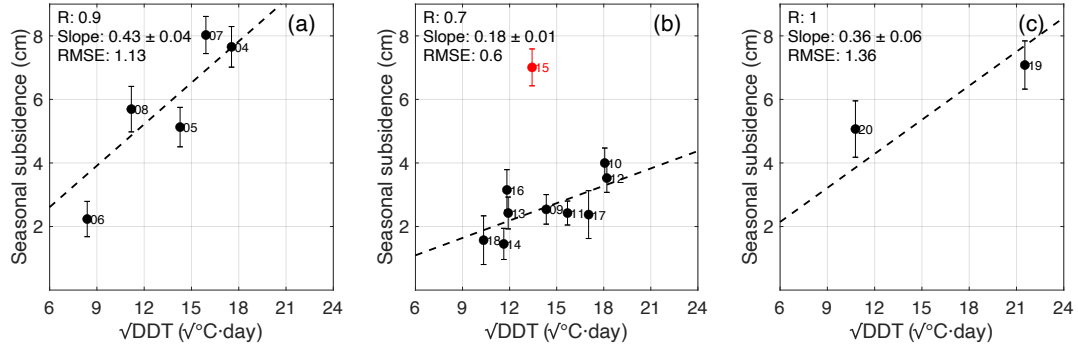


Figure 4.3: Scatter plots between seasonal subsidence and \sqrt{DDT} during (a) 2004–2008, (b) 2009–2018, (c) 2019–2020, respectively. The measurement in 2015, marked as a red dot, is excluded as an outlier. The correlation coefficient (R), slope of the linear regression line, and root mean square error (RMSE) are presented as well.

4.5 Discussion

4.5.1 A moist-to-dry shift of the active layer from 2004–2008 to 2009–2018

We hypothesized that the slope decreased from 2004–2008 to 2009–2018 was caused by the moisture decrease in the active layer. Based on section 1.2.2, the ratio D positively varies with soil moisture content of the active layer. Lower D means less moisture content in the active layer. Therefore, we postulated that a moist-to-dry shift of the active layer occurred from 2004–2008 to 2009–2018 and the relatively dry active layer caused the smaller slope during 2009–2018.

We used the in situ measurements of soil moisture at the depths of 5 cm, 20 cm,

and 35 cm during 2004–2016 to verify our hypothesis, which are presented in Fig. 4.4. We obtained the mean values and standard deviations of the moisture contents in each thaw season at each depth. The best linear fits of these mean values were also constructed. For soil moisture at the 5 cm depth, it decreased obviously from $0.32 \text{ cm}^3 \cdot \text{cm}^{-3}$ in 2004 to $0.18 \text{ cm}^3 \cdot \text{cm}^{-3}$ in 2008 by the rate of $0.05 \pm 0.02 \text{ cm}^3 \cdot \text{cm}^{-3} \cdot \text{yr}^{-1}$, then increased slightly by $0.01 \pm 0.01 \text{ cm}^3 \cdot \text{cm}^{-3} \cdot \text{yr}^{-1}$ during 2009–2016 (Fig. 4.4(a)). As for the soil moisture at the 20 cm depth, it decreased by the rate of $0.02 \pm 0.02 \text{ cm}^3 \cdot \text{cm}^{-3} \cdot \text{yr}^{-1}$ during 2004–2008, and then kept relatively steady during 2009–2016 (Fig. 4.4(b)). The soil moisture at 35 cm depth was generally stable during the data time span except for a decrease in 2007 (Fig. 4.4(c)). The soil down to 35 cm depth in the active layer underwent a drying process during 2004–2008 then kept the dry condition during 2009–2016. The in situ measurements support the postulated moist-to-dry shift of the active layer.

In general, the soil thermal conductivity varies positively with moisture content. When the soil dries, the soil pores increase and filled by air, which is relatively inefficient for heat conduction compared with moisture and soil particles. For example, the thermal conductivity for dry silt is $0.2 \text{ W} \cdot \text{m}^{-1} \cdot {}^\circ\text{C}^{-1}$ whereas $0.96 \text{ W} \cdot \text{m}^{-1} \cdot {}^\circ\text{C}^{-1}$ when it becomes saturated (Lu et al., 2007). At the study site, the relatively dry top soil in the 0–35 cm layer during 2009–2016 acted as an insulator retarding the heat transfer from the atmosphere into the deeper frozen ground and affected its thermal regime.

In situ ground temperatures at the depths of 5 cm, 20 cm, and 35 cm are used to reveal the changes of heat transfer efficiency due to the dry top layer. We calculated the ratio between the DDT derived by ground temperatures ($\text{DDT}_{\text{ground}}$) and that by air temperatures (DDT_{air}) at these three depths (Fig. 4.5). A smaller ratio indicates less efficiency of heat transfer. The ratios during 2004–2008 were generally larger than those during 2009–2016 at all of the three depths. For instance, at 5 cm depth,

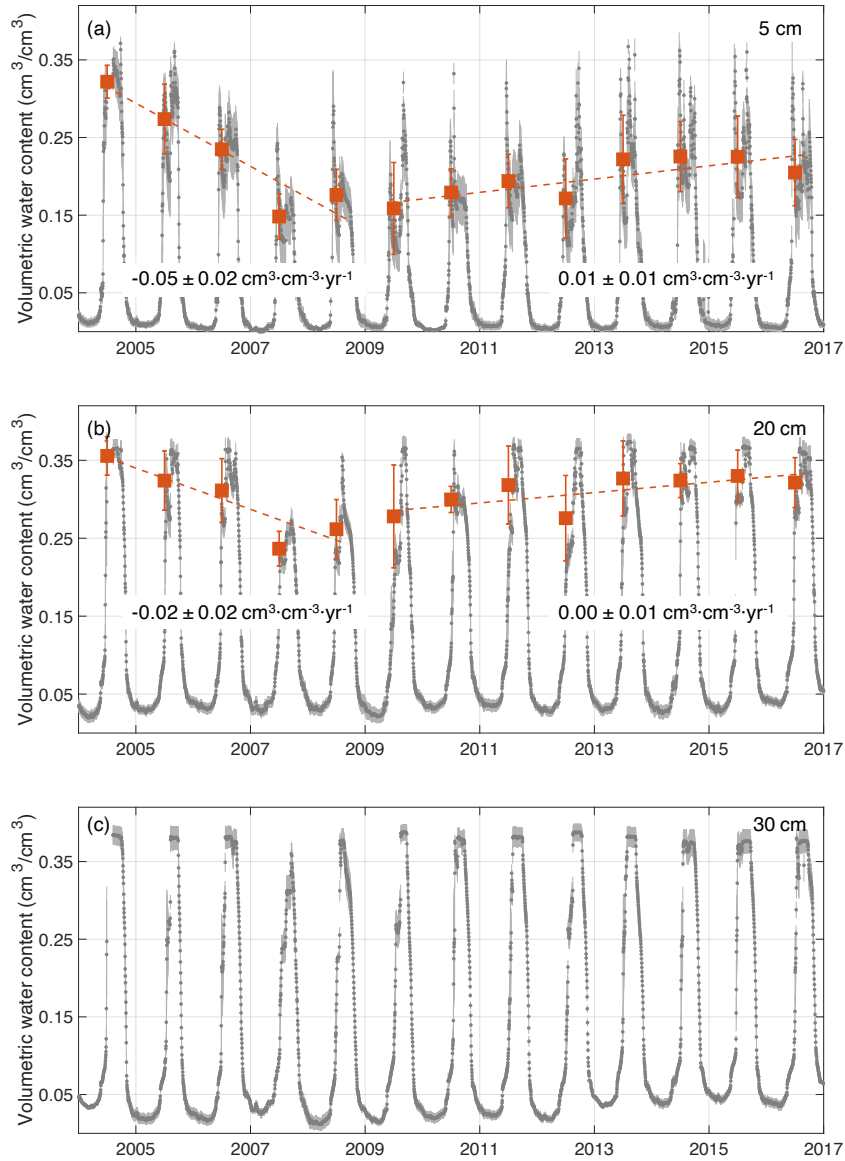


Figure 4.4: (a) In situ volumetric water content at 5 cm during 2004–2016. The brown solid squares and error bars represent the mean values and standard deviations of soil moisture content in each thawing season. The best linear fits of the mean values during 2004–2008 and 2009–2016 have the slopes of $-0.05 \pm 0.02 \text{ cm}^3 \cdot \text{cm}^{-3} \cdot \text{yr}^{-1}$ and $0.01 \pm 0.01 \text{ cm}^3 \cdot \text{cm}^{-3} \cdot \text{yr}^{-1}$, respectively. (b) and (c) are for in situ soil moisture content at 20 cm and 35 cm, respectively. We do not calculate the mean values of soil moisture content at 35 cm depth, as they are nearly constant during 2004–2016.

the mean value of the ratios during 2004–2008 was 0.86 with the standard deviation of 0.09, whereas the one during 2009–2016 was 0.66 ± 0.07 . The results of the other depths are presented in Table 4.1. A similar phenomenon was reported by Göckede et al. (2019), which found that the dry top layer at a persistent drainage site had a cooling effect on the frozen ground and led to a shallower active layer, compared with the nearby wetland as the control site.

To sum up, due to the persistent decrease of soil moisture down to the 35 cm depth during 2004–2008, the soil shifted from being moist to relatively dry during 2009–2018. The dry top soil and induced changes in soil thermal properties led to a shallower active layer (than the expected in a similar condition to that during 2004–2008). Consequently, due to the decreased moisture content and shallower active layer, the ground surface underwent less seasonal subsidence therefore a smaller slope during 2009–2018. The soil moisture content in 2007 and 2008 reached the level comparable to that during 2009–2018, which seems to be inconsistent with the moist state indicated by the higher slope during 2004–2008. We speculated that the active layer was still in the transition and did not enter the next state completely in 2007 and 2008. It responded to the air temperatures in a similar manner to that during 2004–2006.

4.5.2 Limitations of surface elevation changes in revealing permafrost degradation/aggradation

The multi-year surface elevation changes have been used to infer permafrost changes, such as those presented in Chapter 3 (Liu and Larson, 2018; Zhang et al., 2020). The multi-year trend of surface deformation could be contributed by the near-surface permafrost degradation/aggradation and soil moisture changes within the active layer. The impact of moisture changes has to be assessed and quantified. Otherwise, the permafrost changes would be under or over-estimated. At the current stage, it is challenging to quantify the contribution of soil moisture changes within the active layer,

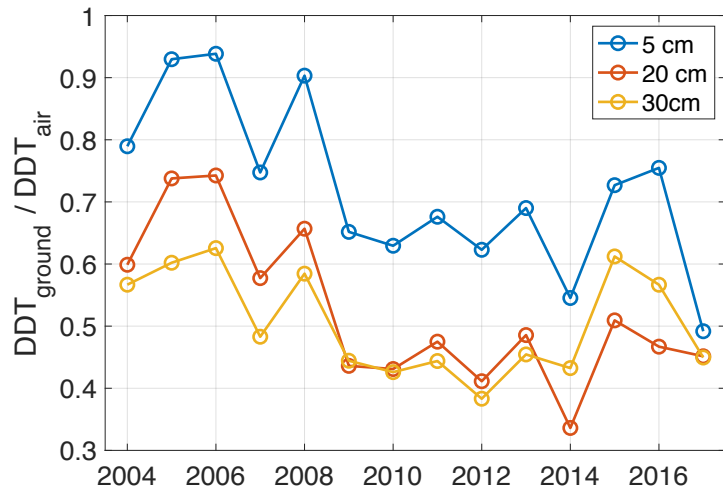


Figure 4.5: The ratios of DDT derived from ground temperature (DDT_{ground}) to that from air temperature (DDT_{air}) during 2004–2016 at the depths of 5, 20, and 35 cm, respectively.

Table 4.1: Ratios of DDT derived from the ground temperatures (DDT_{ground}) and that from air temperatures (DDT_{air}) in each year during 2004–2016 at 5 cm, 20 cm, and 35 cm depth, respectively.

Year	DDT _{ground} /DDT _{air}			Mean ± std		
	5 cm	20 cm	35 cm	5 cm	20 cm	35 cm
2004	0.79	0.60	0.57			
2005	0.93	0.74	0.60			
2006	0.94	0.74	0.63	0.86 ± 0.09	0.66 ± 0.08	0.57 ± 0.05
2007	0.75	0.58	0.48			
2008	0.90	0.66	0.58			
2009	0.65	0.44	0.44			
2010	0.63	0.43	0.43			
2011	0.68	0.48	0.44			
2012	0.62	0.41	0.38	0.66 ± 0.07	0.44 ± 0.05	0.47 ± 0.08
2013	0.69	0.49	0.45			
2014	0.55	0.34	0.43			
2015	0.73	0.51	0.61			
2016	0.75	0.47	0.57			

as the measurements of soil moisture content, active layer thickness, and ground temperature are usually poorly sampled or even absent.

In Chapter 3, we found that the ground surface in Alert, Resolute Bay, and Baker Lake underwent a multi-year linear trend of subsidence. At these sites, the records of soil moisture content and active layer thickness are not available. Therefore, we cannot evaluate the changes in soil moisture and quantify their contributions. As the thawing seasons at these sites were warming, we postulated that the subsidence was possibly caused by near-surface permafrost thawing. Iqaluit had a multi-year subsidence trend in cooling summers. Soil moisture content and other environmental variables may moderate the impact of air temperature and lead to ground settlement.

4.6 Conclusion

Seasonal subsidence is a useful indicator of heat and moisture changes within the active layer. Contrarily with active layer thickness, it positively varies with soil moisture content. We obtained the seasonal subsidence during 2004–2020 at SG27 in Utqiagvik, Alaska by GNSS-IR. We found that the ratio between seasonal subsidence and \sqrt{DDT} during 2004–2008 was $0.43 \pm 0.04 \text{ cm} \cdot (\text{ }^{\circ}\text{C} \cdot \text{day})^{-1/2}$. Whereas, it was $0.18 \pm 0.01 \text{ cm} \cdot (\text{ }^{\circ}\text{C} \cdot \text{day})^{-1/2}$ during 2009–2018.

The significant ratio drop could be caused by the moist-to-dry shift of the active layer. Based on in situ measurements of soil moisture, the soil down to 35 cm depth persistently decreased during 2004–2008 then kept the relatively dry state during 2009–2016. The dry top soil leads to low thermal conductivity, impedes the heat transfer from air to the deeper frozen ground, and consequently leads to a shallow active layer. Dry soil and less active layer thickness resulted in less seasonal subsidence and a smaller ratio during 2009–2018.

This study highlights using the seasonal subsidence to reveal the moist-to-dry

shift of the active layer. It provides a new perspective into the usage of surface deformation to study frozen ground dynamics. Multiple GNSS sites have been identified to be suitable for GNSS-IR studies. Their continuous and daily measurements can be used to estimate seasonal subsidence, which can be used in turn to infer the hydrological changes in the active layer. This study also implies that soil moisture changes must be considered when using surface deformation to investigate permafrost degradation and aggradation.

End of chapter.

Chapter 5

Improving the GNSS-IR algorithm for estimating surface soil moisture in permafrost areas¹

5.1 Introduction

Surface soil moisture plays a significant role in regulating surface energy balance and water cycle through evapotranspiration (Seneviratne et al., 2010). It affects the exchange of water and heat between the atmosphere and frozen ground, consequently influences the thermal and hydrological conditions in permafrost areas. Thus, continuously monitoring the soil moisture is crucial for understanding its impact on the active layer and near-surface permafrost.

Soil moisture monitoring networks (e.g., <http://www.okmesonet.ocs.ou.edu>) exist but are usually distributed sparsely and unevenly, which cannot fully repre-

¹This chapter is based on Jiahua Zhang, Lin Liu, Lei Su, and Tao Che (2021). Three-in-one: GPS-IR measurements of ground surface elevation changes, soil moisture, and snow depth at a permafrost site in the northeastern Qinghai-Tibet Plateau. *The Cryosphere*, 15, 3021–3033, <https://doi.org/10.5194/tc-15-3021-2021>.

sent the soil moisture conditions, especially in the extensive permafrost regions in QTP and Arctic. The remote sensing observations, such as Soil Moisture Active Passive (SMAP), have much broader spatial coverages on the order of tens of kilometers. Moreover, they are only validated at several sites (Chen et al., 2013, 2017; Ma et al., 2017; Zhang et al., 2017a).

The ability of GNSS-IR in estimating soil moisture content has been well investigated (Larson et al., 2008b, 2010; Zavorotny et al., 2010; Chew et al., 2014, 2015; Small et al., 2010). It uses the oscillation phase of SNR observations, which is nearly proportional to the soil moisture content in the layer of 0–5 cm depth. The GNSS-IR measurements have the advantages of daily scales and local spatial coverages on the order of 1000 m². They can bridge the point in situ measurements and remote sensing ones. Small et al. (2010) estimated soil moisture at 11 sites with various vegetation conditions. The RMSEs of the GNSS-IR measurements range from 1.5% to 5.1%. This agreement level makes the GNSS-IR observations capable of validating the remote sensing ones.

The performance of the GNSS-IR algorithm for estimating soil moisture content has not been assessed in permafrost areas. The previous studies do not explicate the impact of seasonal surface elevation changes on soil moisture estimation. In the framework of GNSS-IR, the SNR phases are mostly determined by soil moisture and the GNSS-IR geometry. The surface elevation changes affect the GNSS-IR geometry, consequently, SNR phases and soil moisture estimates. We run simulations to elucidate that the commonly-used GNSS-IR algorithm cannot be applied directly to permafrost areas. Given this, our first objective in this study is to improve the default GNSS-IR algorithm to make it valid in permafrost areas. Furthermore, measuring surface elevation changes, soil moisture, and snow depth at a single site can fully utilize GNSS-IR in permafrost areas, which has not been conducted yet to date. Our next objective is to propose a three-in-one framework, i.e., integrating the GNSS-IR mea-

surements of surface elevation changes, soil moisture, and snow depth at one site. We use the SNR data recorded by QLBG in the northeastern QTP to validate the improved algorithm and illustrate the three-in-one framework.

In section 5.2, we briefly describe the study site and instrumentation. In section 5.3, we conduct simulations to illustrate the limitation of the default GNSS-IR algorithm for estimating soil moisture in permafrost areas, and introduce our solution for improvement. We then present the concept of the three-in-one framework. We finally summarize the datasets used in this study. Section 5.4 shows the results, i.e., the improvement of our method and the GNSS-IR estimates of surface elevation changes, soil moisture, and snow depth at QLBG. In section 5.5, we discuss the possible error sources of the modified method, surface reflectivity's impact on snow depth, and the benefits of the three-in-one framework for permafrost studies. We conclude this study by section 5.6.

5.2 Study site

The study site, Binggou (38.01° N, 100.24° E, 4120 m a.s.l.), is located in the northeastern QTP (Fig. 5.1(a)). The mean annual ground surface temperature is around -3.5°C . Permafrost exists at this site with a thickness of 25–30 m (Ran et al., 2018). The active layer thickness is ~ 1.6 m, based on ground temperature observations. The biome at this site is the alpine steppe. As for the soil texture profile, sandy silt dominates in the upper 0.2 m. The soil becomes a mixture of sand, silt, and gravel in the layer between 0.2 m and 0.5 m. The deeper layer is mainly composed of gravel. This general description of soil texture was recorded when installing the GNSS monument. The soil moisture content is $\sim 40\%$ in the upper 0.4 m, decreases to 20% at the depth of 0.8 m, and remains relatively constant to the depth of 1.6 m (Che et al., 2019).

A GNSS station, called QLBG, has been operating since November 2016. The an-

tenna height is ~ 2 m above the ground surface, and the monument foundation is ~ 1.5 m deep. The foundation depth is slightly shallower than the active layer base, which implies that the monument might settle in late summer when the thawing front reaches the permafrost table (or heave up at the beginning of freezing season when the foundation freezes). However, the magnitude of such movement is expected to be negligible, as the layer between the foundation depth and the active layer base is as thin as ~ 10 cm. Given that the soil moisture content is $\sim 20\%$, the thawing of this layer causes subsidence of only ~ 0.2 cm. Such a magnitude is at least one order less than the uncertainty of GNSS-IR measurements. Thus, the monument can be regarded as stable in the thawing season considered in this study (see the detailed discussion in section 5.5.1). The antenna of QLBG is mounted onto a galvanized steel pipe anchored to a concrete block. The GNSS receiver type is CHC N72, and the antenna is CHCC220GR with a CHCD radome. Figure 5.1(b) shows a ground photo of QLBG. In Fig. 5.1(c), an integrated weather station exists close to QLBG, which records various environmental variables, including soil moisture and ground temperature (Che et al., 2019). They are both measured to the depth of 1.6 m. Due to the open and relatively horizontal and smooth surface, QLBG is usable for GNSS-IR studies.

5.3 Improving the default algorithm of estimating soil moisture

5.3.1 Limitation of the default algorithm

The steps to retrieving phases from SNR data have been presented in section 1.3.3. Here, we make a brief description. For estimating the phase, an *a priori* reflector height H_0 has to be prescribed. Given any SNR interferogram, by fixing the reflector height to be H_0 , we can determine the phase by LSE. In the commonly-used algorithm,

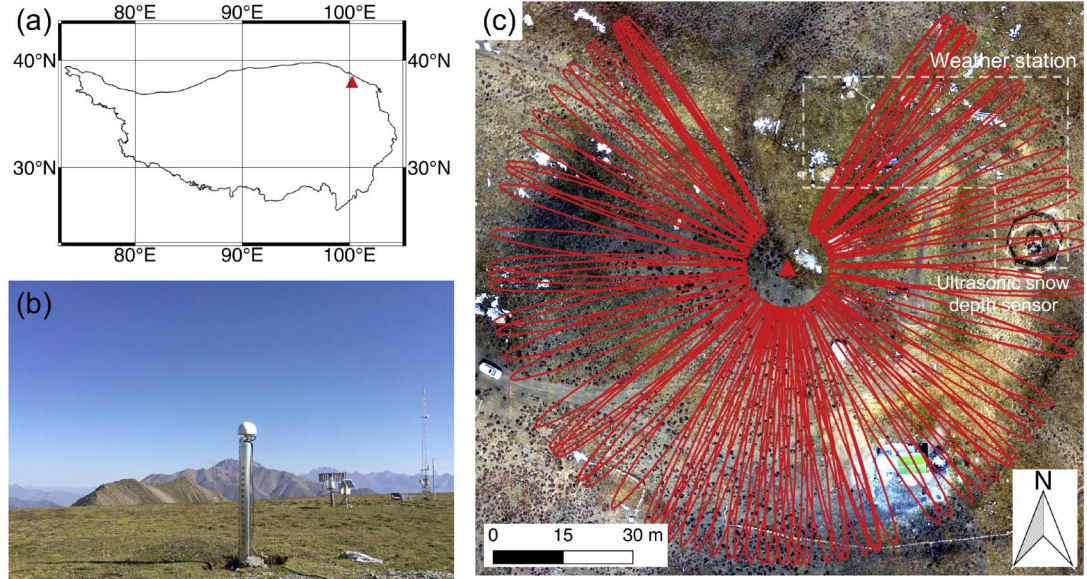


Figure 5.1: (a) Location of the study site, Binggou, in the northeastern Qinghai-Tibet Plateau. (b) Ground photo of the GNSS station QLBG. (c) Orthophoto of the Binggou site showing the surface condition, QLBG (red triangle), and the integrated weather station. Red elliptic curves indicate the footprints of the reflected L1 GPS signals at the satellite elevation angle of 5°.

H_0 is the mean value of the daily reflector heights over the data time span.

Using a constant reflector height H_0 to estimate phases might not be valid in permafrost areas, as the ground surface is subject to moves vertically due to the active layer thawing/freezing. To illustrate this problem and its impact on the phase estimation, we ran simulations by using the multipath simulator of [Nievinski and Larson \(2014\)](#). We initially set the reflector height H to be 2 m, which is the typical monument height of the most GNSS stations. Then, we introduced a surface deformation d . Positive (negative) means surface subsidence (uplift). In the simulations, d varies from -5 to 5 cm at a step of 1 cm. Not knowing the antenna gain pattern of CHCC220GR CHCD, we alternatively used the one of TRM29659.00 SCIT. Other key parameters used in the simulations are listed in Table 5.1.

In Fig 5.2(a), we show an example of the simulated SNR data with d of 2 cm whose

Table 5.1: Key parameters for SNR simulations with surface elevation changes.

Parameter	Value
GNSS signal	GPS L1 C/A
Antenna	TRM29659.00 with the radome SCIT
Reflector height	1.95–2.05 m with 1 cm intervals
Elevation angle	5–20°
Azimuth angle	0–360°
Soil type	Sandy loam

3-order polynomial fit has been removed. We used LSE to estimate the phase by using H and $H+d$, respectively. From the inset plot of Fig. 5.2(a), we can observe that using H introduces a phase bias of around -14°. Figure 5.2(b) shows the simulated bias corresponding to the various d . The bias is approximately proportional to the surface deformation.

In summer, surface subsidence accumulates with the downward movement of the thawing front, which leads to biases with larger magnitudes. The biases may mislead the interpretation of soil moisture variation, with a seasonal trend superimposed on the soil moisture estimates. Thus, such bias needs to be corrected when using GNSS-IR to estimate soil moisture content in permafrost areas. To solve this problem, we propose a solution presented in the following subsection.

5.3.2 Solution of introducing modeled surface elevation changes

To address the problem illustrated above, we proposed a solution of introducing modeled ground surface elevation changes. The modeled values are added to the constant H_0 to derive a time-varying reflector height H_0' , approximating the true daily changes of reflector height. For any given day, we use the corresponding reflector height to estimate phases. We have to note that the daily reflector heights derived by LSP cannot be used directly. As they have relatively large oscillations, the reflector heights cannot reflect the evolution of surface elevation changes in daily scales.

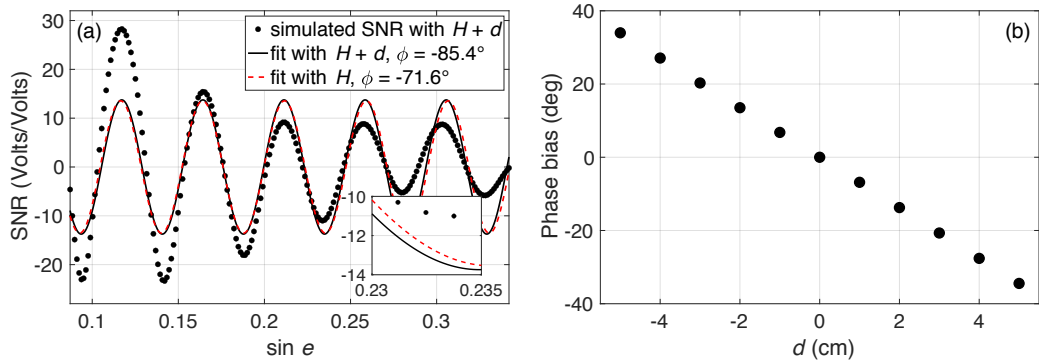


Figure 5.2: (a) Simulated SNR with $H+d$ and their fits based on $H+d$ and H , respectively. In this simulation, H and d are fixed as 2 m and 2 cm, respectively. The inset plot shows that the phases of these two fits are different. (b) The simulated phase bias when using various d .

We simulate the ground surface elevation changes based on the Stefan-equation-based model of Liu et al. (2010). This model can estimate surface deformation on any given day from the onset of thawing season. It is expressed as

$$d(\tau) = s\tilde{I}_T(\tau) + d_0, \quad (5.1)$$

where $d(\tau)$ is the surface deformation on the day of τ . s is the seasonal subsidence. $\tilde{I}_T(\tau)$ is the normalized square-root-of thermal index, $I_T(\tau)$, which can be derived by

$$I_T(\tau) = \sqrt{DDT(\tau)}. \quad (5.2)$$

We use the GNSS-IR-measured surface elevation changes and normalized thermal indices to inverse the parameters of s and d_0 . They are then used together with the normalized thermal indices to simulate ground surface elevation changes and then obtain H'_0 . We then use the H'_0 to estimate the phases. As in situ soil moisture observations are available, we directly compare them to the phases to obtain the mapping function.

5.3.3 Data

Snow depth was measured manually during DOY 112–156 in 2017. It was sampled at ten points on a daily basis, randomly distributed southeast of QLBG and near the ultrasonic snow depth sensor, which are generally within the azimuth range of 90–135 degrees (Fig. 5.1). We averaged them to obtain the daily measurements and used their standard deviations to be uncertainties. We use the manual observations to compare with our GNSS-IR measurements.

We also use in situ soil moisture and ground surface temperature in 2017 and 2018. We use the ground temperatures to determine the onset and duration of thaw seasons. They are also used to calculate the thermal index. We use the soil moisture observations to convert phases to soil moisture content, and then to validate our modified GNSS-IR method.

SNR data of the GPS L1 C/A code recorded by QLBG are available from November 2016 to April 2019 (Fig. 5.3). They have frequent and large gaps, such as during DOY 57–111 and DOY 191–215 in 2017 and DOY 77–180 in 2018, due to instrumentation problems. Considering the continuity of SNR data and availability of in situ measurements, we use the SNR data within the azimuth range of 90–135 degrees during 167–173 in 2017 to calculate the reflector height at the beginning of thawing season to be the reference for estimating snow depth, and the ones during DOY 112–156 to obtain snow depth. The SNR data within the azimuth range of 0–360 degrees during DOY 182–243 in 2018 are used to measure surface elevation changes and soil moisture content. The sampling rate of SNR data is 15 s. The SNR data are recorded as integers. L2C signals are not recorded.

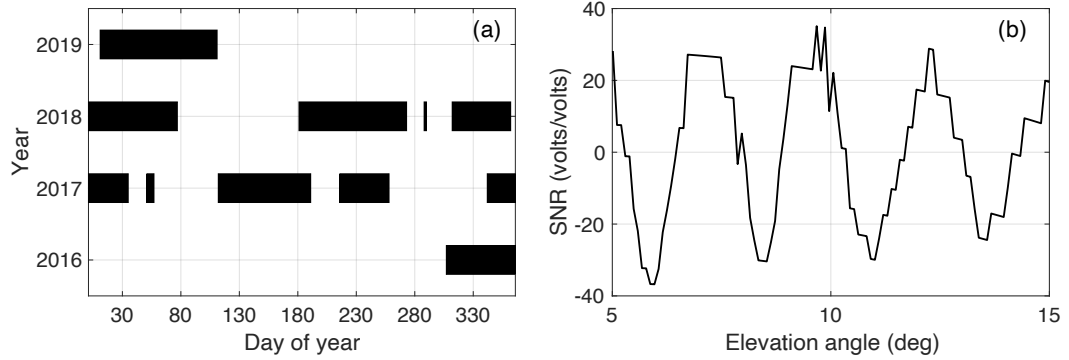


Figure 5.3: (a) Presence of SNR observations of the GPS L1 C/A code recorded by QLBG. (b) SNR observations with the elevation angles of 5–15 degrees of the GPS PRN02 satellite on DOY 220 in 2018. The second-order polynomial has been removed.

5.4 Results

5.4.1 Ground surface elevation changes

We obtained the daily reflector height measurements during DOY 182–243 in 2018. We then removed the mean value from the negative reflector heights and used the residuals to be the ground surface elevation changes, which are shown in Fig. 5.4(a). Their uncertainties are on the order of 1–2 centimeters. Surface elevation changes show a progressive subsidence trend, which is mainly caused by ground ice melting within the active layer.

We compared the surface elevation changes to the normalized thermal indices and built their best linear fit to obtain the model parameters based on section 5.3.2. The parameters s and d_0 are -1.7 ± 0.8 cm and 1.2 ± 0.6 cm, respectively (Fig. 5.4(b)). We then used these parameters and the normalized thermal indices to simulate the ground surface elevation changes, which are presented in Fig. 5.4(a) as a curve superimposed on the GNSS-IR measurements. The simulated surface deformation was used to compute the time-varying H_0' , to estimate the phases and then soil moisture content, which are presented in the following section.

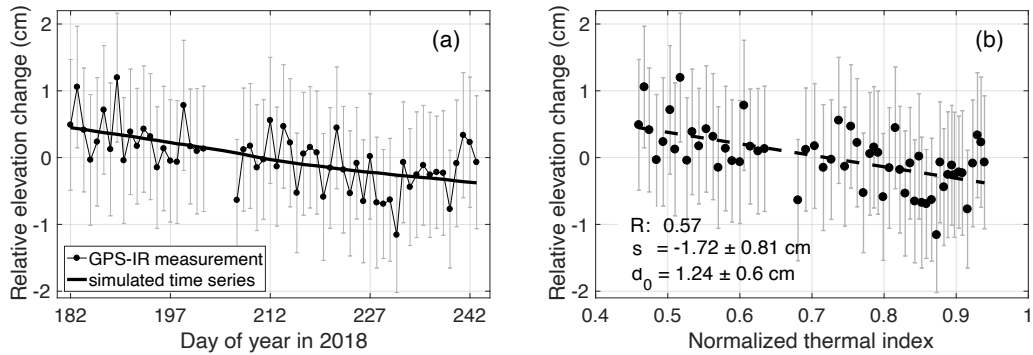


Figure 5.4: (a) Time series of GPS-IR measurements of ground surface elevation changes and the simulated ones based on the model parameters s and d_0 in (b) during DOY 182–243 in 2018. (b) Scatter plot between the ground surface elevation changes and the normalized thermal indices and their best linear fit as a dashed line. s and d_0 are the slope and intercept of this fit line.

5.4.2 Validation of the improved method and soil moisture

We used the time-varying H'_0 obtained in the last section to estimate the daily phases during DOY 182–243 in 2018 (Fig. 5.5(a)). For comparison, we also obtained the phases by the default method (Fig. 5.5(c)). We compared the phases to in situ soil moisture measurements to obtain their best linear fits as the mapping functions. The fit line for the modified method has a slope of $1.73\% \pm 0.07\% \text{ deg}^{-1}$ and an intercept of $22.2\% \pm 0.6\%$ (Fig. 5.5(b)). The one for the default method has a slope of $0.84\% \pm 0.04\% \text{ deg}^{-1}$ and an intercept of $30\% \pm 0.39\%$ (Fig. 5.5(d)). We used these parameters to convert the phases to soil moisture content shown in Fig. 5.6.

From the in situ measurements in Fig. 5.6, the surface soil underwent several drying/wetting cycles during DOY 182–243 in 2018, especially the one during DOY 201–218 with a magnitude of $\sim 10\%$. The soil moisture estimated by our method agrees well with the in situ ones (Fig. 5.6(a)). They capture the prominent drying/wetting feature and other cycles as well. The correlation coefficient between the in situ measurements and the estimates by our method is 0.82, and they have an RMSE of 1.51%. In contrast, for the soil moisture derived by the default method, we barely recognize

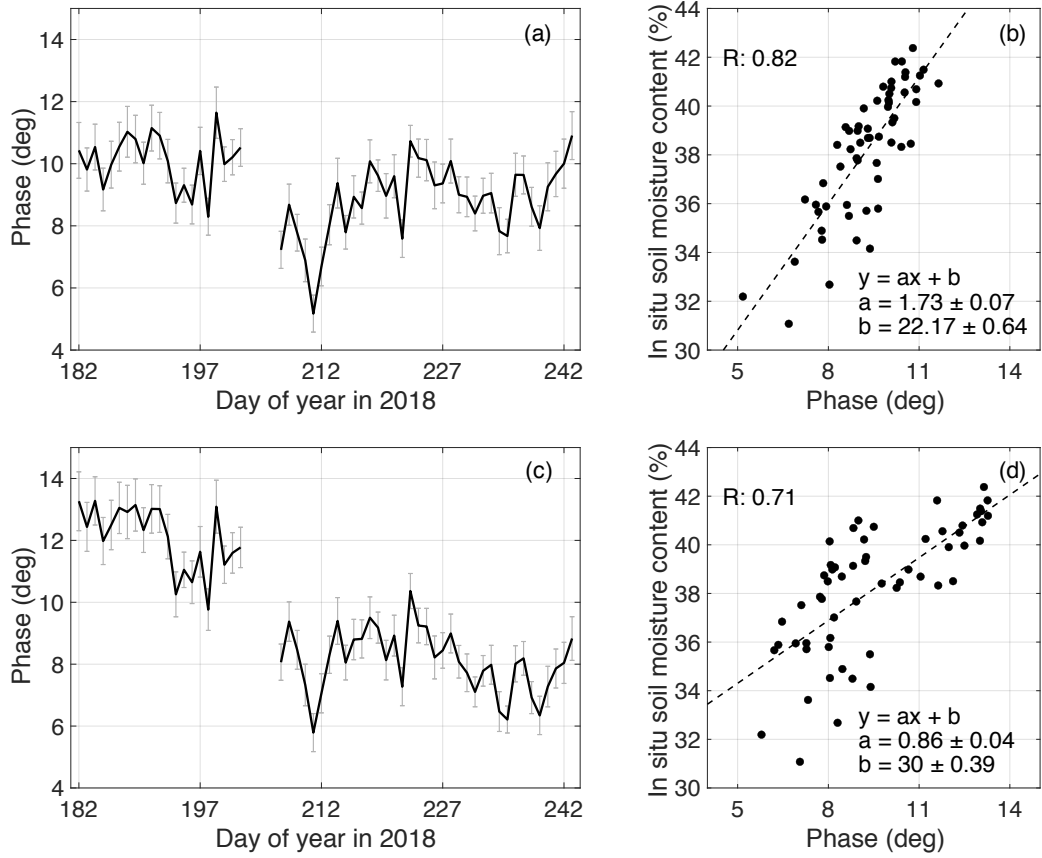


Figure 5.5: (a) Time series of the phases derived by our method during DOY 182–243 in 2018. Error bars denote their uncertainties. (b) Scatter plot between phases in (a) and in situ soil moisture and their best linear fit shown as a dashed line. The slope and intercept of the fit line are presented. We also show the correlation coefficient as R. (c) and (d) are similar to (a) and (b) correspondingly but for the results of the default method. The data gap during DOY 203–206 is due to the absence of SNR data.

the significant drying-wetting phenomenon during DOY 201–218. Furthermore, they exhibit an obvious descending trend. Based on the simulations in section 5.3.1, the phase bias is nearly proportional to surface deformation, and surface subsidence introduces a negative bias. In summer, when the thawing front advances deeper, the surface subsidence accumulates, then the bias decreases (with increasing absolute value). Accumulating surface subsidence gives rise to a decreasing trend of soil moisture estimates. The soil moisture estimates by the default method and in situ mea-

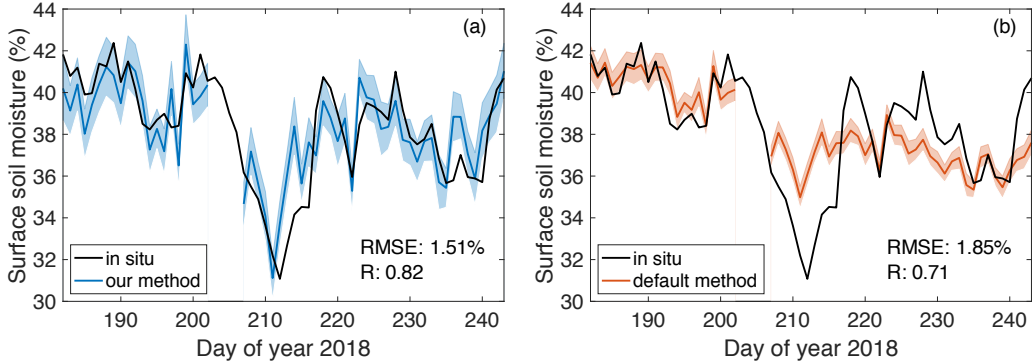


Figure 5.6: Time series of in situ soil moisture content and those measured by (a) our method and (b) the default method. The shaded areas denote the uncertainties of GNSS-IR estimates. The RMSE and correlation coefficient are presented.

surements have a correlation coefficient of 0.71 and an RMSE of 1.85%. In summary, our method outperforms the default one. Moreover, our results have a comparable accuracy with the ones reported in [Small et al. \(2010\)](#).

5.4.3 Snow depth

We obtained the GNSS-IR-measured snow depth during DOY 112–156 in 2017 (Fig. 5.7). Their uncertainties are on the order of several centimeters as well. From the manual measurements, the snow cover underwent several cycles of accumulation/ablation, e.g., the one during DOY 140–147. Consistently, the GNSS-IR measurements capture these processes. Figure 5.7(b) shows the scatter plot between the GNSS-IR and manual observations and their best linear fit. The correlation coefficient is 0.73. The GNSS-IR measurements have an RMSE of 4.11 cm and a bias of 2.49 cm.

The GNSS-IR measurements overestimate the snow depth, indicated by the positive bias. The main reason is possibly the difference of surface reflectivity between snow and wet soil at the beginning of thawing season. A detailed discussion is presented in section 5.5.3. Moreover, the possible penetration into soil when manually measuring snow depth may also affect the GNSS-IR measurements ([McCreight et al.](#),

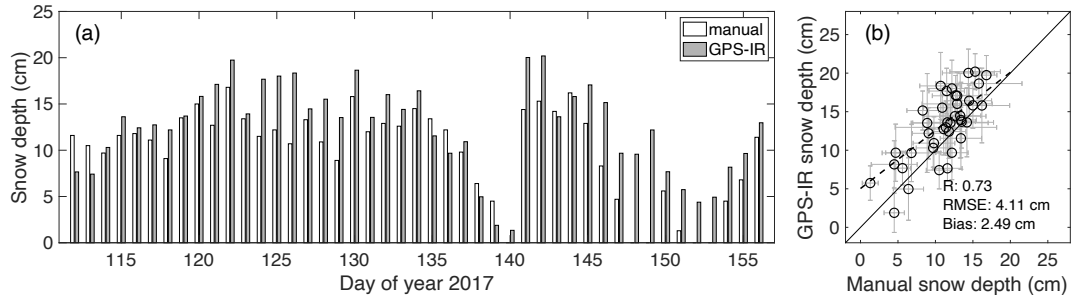


Figure 5.7: (a) Bar plots of snow depth measured by GNSS-IR and manually. We do not show the error bars for clarity. (b) Scatter plots of these two datasets and their best linear fit as a dashed line. We also show the correlation coefficient, RMSE, and bias.

2014). The penetration could compensate a part of the overestimation of GNSS-IR observations.

5.5 Discussion

5.5.1 Monument stability

We here assess the monument stability of QLBG and its impact on the GNSS-IR measurements of surface elevation changes and soil moisture content during DOY 182–243 in 2018. We noted in section 5.2 that the foundation depth of QLBG is slightly shallower than the active layer base. We computed the positioning measurements of QLBG during DOY 182–243 in 2018 in the local NEU coordinate reference system, by using GAMIT/GLOBK (<http://geoweb.mit.edu/gg/links.php>) and four IGS reference stations BJFS (39.61° N, 115.89° E), JFNG (86.54° N, 114.49° E), URUM (43.81° N, 87.60° E), and LHAZ (29.66° N, 91.10° E). The positioning results are presented in Fig. 5.8.

For the positioning observations in the east and north directions, their variations are as small as in the range of less than 1 cm. It implies that the monument has no sig-

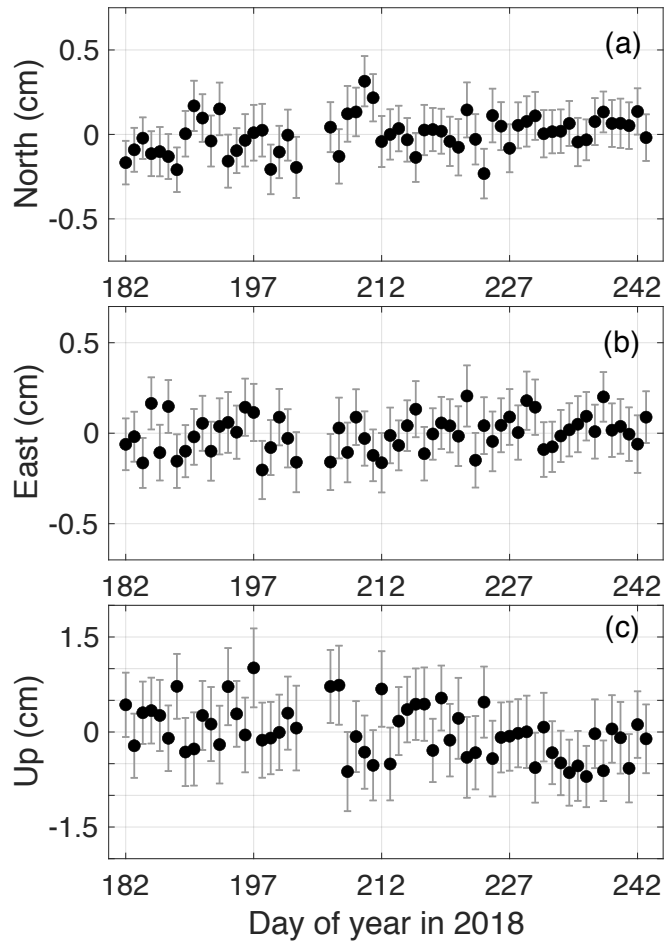


Figure 5.8: Positioning observations of QLBG in the (a) north, (b) east, and (c) up directions during DOY 182–243 in 2018. They are referenced to their mean values individually.

nificant inclination and the antenna is still in the up-right direction. The positioning results in the up direction are composed of monument displacements and solid earth movements, such as crustal motion and surface deformation due to atmospheric and hydrological loadings. Regarding the crustal movement, the velocity field of the contemporary crustal motion of QTP relative to the Eurasian plate has been constructed ([Gan et al., 2007](#); [Liang et al., 2013](#)). The magnitude of the uplift rate at our study site is less than 1 mm/year. The vertical crustal movement during DOY 182–243 in 2018 was

negligible. We used the simulated surface deformation provided by ESMGFZ (Earth System Modelling group of GFZ ([Dill and Dobslaw, 2013](#))) to examine the influence of surface loadings. The simulated values are shown in Fig. 5.9. During DOY 182–243 in 2018, the variation range of the surface deformation due to the atmospheric loading was around 9 mm, and that of continental hydrology was 4 mm. We removed the contributions of the surface loadings from the positioning results and used the residuals to be the vertical monument movement, which are shown in Fig. 5.10. The monument movement is relatively noisy, and varies in a range of 1.5 cm. We built a best linear fit for them and found that they did not present a statistically significant trend as $0.003 \pm 0.004 \text{ cm} \cdot \text{day}^{-1}$ (t-test, $\alpha = 0.05$). The monument movement follows a Gaussian normal distribution with the mean of 0 cm and the standard deviation of 0.42 cm. It barely affects the constant H_0 . The monument movement also has little impact on the GNSS-IR-measured surface elevation changes, as we focus on their temporal variations.

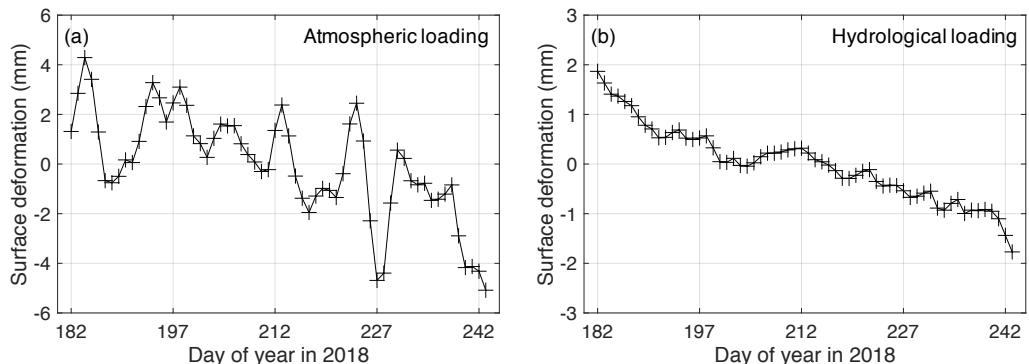


Figure 5.9: Surface deformation due to (a) atmospheric loadings and (b) continental hydrological loadings, respectively, during DOY 182–243 in 2018. They are referenced to their mean values individually.

In the modified method, the time-varying H_0' comprises the constant H_0 and the modeled surface elevation changes. Here, we assess the impact of the vertical monument movement on the model parameters and modeled surface elevation changes.

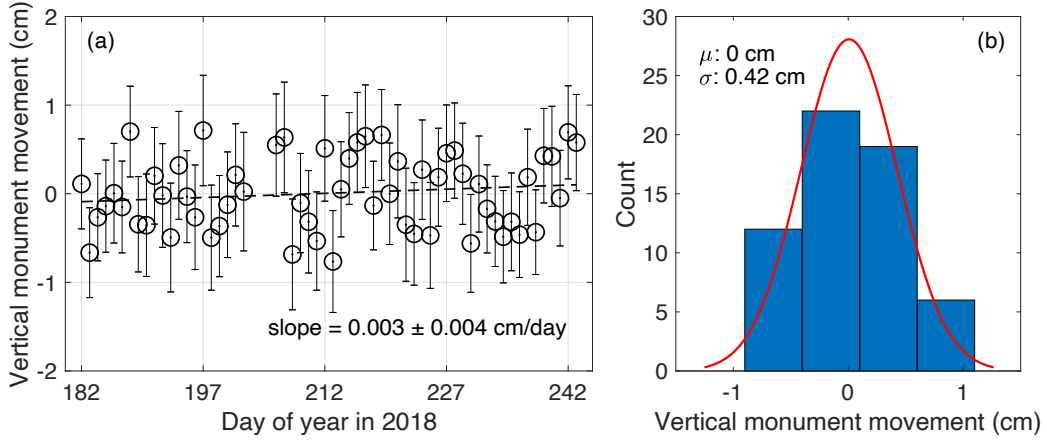


Figure 5.10: (a) Time series of the vertical monument movement during DOY 182–243 in 2018. Their best linear fit line is also presented as a dashed line with the slope of $0.003 \pm 0.004 \text{ cm} \cdot \text{day}^{-1}$. (b) Histogram of the vertical monument movements and their normal distribution fit (red curve). The mean (μ) and standard deviation (σ) of this normal fit are 0 cm and 0.42 cm, respectively.

Considering the vertical movement (denoted as v hereafter), based on equation 5.1, the model expression is changed to

$$d(\tau) + v(\tau) = s\tilde{I}_T + d_0. \quad (5.3)$$

The essence of studying the impact of v on the model parameters is to investigate the dependence of v on \tilde{I}_T . We built a scatter plot between v and \tilde{I}_T (Fig. 5.11). The correlation coefficient between them is as weak as 0.14. This result can be expected as the vertical movement is almost white noise whereas the thermal indices possess an increasing trend. The weak correlation indicates that the monument movement has little impact on the estimates of s and d_0 , then the modeled surface elevation changes. Together with the discussion in the last paragraph, the vertical monument movement has little impact on the time-varying reflector height H'_0 , thus barely affect the phases and soil moisture estimates.

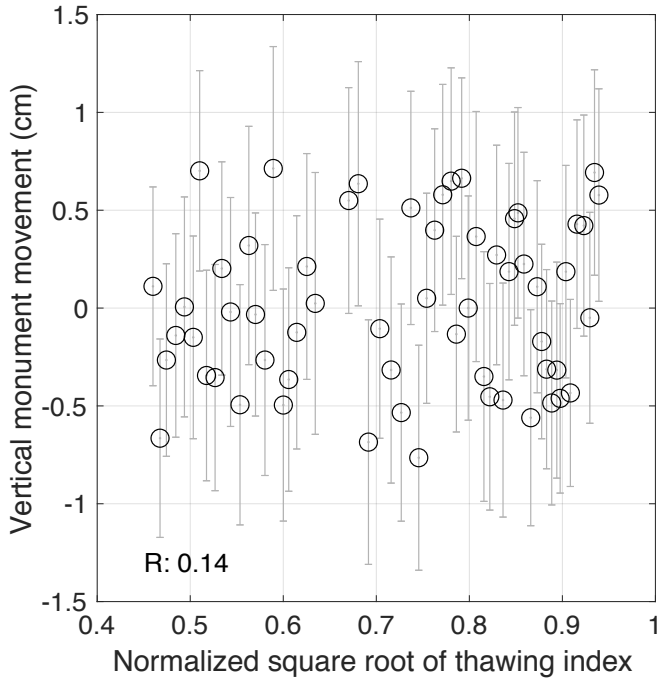


Figure 5.11: Scatter plot between the square root of normalized thawing index and the vertical monument movement during DOY 182–243 in 2018.

5.5.2 Error sources of the improved method

The error sources of the improved method are related to antenna gain pattern, surface conditions (i.e., vegetation and soil moisture), and the GNSS-IR geometry. The receiver antenna is designed to favor the reception of direct signals and suppress those with low elevation angles and the reflected ones. It has an asymmetric gain pattern along the elevation angle. For any SNR series with the same elevation angles, they suffer from the same impact. Therefore, the influence of antenna gain pattern on the SNR phases can be regarded as a systematic bias. As we focus on the temporal variations, the impact of antenna gain pattern is negligible.

The surface reflectivity for the L-band GNSS signal varies with elevation angle. It is dominantly determined by soil moisture content in permafrost areas, where the vegetation is typically shorter than the wavelength of the satellite signal ([Ulaby and](#)

[Long, 2015](#)). Due to surface reflectivity, the phase of each point of a given SNR interferogram is slightly different, i.e., the phase term $\phi(e)$ in equation 1.11 is a variable. Assuming the phase as a constant in data processing might introduce errors. [Zavorotny et al. \(2010\)](#) simulated SNR in bare soil with a smooth reflecting surface. The phase variation with respect to the elevation angle is nearly the same, given a change of soil moisture content. It indicates that assuming the phase as a constant has little impact on the GNSS-IR estimates of soil moisture, as we focus on the temporal changes of the phases. The vegetation's impact is negligible, as it is sufficiently short to be transparent for the GNSS signals.

Regarding the error sources related to the GNSS-IR geometry, they affect the soil moisture estimates through the GNSS-IR-measured surface elevation changes, which are used to calculate the time-varying H'_0 . The error sources are mainly monument stability, monument thermal contraction/expansion, tropospheric delays of the GNSS signals, and soil moisture. The impact of monument stability has been discussed in the last section 5.5.1. As for the thermal expansion/contraction of the monument, the coefficient of linear thermal expansion of galvanized steel is $11\text{--}13 \times 10^{-6} \text{ m}\cdot(\text{m}\cdot^\circ\text{C})^{-1}$. Given a temperature range of 20°C in a thawing season, for a 2-m-high monument, the magnitude of the thermal expansion is less than 1 mm, at least one order of magnitude smaller than the uncertainties of surface elevation changes. Regarding the tropospheric delays, we used the in situ measurements of air temperature and pressure to quantify them, based on the refraction correction model of [Bennett \(1982\)](#). The tropospheric biases are $\sim 1.3 \text{ cm}$ and relatively steady (Fig. 5.12). As we focus on the temporal changes of surface elevation changes, the impact of tropospheric bias is limited. The temporal variation of soil moisture may also introduce bias to the GNSS-IR-measured surface elevation changes. Assuming the phase as a constant introduces a bias to the frequency retrieval then reflector height. Such bias is called compositional reflector height, as it manifests itself as a part of reflector height ([Nievinski,](#)

2013). Liu and Larson (2018) conducted simulations and found that the bias was less than 2 cm and varied in the range of less than 1 cm, given soil moisture between 15% and 40%. In this study, such bias is expected to be limited, as the precipitation is scarce and light in the cold and dry plateau climate and that we focus on the temporal changes of the surface elevations.

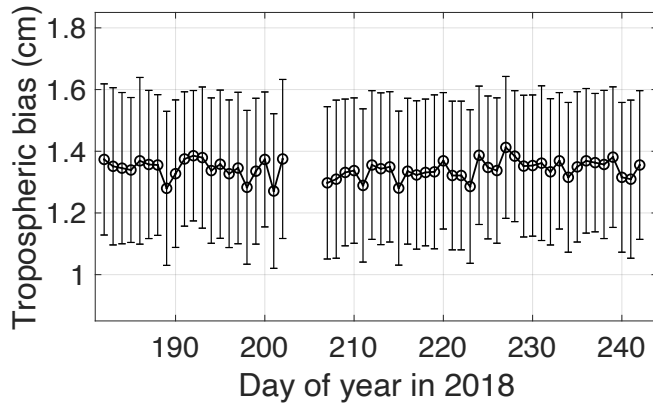


Figure 5.12: Tropospheric biases of surface elevation changes during DOY 182–243 in 2018. They are the mean values of the biases of all satellite tracks, whose standard deviations are represented by error bars.

5.5.3 Impact of surface reflectivity on snow depth

In the framework of GNSS-IR, snow depth is derived as the difference between the reflector height of snow surface and the one of ground surface (1.5). In our study, we use the reflector height at the beginning of thawing season as a reference. Based on the in situ measurements, the mean volumetric moisture content at the depth of 1 cm during DOY 167–173 in 2017 was $\sim 38\%$. Given the significant contrast of moisture content between snow and thawed soil, their difference in surface reflectivity for GNSS signals might affect the GNSS-IR-estimated snow depth.

We used the multipath simulator of Nievinski and Larson (2014) to simulate SNR in the conditions of snow and wet soil. The key parameters for the simulations are

Table 5.2: Parameters for SNR simulations in snow-free and snow-cover conditions.

Parameter	Value
Antenna (Radome)	TRM29659.00 SCIT
Signal	L1 C/A
Antenna height	2 m
Azimuth range	90–135°
Elevation angle	5–20°
Snow-free condition	Sandy loam with a volumetric moisture content of 38%
Snow-cover condition	Dry snow with default properties in Nievinski and Larson (2014)

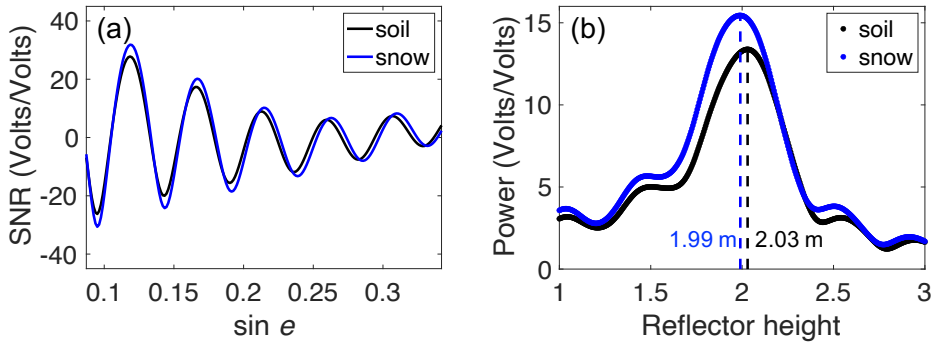


Figure 5.13: (a) Simulated SNR observations with the reflector of wet soil (black curve) and snow (blue curve). (b) Frequency spectrums of the simulated SNR observations. The frequency has been converted into reflector height. The dominant reflector height with peak power is 2.03 m for wet soil, whereas 1.99 m for snow.

presented in Table 5.2. The simulated SNR observations and their LSP analysis results are presented in Fig. 5.13. The dominant reflector height corresponding to the peak power is 1.99 m for snow, whereas 2.03 m for wet soil. The reflectivity difference between snow and wet soil does affect SNR observations and introduces a bias to reflector height retrievals consequently to snow depth measurements. In the simulations, a bias of 4 cm is introduced, making the GNSS-IR measurements overestimate the snow depth, which is consistent with our finding in section 5.4.3.

5.5.4 Benefits of the three-in-one framework

The three-in-one framework can fully utilize the GNSS-IR in permafrost studies. We can obtain the GNSS-IR measurements of three key variables by one station, which is crucially important due to the lack of observations in the extensive permafrost areas.

The obtained GNSS-IR measurements can be directly used to study the changes in permafrost areas at local scales. We can use the snow depth results to study the variation of snow cover and its insulating effect and hydrological impact on the frozen ground. The ground surface elevation changes can indicate the amount of melting ground ice and the changes of active layer thickness with ancillary information such as soil moisture profiles. The active layer thickness can be estimated based on seasonal subsidence and soil moisture profile (Liu et al., 2012). The measurements of soil moisture content aid in studying water cycles, surface energy balance, the interaction between the atmosphere and the frozen ground.

The GNSS-IR measurements can be used to calibrate/validate the remote sensing observations in regional scales. At present, surface elevation changes, soil moisture, snow depth can be provided by air and space-borne measurements, such as InSAR measurements for surface elevation changes (Liu et al., 2010), SMAP data for soil moisture content (Entekhabi et al., 2010), and snow depth estimated from passive microwave radiometry data (Walker and Silis, 2002; Che et al., 2008). These remote sensing observations have relatively broad spatial coverages, typically on the order of several tens of kilometers. The GNSS-IR measurements can be used to calibrate/validate the remote sensing observations. We have conducted a comprehensive analogy between GNSS-IR and InSAR in section 6.2.2, which shows their complementary nature. Their synergy can provide improved, insightful, and quantitative observations. The three-in-one framework can be also extended to other GNSS sites, such as those in the Arctic.

5.6 Conclusion

This study highlights the improvement to the default GNSS-IR algorithm for estimating soil moisture content in permafrost regions. It can correct the bias introduced by the seasonal surface elevation changes. The SNR data and the in situ measurements of soil moisture at QLBG have been used to validate this modified method. The correlation coefficient and RMSE between the GNSS-IR estimates and the in situ ones improve from 1.85% to 1.51% and 0.71 to 0.82, respectively.

We implemented a framework to integrate the GNSS-IR measurements of ground surface elevation changes, soil moisture, and snow depth at one single site, and illustrated it by using QLBG. This framework helps to fully use GNSS-IR in permafrost regions. It can also be extended to other sites, for instance, those in the Arctic.

This study is also the first to use GNSS-IR in QTP. The site QLBG fills a spatial gap in the existing sparse permafrost-monitoring sites. Its GNSS-IR measurements are complementary to the existing observations, such as active layer thickness and ground temperature.

End of chapter.

Chapter 6

Conclusion

6.1 Contributions

In this thesis, we identified 23 suitable sites in the Arctic permafrost areas for GNSS-IR studies by screening the major open-data GNSS networks. Most of them are located in northern Canada and Alaska, and a few are scattered in the Eurasian permafrost areas. The reflector heights have been obtained at these usable sites, which can be converted into surface elevation changes in snow-free seasons and snow depth otherwise. As for the unusable ones in the permafrost areas, the dominant causes are the undulated surface, surrounding obstruction, such as trees, tall shrubs, and buildings, and insufficient SNR data. It implies that better location choices are needed when installing GNSS sites in the future. A site of QLBG in northeastern QTP has also been proved to be useful for GNSS-IR applications as well.

We used the multi-year, continuous, and daily GNSS-IR measurements of surface elevation changes to study frozen ground dynamics in various temporal scales.

- We investigated the multi-year linear trend at five sites in the Canadian Arctic, i.e., Alert, Resolute Bay, Repulse Bay, Baker Lake, and Iqaluit. We found that the ground surface underwent multiple-year subsidence by 0.61 ± 0.04

$\text{cm}\cdot\text{yr}^{-1}$ during 2012–2018 in Alert, $0.70 \pm 0.02 \text{ cm}\cdot\text{yr}^{-1}$ during 2003–2014 in Resolute Bay, $0.17 \pm 0.02 \text{ cm}\cdot\text{yr}^{-1}$ during 2010–2020 in Baker Lake, and $0.10 \pm 0.02 \text{ cm}\cdot\text{yr}^{-1}$ during 2010–2020 in Iqaluit. The vertical surface movement during 2014–2020 in Repulse Bay was not significant with the rate of $0.01 \pm 0.04 \text{ cm}\cdot\text{yr}^{-1}$ (t-test, $\alpha = 0.05$). We also found that Alert, Resolute Bay, and Baker Lake had warming thawing seasons. It indicates that the subsidence at these three sites was possibly caused by near-surface permafrost degradation induced by warming air temperature. On the contrary, Iqaluit had cooling summers. The impact of air temperature might be moderated by other environmental variables, such as vegetation, soil moisture, and ground ice near the permafrost table. Thus, at Iqaluit, the ground surface still underwent a subsidence trend in the cooling thawing seasons.

- Regarding seasonal surface elevation changes, we observed that they were irregular in most years at each Canadian Arctic site. Through comparing vertical surface movement and square-root-of-thawing indices, we found that the Stefan equation fails in most years at each site, by showing positive or weakly negative correlation coefficients. This implies that the simplification of soil properties and heat transfer process behind the Stefan equation cannot fully represent the real conditions at the study sites. Through the correlation between average seasonal surface deformation and mean normalized \sqrt{DDT} , the soil conditions at Alert and Baker Lake are closer to the assumed cases of the Stefan equation, compared with the other sites.
- At Resolute Bay, we observed that the end-of-thaw elevations were highly negatively correlated with square-root-of-thawing indices during 2003–2012, whereas they were low in 2013 and 2014 with cool summers. This significant change in correlation during 2013–2014 was postulated to be caused by the

changes in soil properties and ground ice content at the active layer base, triggered by the extremely warm summer in 2011. The heat still could penetrate into deep frozen ground to cause low end-of-thaw elevations during 2013–2014.

- We used the GNSS-IR-estimated seasonal subsidence in Utqiagvik, Alaska, to infer the moist-to-dry shift of the active layer from 2004–2008 to 2009–2018. By comparing the seasonal subsidence with the square-root of thawing index, we found that their ratio during 2004–2008 was $0.43 \pm 0.04 \text{ cm} \cdot (\text{°C} \cdot \text{days})^{-1/2}$ whereas $0.18 \pm 0.01 \text{ cm} \cdot (\text{°C} \cdot \text{days})^{-1/2}$ during 2009–2018. Thus, the seasonal subsidence was more sensitive to the thawing index during 2004–2008. We hypothesized that the soil moisture decrease caused this significant change. In situ measurements of soil moisture content validated this hypothesis by showing a decreasing trend in the soil down to 35 cm depth during 2004–2008 and keeping relatively stable during 2009–2016. The dry top soil has lower thermal conductivity and becomes inefficient for heat conduction. It impedes the heat transfer into the deeper ground and affects the ground thermal regime. Consequently, it leads to a shallower active layer. The relatively dry and shallower active layer contributed together to the smaller ratio during 2009–2018.

We also improved the commonly-used GNSS-IR algorithm for estimating surface soil moisture, which does not consider the impact of seasonal surface deformation in permafrost areas. We introduced the modeled surface elevation changes into the default algorithm to mitigate the seasonal bias. We validated our method by using the SNR data and in situ observations at QLBG in the northeastern QTP. As a result, the RMSE and correlation coefficient between the GNSS-IR estimates of soil moisture content and in situ ones improve from 1.85% to 1.51% and 0.71 to 0.82, respectively. We also implemented a three-in-one framework to integrate the GNSS-IR estimates of surface elevation changes, surface soil moisture, and snow depth at one site and illustrated it by using QLBG as an example.

In summary, this thesis provides numerous usable GNSS sites to fill the spatial gaps of the existing permafrost monitoring programs. Their GNSS-IR measurements of surface elevation changes complement the core observations, such as active layer thickness and ground temperature. They also contribute to quantifying frozen ground dynamics and revealing its thermal and hydrological changes. The improved GNSS-IR algorithm helps to estimate surface soil moisture in permafrost regions reliably. The three-in-one framework can be applied to other suitable sites.

6.2 Future work

6.2.1 Supersites for monitoring permafrost areas

The environmental variables, including vegetation, soil type, soil moisture, and ground ice content, moderate the impact of air temperature on frozen ground, consequently affecting its thermal regime, indicated by our studies, including the multi-year subsidence trend in cooling summers in Iqaluit, the change of the correlation sign between the end-of-thaw elevations and square-root-of thawing indices from 2003–2012 to 2013–2014 in Resolute Bay, and the variation in the ratio between seasonal subsidence and square-root-of thawing indices from 2004–2008 to 2009–2020 in Utqiagvik, Alaska. The dominance of air temperature and other environmental variables in frozen ground dynamics may vary. [Shur and Jorgenson \(2007\)](#) proposed a classification system to describe the complex interaction of climatic and ecological processes in permafrost formation, which contains five categories as climate-driven, climate-driven and ecosystem-modified, climate-driven and ecosystem protected, ecosystem-driven, and ecosystem-protected permafrost. The weights of climatic and ecological factors involving permafrost changes are different in each category. For example, air temperature dominates the formation of climate-driven permafrost, whereas the ecosystem-driven permafrost usually occurs in the low-lying, poorly-drained, and

north-facing areas.

The influence of the variables mentioned above on frozen ground has not been completely resolved. For instance, contradictory studies of the impact of soil moisture increase on permafrost thermal state have been reported. Wu et al. (2015) observed active layer thickening at a permafrost site in central QTP, where the air temperature did not show a significant warming trend but the summer rainfall rose obviously. The wetting soil might be the cause for the deepening active layer. Mekonnen et al. (2021) obtained similar results by conducting simulations under the expected wetting scenario in the Arctic. Göckede et al. (2019) observed a decrease in the ground temperature and active layer thickness at a drainage site with decreasing soil moisture compared with a control site with saturated soil. However, Zhang et al. (2021a) reported an opposite result. They conducted simulations to find that, in QTP, soil wetting could reduce the impact of air temperature by leading to a shallower active layer and cooler ground temperature than the expected one solely considering air temperature. At the current stage, the lack of sufficient in situ measurements makes it challenging to clearly reveal the processes of how the ecological variables moderate and even excel the air temperature's impact.

Supersites are called for monitoring permafrost changes and investigating their interactions with the surrounding environment, where sufficient variables can be measured. One of the candidates is the QLBG site in QTP. This site already has an integrated weather station recording various meteorological factors, such as air temperature, precipitation, wind, and radiation (Che et al., 2019). These records can be used to quantify the climatic and ecological forcings. However, the observations for characterizing the frozen ground is not sufficient. The ground temperature and soil moisture are measured only to the depth of 1.6 m. The active layer thickness cannot be resolved as it is deeper than 1.6 m in recent years. Moreover, the description of soil texture is coarse. The ground ice content near the permafrost table is not measured.

To upgrade this site into a super one, we need to install more sensors in deeper depths to observe ground temperature and soil moisture. We also need to conduct a detailed description of soil profile and ground ice content at the active layer base.

Another candidate is the SG27 site in Utqiagvik, Alaska. Numerous studies have been conducted here to study active layer thickness and its relationship with air temperature, organic layer, soil moisture, and ground ice content (Nelson et al., 1998; Shiklomanov et al., 2010; Streletschi et al., 2017). The Barrow Atmospheric Baseline Observatory (<https://gml.noaa.gov/dv/site/index.php?stacode=brw>) records various meteorological factors, such as air temperature, pressure, relative humidity, wind, and radiation, spanning over several decades. As for monitoring frozen ground, the CALM site, U1, exists to report active layer thickness annually. The soil climate station (U1-1) measures moisture content and ground temperature at the depths of 5 cm, 20 cm, and 35 cm (Fig. 4.1). However, SG27 has the similar limitations to QLBG, which lacks sufficient observations of frozen ground. The spatial coverage of U1 is not consistent with the one of U1-1, indicating that the active layer thickness measured at U1 might not valid at U1-1, given a large spatial heterogeneity in active layer thickness (Shiklomanov et al., 2010). Moreover, the ground temperature at 35 cm has been above 0 °C in recent years. The current sampling depths cannot fully characterize the thermal regime of the frozen ground. We need to monitor the ground temperature and soil moisture at deeper depths and describe the soil profile and ground ice condition in detail.

6.2.2 Synergy between GNSS-IR and SAR/InSAR¹

SAR/InSAR has been widely used to study permafrost in recent years, e.g., estimating surface deformation, active layer thickness, surface soil moisture, and ground ice loss (Liu et al., 2010, 2012; Zwieback and Berg, 2019; Daout et al., 2020). The application fields of SAR/InSAR have a large overlap with the ones of GNSS-IR. Here, we analogize them by the following aspects:

- *Tropospheric delay.* For GNSS-IR, only the tropospheric delay of the additional path of the reflected signal with respect to the direct one should be considered. Its magnitude mainly depends on precipitable water vapor and antenna height above surface. For a typical several-meter-high station in permafrost areas, the tropospheric bias of surface vertical movement is limited, e.g., ~ 1.6 cm for the 2.3 m-high station RESO in Resolute Bay, Canada (Zhang et al., 2020) and ~ 1.3 cm for the 2 m-high QLBG in QTP (Zhang et al., 2021b). They are also nearly stable throughout the thaw season. The tropospheric impacts can be neglected, as we only focus on the temporal changes of surface vertical movement. As for InSAR, the differential tropospheric delays between the SAR acquisitions negatively affect the accuracy of deformation in both spatial and temporal domains. Various methods and independent products, including GNSS observation-based tropospheric delays, can be utilized for mitigating the tropospheric delays for InSAR.
- *Effect of vegetation.* The vegetation has a negligible impact on the L-band GNSS signals when its height is shorter than the wavelength of the satellite signals. In areas with taller vegetation, the magnitude and oscillation of SNR observations respond to vegetation growth condition (Small et al., 2010). However, the

¹This section is based on Jiahua Zhang and Lin Liu (2021). Studying frozen ground dynamics by using GNSS interferometric reflectometry: achievements and potential synergy with InSAR. IEEE International Geoscience and Remote Sensing Symposium.

feasibility of using the frequency and amplitude of SNR data to estimate vegetation parameters depends on vegetation types. Small et al. (2010) found that the SNR data did not present clear interference patterns when the corn was ~ 2 m tall. Whereas, (Zhang et al., 2017b) used the frequency of SNR data to estimate the height of wheat. The space-borne SAR sensors, operating at various wavelengths, such as X-, C- and L-band, have different sensitivities to vegetation canopy and structure. Temporal changes of vegetation lead to interferometric decorrelation, especially for short-wavelength radar signals. On the other hand, SAR Tomography, SAR Polarimetry and Polarimetric Interferometry can be used to build vegetation structure and retrieve biomass.

- *Effect of soil moisture.* The GNSS-IR geometry is affected by soil moisture variation. Such impact is not uniform for the reflection points, i.e., $\phi(e)$ varies with elevation angle in equation 1.11. Taking $\phi(e)$ as a constant in practice introduces uncertainties to the measurements of surface elevation changes. Nievinski and Larson (2014) proposed a multipath simulator to quantify such uncertainties. Temporal soil moisture changes also affect InSAR phases, decrease coherence, and introduce non-zero closure phase (phase triplet). In permafrost areas, since soil moisture changes abruptly during freeze-to-thaw and thaw-to-freeze transition seasons, decorrelation is severe and impedes the capability of InSAR for measuring deformation. Soil moisture changes, if continuously wetting or drying for weeks within a thaw season, may also introduce systemic bias in the InSAR-measured deformation time series. A few studies have explore the use of closure phases to evaluate the influence of soil moisture on InSAR phase and coherence (e.g., Zwieback et al., 2016).
- *Sensitivity to lateral ground movement.* GNSS-IR is insensitive to the lateral movement of ground surface. It requires the ground surface to be relatively

horizontal and flat. Horizontal movement, therefore, tends not to be detected by GNSS-IR. Whereas, line-of-sight InSAR measurements can be mapped to the vertical and horizontal directions and provide surface elevation changes and lateral movement.

- *Sensitivity to solid earth movement.* GNSS-IR measurements are free of solid earth movement if the monument is deeply anchored. InSAR, depending on the choice of reference point, measures combined displacements of solid earth and frozen ground.
- *Capability of mapping thermokarst landforms.* GNSS-IR is not feasible in thermokarst landforms due to their large surface roughness. InSAR may still be useful but challenging because of the loss of coherence (Liu et al., 2015). Single-pass InSAR from bistatic TanDEM-X data has been explored to observe the elevation changes of thaw slumps (Zwieback et al., 2018).
- *Necessity of reference point.* InSAR requires a reference point with known surface deformation or assumed to be stable. Reflector heights retrieved from GNSS-IR measurements do not require any reference point.
- *Temporal and spatial resolutions.* The GNSS-IR measurements are daily and at local scales ($\sim 1000 \text{ m}^2$). In contrast, the InSAR observations have coarser temporal resolutions (typically 6 days to about one month) and much broader spatial coverages on the order of tens to hundreds of kilometers.
- *Uncertainty of the measurement.* The uncertainties of GNSS-IR-retrieved surface elevation changes are on the order of several centimeters, whereas a few millimeters for InSAR.

A synergy of GNSS-IR and SAR/InSAR can combine their strengths and compensate for the limitations. For instance, daily and continuous GNSS-IR measurements

help to tie InSAR measurements with gaps in time (e.g., InSAR coherence loss in thawing seasons) and between missions (such as L-band ALOS-1, ALOS-2, ALOS-4, and NISAR). The GNSS sites can provide reference points for InSAR measurements in two ways: by providing (1) the GNSS-IR measurements to quantify the frozen ground changes and (2) the positioning results to correct the solid earth movement. Given their various sensitivities to surrounding environment (topography, soil, vegetation), the combination of GNSS-IR and SAR/InSAR aid in obtaining improved, quantitative, and insightful measurements in fine temporal resolutions and over broad permafrost regions.

End of chapter.

Appendix A

Output

A.1 Publication

Jiahua Zhang, Lin Liu, Lei Su, and Tao Che (2021). Three in one: GPS-IR measurements of ground surface elevation changes, soil moisture, and snow depth at a permafrost site in the northeastern Qinghai–Tibet Plateau. *The Cryosphere*, 15, 3021–3033, <https://doi.org/10.5194/tc-15-3021-2021>.

Jiahua Zhang and Lin Liu (2021). Mining noise data for monitoring Arctic permafrost by using GNSS interferometric reflectometry. *Polar Science*, 100649, <https://doi.org/10.1016/j.polar.2021.100649>.

Jiahua Zhang, Lin Liu, and Yufeng Hu (2020). Global Positioning System interferometric reflectometry (GPS-IR) measurements of ground surface elevation changes in permafrost areas in northern Canada. *The Cryosphere*, 14(6), 1875–1888. <https://doi.org/10.5194/tc-14-1875-2020>.

Yufeng Hu, Lin Liu, Kristine Larson, Kevin Schaefer, **Jiahua Zhang**, and Yibin Yao (2018). GPS Interferometric Reflectometry Reveals Cyclic Elevation Changes in Thaw and Freezing Seasons in a Permafrost Area (Barrow, Alaska). *Geophysical Research Letters*, 45, 5581–5589. <https://doi.org/10.1029/2018GL077960>.

A.2 Conference paper and presentation

2021

Jiahua Zhang and Lin Liu (2021). Studying frozen ground dynamics by using GNSS interferometric reflectometry: achievements and potential synergy with InSAR. IEEE International Geoscience and Remote Sensing Symposium, accepted.

Jiahua Zhang and Lin Liu (2021). Utilizing the full potentials of GNSS interferometric reflectometry for quantifying permafrost changes in a warming climate. China & the Arctic: A View to 2050, Hong Kong, China.

2020

Jiahua Zhang, Lin Liu, and Kang Wang (2020). Drying active layer in Utqiagvik, Alaska revealed from the GPS-IR-measured seasonal subsidence during 2004–2019, AGU Fall meeting, virtual meeting.

Jiahua Zhang and Lin Liu (2020). Mining noisy data for monitoring Arctic permafrost by using GNSS Interferometric Reflectometry, Sixth International Symposium on Arctic Research, virtual meeting.

2019

Jiahua Zhang, Tao Che, Lei Su, and Lin Liu (2019). Three-in-one: GPS-IR measurements of surface soil moisture, snow depth, and ground surface elevation changes at a permafrost site in Northeastern Qinghai-Tibet Plateau, AGU Fall meeting, San Francisco, U.S.

2018

Jiahua Zhang, Lin Liu, and Yufeng Hu (2018). Investigating the changes in surface elevation of permafrost terrain in the Canadian Arctic measured by GPS Interferometric reflectometry, AGU Fall meeting, Washington D.C., U.S.

Jiahua Zhang, Lin Liu, and Yufeng Hu (2018). Investigating the decadal changes of frozen ground at Resolute Bay in the Canadian High Arctic through surface elevation changes measured by GPS Interferometric Reflectometry, 15th International

Circumpolar Remote Sensing Symposium, Potsdam, Germany

Jiahua Zhang, Lin Liu, and Yufeng Hu (2018). Investigating the decadal changes of frozen ground at Resolute Bay in the Canadian Arctic by using surface elevation changes estimated by GPS Interferometric Reflectometry, 3rd Congress of China Geodesy and Geophysics, Lanzhou, China

2017

Yufeng Hu, Lin Liu, Kristine M. Larson, Kevin M. Schaefer, **Jiahua Zhang** (2017). Freezing-season ground uplift over permafrost area estimated using GPS Interferometric Reflectometry, International Symposium on GNSS, Hong Kong, China

A.3 Data

Jiahua Zhang, Lin Liu, and Yufeng Hu (2019). Reflector heights measured by GPS-IR at Alert, Resolute Bay, Repulse Bay, Baker Lake, and Iqaluit in northern Canada. PANGAEA. <https://doi.org/10.1594/PANGAEA.904347>.

Jiahua Zhang and Lin Liu (2020). Reflector heights in the Arctic permafrost areas measured by GNSS interferometric reflectometry (Version 0.1.0). Zenodo. <https://doi.org/10.5281/zenodo.4319372>.

Jiahua Zhang, Lin Liu, Lei Su, and Tao Che (2021). GPS-IR measurements of ground surface elevation changes, surface soil moisture, and snow depth at a permafrost site in northeastern Qinghai-Tibet Plateau. Zenodo. <http://doi.org/10.5281/zenodo.4895864>

The GNSS-IR measurements are also archived on my personal academic website as <https://jiahua-gnssr.com>.

□ End of chapter.

Bibliography

- Anderson, K. D. (1996). A global positioning system (GPS) tide gauge. Technical report, Advisory Group for Aerospace Research and Development (AGARD).
- Bennett, G. G. (1982). The Calculation of Astronomical Refraction in Marine Navigation. *Journal of Navigation*, 35(2):255–259.
- Biskaborn, B. K., Smith, S. L., Noetzli, J., Matthes, H., Vieira, G., Streletschiy, D. A., Schoeneich, P., Romanovsky, V. E., Lewkowicz, A. G., Abramov, A., Allard, M., Boike, J., Cable, W. L., Christiansen, H. H., Delaloye, R., Diekmann, B., Drozdov, D., Etzelmüller, B., Grosse, G., Guglielmin, M., Ingeman-Nielsen, T., Isaksen, K., Ishikawa, M., Johansson, M., Johannsson, H., Joo, A., Kaverin, D., Kholodov, A., Konstantinov, P., Kröger, T., Lambiel, C., Lanckman, J.-P., Luo, D., Malkova, G., Meiklejohn, I., Moskalenko, N., Oliva, M., Phillips, M., Ramos, M., Sannel, A. B. K., Sergeev, D., Seybold, C., Skryabin, P., Vasiliev, A., Wu, Q., Yoshikawa, K., Zheleznyak, M., and Lantuit, H. (2019). Permafrost is warming at a global scale. *Nature Communications*, 10(1):264.
- Brewer, M. C. (1958). Some results of geothermal investigations of permafrost in northern Alaska. *Transactions, American Geophysical Union*, 39(1):19.
- Brown, J., Ferrians Jr, O. J., Heginbottom, J. A., and Melnikov, E. S. (1997). *Circum-Arctic map of permafrost and ground-ice conditions*. US Geological Survey Reston, VA.
- Brown, J. and Sellmann, P. V. (1973). Permafrost and coastal plain history of arctic alaska. *Alaskan arctic tundra. Edited by M.E. Britton. Arctic Institute of North America. Technical paper No.25*. Publisher: Washington, pages 31–47.
- Bruyninx, C., Legrand, J., Fabian, A., and Pottiaux, E. (2019). GNSS metadata and data validation in the EUREF Permanent Network. *GPS Solutions*, 23(4):106.
- Burgess, M., Smith, S., Brown, J., Romanovsky, V., and Hinkel, K. (2000). Global terrestrial network for permafrost (gtnet-p): Permafrost monitoring contributing

to global climate observations. *Geological Survey of Canada, Current Research*, 2000-E14.

Camps, A., Park, H., Pablos, M., Foti, G., Gommenginger, C. P., Liu, P.-W., and Judge, J. (2016). Sensitivity of GNSS-R Spaceborne Observations to Soil Moisture and Vegetation. *IEEE Journal of Selected Topics in Applied Earth Observations and Remote Sensing*, 9(10):4730–4742.

Carreno-Luengo, H., Lowe, S., Zuffada, C., Esterhuizen, S., and Oveisgharan, S. (2017). Spaceborne GNSS-R from the SMAP Mission: First Assessment of Polarimetric Scatterometry over Land and Cryosphere. *Remote Sensing*, 9(4):362.

Che, T., Li, X., Jin, R., Armstrong, R., and Zhang, T. (2008). Snow depth derived from passive microwave remote-sensing data in China. *Annals of Glaciology*, 49:145–154.

Che, T., Li, X., Liu, S., Li, H., Xu, Z., Tan, J., Zhang, Y., Ren, Z., Xiao, L., Deng, J., Jin, R., Ma, M., Wang, J., and Yang, X. (2019). Integrated hydrometeorological, snow and frozen-ground observations in the alpine region of the Heihe River Basin, China. *Earth System Science Data*, 11(3):1483–1499.

Chen, J., Liu, L., Zhang, T., Cao, B., and Lin, H. (2018). Using Persistent Scatterer Interferometry to Map and Quantify Permafrost Thaw Subsidence: A Case Study of Eboling Mountain on the Qinghai-Tibet Plateau. *Journal of Geophysical Research: Earth Surface*, 123(10):2663–2676.

Chen, Y., Yang, K., Qin, J., Cui, Q., Lu, H., La, Z., Han, M., and Tang, W. (2017). Evaluation of SMAP, SMOS, and AMSR2 soil moisture retrievals against observations from two networks on the Tibetan Plateau. *Journal of Geophysical Research*, 122(11):5780–5792.

Chen, Y., Yang, K., Qin, J., Zhao, L., Tang, W., and Han, M. (2013). Evaluation of AMSR-E retrievals and GLDAS simulations against observations of a soil moisture network on the central Tibetan Plateau. *Journal of Geophysical Research Atmospheres*, 118(10):4466–4475.

Chew, C., Lowe, S., Parazoo, N., Esterhuizen, S., Oveisgharan, S., Podest, E., Zuffada, C., and Freedman, A. (2017). SMAP radar receiver measures land surface freeze/thaw state through capture of forward-scattered L-band signals. *Remote Sensing of Environment*, 198:333–344.

Chew, C., Small, E. E., and Larson, K. M. (2016). An algorithm for soil moisture estimation using GPS-interferometric reflectometry for bare and vegetated soil. *GPS Solutions*, 20(3):525–537.

- Chew, C. C. and Small, E. E. (2018). Soil Moisture Sensing Using Spaceborne GNSS Reflections: Comparison of CYGNSS Reflectivity to SMAP Soil Moisture. *Geophysical Research Letters*, 45(9):4049–4057.
- Chew, C. C., Small, E. E., Larson, K. M., and Zavorotny, V. U. (2014). Effects of Near-Surface Soil Moisture on GPS SNR Data: Development of a Retrieval Algorithm for Soil Moisture. *IEEE Transactions on Geoscience and Remote Sensing*, 52(1):537–543.
- Chew, C. C., Small, E. E., Larson, K. M., and Zavorotny, V. U. (2015). Vegetation sensing using GPS-interferometric reflectometry: Theoretical effects of canopy parameters on signal-to-noise ratio data. *IEEE Transactions on Geoscience and Remote Sensing*, 53(5):2755–2764.
- Cosenza, P., Guérin, R., and Tabbagh, A. (2003). Relationship between thermal conductivity and water content of soils using numerical modelling. *European Journal of Soil Science*, 54(3):581–588.
- Cruickshank, J. (1971). Soils and Terrain Units Around Resolute, Cornwallis Island. *ARCTIC*, 24(3).
- Daout, S., Dini, B., Haeberli, W., Doin, M.-P., and Parsons, B. (2020). Ice loss in the Northeastern Tibetan Plateau permafrost as seen by 16 yr of ESA SAR missions. *Earth and Planetary Science Letters*, 545:116404.
- Dill, R. and Dobslaw, H. (2013). Numerical simulations of global-scale high-resolution hydrological crustal deformations. *Journal of Geophysical Research: Solid Earth*, 118(9):5008–5017.
- Dow, J. M., Neilan, R. E., and Rizos, C. (2009). The International GNSS Service in a changing landscape of Global Navigation Satellite Systems. *Journal of Geodesy*, 83(3-4):191–198.
- Dredge, L. A. (1994). Surficial geology, Repulse Bay-Hurd Channel, districts of Franklin and Keewatin, Northwest Territories. Technical report, Geological Survey of Canada.
- Eaton, D. W., Adams, J., Asudeh, I., Atkinson, G. M., Bostock, M. G., Cassidy, J. F., Ferguson, I. J., Samson, C., Snyder, D. B., Tiampo, K. F., and Unsworth, M. J. (2005). Investigating Canada's Lithosphere and earthquake hazards with portable arrays. *Eos, Transactions, American Geophysical Union*, 86(17):169–173.
- Ednie, M. and Smith, S. L. (2015). Permafrost temperature data 2008-2014 from community based monitoring sites in Nunavut. Technical report, Geological Survey of Canada.

- Entekhabi, D., Njoku, E. G., O'Neill, P. E., Kellogg, K. H., Crow, W. T., Edelstein, W. N., Entin, J. K., Goodman, S. D., Jackson, T. J., Johnson, J., Kimball, J., Piepmeier, J. R., Koster, R. D., Martin, N., McDonald, K. C., Moghaddam, M., Moran, S., Reichle, R., Shi, J. C., Spencer, M. W., Thurman, S. W., Tsang, L., and Van Zyl, J. (2010). The Soil Moisture Active Passive (SMAP) Mission. *Proceedings of the IEEE*, 98(5):704–716.
- Foti, G., Gommenginger, C., Jales, P., Unwin, M., Shaw, A., Robertson, C., and Roselló, J. (2015). Spaceborne GNSS reflectometry for ocean winds: First results from the UK TechDemoSat-1 mission. *Geophysical Research Letters*, 42(13):5435–5441.
- French, H. M. (2007). *The Periglacial Environment*. John Wiley & Sons Ltd., West Sussex, England.
- Gan, W., Zhang, P., Shen, Z.-K., Niu, Z., Wang, M., Wan, Y., Zhou, D., and Cheng, J. (2007). Present-day crustal motion within the Tibetan Plateau inferred from GPS measurements. *Journal of Geophysical Research*, 112(B8):B08416.
- Ge, S., McKenzie, J., Voss, C., and Wu, Q. (2011). Exchange of groundwater and surface-water mediated by permafrost response to seasonal and long term air temperature variation. *Geophysical Research Letters*, 38(14):n/a–n/a.
- Georgiadou, Y. and Kleusberg, A. (1988). On carrier signal multipath effects in relative GPS positioning. *manuscripta geodaetica*, 13:172–179.
- Gleason, S., Hodgart, S., Yiping Sun, Gommenginger, C., Mackin, S., Adjrad, M., and Unwin, M. (2005). Detection and Processing of bistatically reflected GPS signals from low Earth orbit for the purpose of ocean remote sensing. *IEEE Transactions on Geoscience and Remote Sensing*, 43(6):1229–1241.
- Göckede, M., Kwon, M. J., Kittler, F., Heimann, M., Zimov, N., and Zimov, S. (2019). Negative feedback processes following drainage slow down permafrost degradation. *Global Change Biology*, pages 0–3.
- Gruber, S. (2020). Ground subsidence and heave over permafrost: hourly time series reveal interannual, seasonal and shorter-term movement caused by freezing, thawing and water movement. *The Cryosphere*, 14(4):1437–1447.
- Hjort, J., Karjalainen, O., Aalto, J., Westermann, S., Romanovsky, V. E., Nelson, F. E., Etzelmüller, B., and Luoto, M. (2018). Degrading permafrost puts Arctic infrastructure at risk by mid-century. *Nature Communications*, 9(1):5147.
- Hu, Y., Liu, L., Larson, K. M., Schaefer, K. M., Zhang, J., and Yao, Y. (2018). GPS Interferometric Reflectometry Reveals Cyclic Elevation Changes in Thaw and Freezing Seasons in a Permafrost Area (Barrow, Alaska). *Geophysical Research Letters*, 45(11):5581–5589.

- Jayachandran, P. T., Langley, R. B., MacDougall, J. W., Mushini, S. C., Pokhotelov, D., Hamza, A. M., Mann, I. R., Milling, D. K., Kale, Z. C., Chadwick, R., Kelly, T., Danskin, D. W., and Carrano, C. S. (2009). Canadian High Arctic Ionospheric Network (CHAIN). *Radio Science*, 44(1):n/a–n/a.
- Jones, B. M., Grosse, G., Arp, C. D., Miller, E., Liu, L., Hayes, D. J., and Larsen, C. F. (2015). Recent Arctic tundra fire initiates widespread thermokarst development. *Scientific Reports*, 5(15865):1–13.
- Klene, A. E., Nelson, F. E., Shiklomanov, N. I., and Hinkel, K. M. (2001). The N-Factor in Natural Landscapes: Variability of Air and Soil-Surface Temperatures, Kuparuk River Basin, Alaska, U.S.A. *Arctic, Antarctic, and Alpine Research*, 33(2):140.
- Kokelj, S. V. and Jorgenson, M. T. (2013). Advances in Thermokarst Research. *Permafrost and Periglacial Processes*, 24(2):108–119.
- Lahaye, F., Collins, P., Héroux, P., Daniels, M., and Popelar, J. (2001). Using the Canadian Active Control System (CACS) for Real-Time Monitoring of GPS Receiver External Frequency Standards. In *Proceedings of the 14th International Technical Meeting of the Satellite Division of The Institute of Navigation (ION GPS 2001)*, pages 2220 – 2228, Salt Lake City, UT.
- Lantuit, H. and Pollard, W. H. (2008). Fifty years of coastal erosion and retrogressive thaw slump activity on Herschel Island, southern Beaufort Sea, Yukon Territory, Canada. *Geomorphology*, 95(1):84–102.
- Larson, K. M. (2016). GPS interferometric reflectometry: applications to surface soil moisture, snow depth, and vegetation water content in the western United States. *Wiley Interdisciplinary Reviews: Water*, 3(6):775–787.
- Larson, K. M. (2019). Unanticipated Uses of the Global Positioning System. *Annual Review of Earth and Planetary Sciences*, 47(1):19–40.
- Larson, K. M., Braun, J. J., Small, E. E., Zavorotny, V. U., Gutmann, E. D., and Bilich, A. L. (2010). GPS Multipath and Its Relation to Near-Surface Soil Moisture Content. *IEEE Journal of Selected Topics in Applied Earth Observations and Remote Sensing*, 3(1):91–99.
- Larson, K. M., Gutmann, E. D., Zavorotny, V. U., Braun, J. J., Williams, M. W., and Nievinski, F. G. (2009). Can we measure snow depth with GPS receivers? *Geophysical Research Letters*, 36(17):L17502.
- Larson, K. M., Ray, R. D., Nievinski, F. G., and Freymueller, J. T. (2013). The accidental tide gauge: A GPS reflection case study from kachemak bay, Alaska. *IEEE Geoscience and Remote Sensing Letters*, 10(5):1200–1204.

- Larson, K. M. and Small, E. E. (2014). Normalized microwave reflection index: A vegetation measurement derived from GPS networks. *IEEE Journal of Selected Topics in Applied Earth Observations and Remote Sensing*, 7(5):1501–1511.
- Larson, K. M., Small, E. E., Gutmann, E., Bilich, A., Axelrad, P., and Braun, J. (2008a). Using GPS multipath to measure soil moisture fluctuations: Initial results. *GPS Solutions*, 12(3):173–177.
- Larson, K. M., Small, E. E., Gutmann, E. D., Bilich, A. L., Braun, J. J., and Zavorotny, V. U. (2008b). Use of GPS receivers as a soil moisture network for water cycle studies. *Geophysical Research Letters*, 35(24):L24405.
- Lewkowicz, A. G. and Way, R. G. (2019). Extremes of summer climate trigger thousands of thermokarst landslides in a High Arctic environment. *Nature Communications*, 10(1):1329.
- Li, W., Cardellach, E., Fabra, F., Ribó, S., and Rius, A. (2018). Lake Level and Surface Topography Measured With Spaceborne GNSS-Reflectometry From CYGNSS Mission: Example for the Lake Qinghai. *Geophysical Research Letters*, 45(24).
- Li, W., Cardellach, E., Fabra, F., Rius, A., Ribó, S., and Martín-Neira, M. (2017). First spaceborne phase altimetry over sea ice using TechDemoSat-1 GNSS-R signals. *Geophysical Research Letters*, 44(16):8369–8376.
- Li, Y., Yan, S., and Ma, Q. (2021). Deformation measurement based on the phase of reflected signals of beidou geo satellites. In Yang, C. and Xie, J., editors, *China Satellite Navigation Conference (CSNC 2021) Proceedings*, pages 90–100, Singapore. Springer Singapore.
- Liang, S., Gan, W., Shen, C., Xiao, G., Liu, J., Chen, W., Ding, X., and Zhou, D. (2013). Three-dimensional velocity field of present-day crustal motion of the Tibetan Plateau derived from GPS measurements. *Journal of Geophysical Research: Solid Earth*, 118(10):5722–5732.
- Little, J. D., Sandall, H., Walegur, M. T., and Nelson, F. E. (2003). Application of differential global positioning systems to monitor frost heave and thaw settlement in Tundra environments. *Permafrost and Periglacial Processes*, 14(4):349–357.
- Liu, L., Jafarov, E. E., Schaefer, K. M., Jones, B. M., Zebker, H. A., Williams, C. A., Rogan, J., and Zhang, T. (2014a). InSAR detects increase in surface subsidence caused by an Arctic tundra fire. *Geophysical Research Letters*, 41(11):3906–3913.
- Liu, L. and Larson, K. M. (2018). Decadal changes of surface elevation over permafrost area estimated using reflected GPS signals. *The Cryosphere*, 12(2):477–489.

- Liu, L., Schaefer, K., Gusmeroli, A., Grosse, G., Jones, B. M., Zhang, T., Parsekian, A. D., and Zebker, H. A. (2014b). Seasonal thaw settlement at drained thermokarst lake basins, Arctic Alaska. *Cryosphere*, 8(3):815–826.
- Liu, L., Schaefer, K., Zhang, T., and Wahr, J. (2012). Estimating 1992-2000 average active layer thickness on the Alaskan North Slope from remotely sensed surface subsidence. *Journal of Geophysical Research: Earth Surface*, 117(F1):n/a–n/a.
- Liu, L., Schaefer, K. M., Chen, A. C., Gusmeroli, A., Zebker, H. A., and Zhang, T. (2015). Remote sensing measurements of thermokarst subsidence using InSAR. *Journal of Geophysical Research: Earth Surface*, 120(9):1935–1948.
- Liu, L., Zhang, T., and Wahr, J. (2010). InSAR measurements of surface deformation over permafrost on the North Slope of Alaska. *Journal of Geophysical Research: Earth Surface*, 115(F03023).
- Lomb, N. R. (1976). Least-squares frequency analysis of unequally spaced data. *Astrophysics and Space Science*, 39(2):447–462.
- Lowe, S. T., Zuffada, C., Chao, Y., Kroger, P., Young, L. E., and LaBrecque, J. L. (2002). 5-cm-Precision aircraft ocean altimetry using GPS reflections. *Geophysical Research Letters*, 29(10):13–1–13–4.
- Lu, S., Ren, T., Gong, Y., and Horton, R. (2007). An Improved Model for Predicting Soil Thermal Conductivity from Water Content at Room Temperature. *Soil Science Society of America Journal*, 71(1):8–14.
- Luo, J., Niu, F., Lin, Z., Liu, M., and Yin, G. (2019). Recent acceleration of thaw slumping in permafrost terrain of Qinghai-Tibet Plateau: An example from the Beiluhe Region. *Geomorphology*, 341:79–85.
- Ma, C., Li, X., Wei, L., and Wang, W. (2017). Multi-scale validation of SMAP soil moisture products over cold and arid regions in Northwestern China using distributed ground observation data. *Remote Sensing*, 9(4).
- Mackay, J. R. (1983). Downward water movement into frozen ground, western arctic coast, Canada. *Canadian Journal of Earth Sciences*, 20(1):120–134.
- Martin-Neira, M. (1993). A passive reflectometry and interferometry system (PARIS): application to ocean altimetry. *ESA Journal*, 17(4):331–355.
- Martin-Neira, M., Colmenarejo, P., Ruffini, G., and Serra, C. (2002). Altimetry precision of 1 cm over a pond using the wide-lane carrier phase of GPS reflected signals. *Canadian Journal of Remote Sensing*, 28(3):394–403.

- McCreight, J. L., Small, E. E., and Larson, K. M. (2014). Snow depth, density, and SWE estimates derived from GPS reflection data: Validation in the western U. S. *Water Resources Research*, 50(8):6892–6909.
- Mekonnen, Z. A., Riley, W. J., Grant, R. F., and Romanovsky, V. E. (2021). Changes in precipitation and air temperature contribute comparably to permafrost degradation in a warmer climate. *Environmental Research Letters*, 16(2):024008.
- Nelson, F. E., Anisimov, O. A., and Shiklomanov, N. I. (2002). Climate change and hazard zonation in the circum-arctic permafrost regions. *Natural Hazards*, 26(3):203–225.
- Nelson, F. E., Outcalt, S. I., Brown, J., Shiklomanov, N. I., and Hinkel, K. M. (1998). Spatial and Temporal Attributes of the Active-Layer Thickness Record, Barrow, Alaska, U.S.A. In *The 7th International Conference on Permafrost*, pages 797–802.
- Nievinski, F. G. (2013). *Forward and Inverse Modeling of GPS Multipath for Snow Monitoring*. PhD thesis, University of Colorado.
- Nievinski, F. G. and Larson, K. M. (2014). Forward modeling of GPS multipath for near-surface reflectometry and positioning applications. *GPS Solutions*, 18(2):309–322.
- O'Neill, H. B., Wolfe, S. A., and Duchesne, C. (2019). New ground ice maps for Canada using a paleogeographic modelling approach. *Cryosphere*, 13(3):753–773.
- Ran, Y., Li, X., and Cheng, G. (2018). Climate warming over the past half century has led to thermal degradation of permafrost on the Qinghai–Tibet Plateau. *The Cryosphere*, 12(2):595–608.
- Roesler, C. and Larson, K. M. (2018). Software tools for GNSS interferometric reflectometry (GNSS-IR). *GPS Solutions*, 22(3):80.
- Schuur, E. A. G., McGuire, A. D., Schädel, C., Grosse, G., Harden, J. W., Hayes, D. J., Hugelius, G., Koven, C. D., Kuhry, P., Lawrence, D. M., Natali, S. M., Olefeldt, D., Romanovsky, V. E., Schaefer, K., Turetsky, M. R., Treat, C. C., and Vonk, J. E. (2015). Climate change and the permafrost carbon feedback. *Nature*, 520(7546):171–179.
- Schwarz, G. E. and Alexander, R. B. (1995). State Soil Geographic (STATSGO) Data Base for the Conterminous United States. Technical report, U.S. Geological Survey.
- Seneviratne, S. I., Corti, T., Davin, E. L., Hirschi, M., Jaeger, E. B., Lehner, I., Orlowsky, B., and Teuling, A. J. (2010). Investigating soil moisture-climate interactions in a changing climate: A review. *Earth-Science Reviews*, 99(3-4):125–161.

Shiklomanov, N. I., Streletskiy, D. A., Little, J. D., and Nelson, F. E. (2013). Isotropic thaw subsidence in undisturbed permafrost landscapes. *Geophysical Research Letters*, 40(24):6356–6361.

Shiklomanov, N. I., Streletskiy, D. A., Nelson, F. E., Hollister, R. D., Romanovsky, V. E., Tweedie, C. E., Bockheim, J. G., and Brown, J. (2010). Decadal variations of active-layer thickness in moisture-controlled landscapes, Barrow, Alaska. *Journal of Geophysical Research*, 115(4):G00I04.

Shiklomanov, N. I., Streletskiy, D. A., Swales, T. B., and Kokorev, V. A. (2017). Climate Change and Stability of Urban Infrastructure in Russian Permafrost Regions: Prognostic Assessment based on GCM Climate Projections. *Geographical Review*, 107(1):125–142.

Shur, Y., Hinkel, K. M., and Nelson, F. E. (2005). The transient layer: implications for geocryology and climate-change science. *Permafrost and Periglacial Processes*, 16(1):5–17.

Shur, Y. L. and Jorgenson, M. T. (2007). Patterns of permafrost formation and degradation in relation to climate and ecosystems. *Permafrost and Periglacial Processes*, 18(1):7–19.

Sladen, W. E. (2011). permafrost. Technical report, Geological Survey of Canada.

Small, E. E., Larson, K. M., and Braun, J. J. (2010). Sensing vegetation growth with reflected GPS signals. *Geophysical Research Letters*, 37(12):n/a–n/a.

Smith, S. L., Riseborough, D. W., Ednie, M., and Chartrand, J. (2013). A map and summary database of permafrost temperatures in Nunavut, Canada. Technical report, Geological Survey of Canada.

Smith, S. L., Wolfe, S. A., Riseborough, D. W., and Nixon, F. M. (2009). Active-Layer Characteristics and Summer Climatic Indices, Mackenzie Valley, Northwest Territories, Canada. *Permafrost and Periglacial Processes*, 20:201–220.

Streletskiy, D. A., Shiklomanov, N. I., Little, J. D., Nelson, F. E., Brown, J., Nyland, K. E., and Klene, A. E. (2017). Thaw Subsidence in Undisturbed Tundra Landscapes, Barrow, Alaska, 1962–2015. *Permafrost and Periglacial Processes*, 28(3):566–572.

Streletskiy, D. A., Suter, L. J., Shiklomanov, N. I., Porfiriev, B. N., and Eliseev, D. O. (2019). Assessment of climate change impacts on buildings, structures and infrastructure in the Russian regions on permafrost. *Environmental Research Letters*, 14(2):025003.

- Taylor, A., Brown, R. J. E., Pilon, J., and Judge, A. S. (1982). Permafrost and the shallow thermal regime at Alert, N.W.T. In Proceedings of the Fourth Canadian permafrost conference, pages 12–22.
- Throop, J., Smith, S. L., and Lewkowicz, A. G. (2010). Observed recent changes in climate and permafrost temperatures at four sites in northern Canada. In 63rd Canadian Geotechnical Conference & 6th Canadian Permafrost Conference, pages 1265–1272.
- Treufaft, R. N., Lowe, S. T., Zuffada, C., and Chao, Y. (2001). 2-cm GPS altimetry over Crater Lake. Geophysical Research Letters, 28(23):4343–4346.
- Ulaby, F. and Long, D. (2015). Microwave radar and radiometric remote sensing. Artech House.
- Unwin, M., Gleason, S., and Brennan, M. (2003). The Space GPS Reflectometry Experiment on the UK Disaster Monitoring Constellation Satellite. In Proceedings of the 16th International Technical Meeting of the Satellite Division of The Institute of Navigation (ION GPS/GNSS 2003), page 2656.
- Vasiliev, A. A., Drozdov, D. S., Gravis, A. G., Malkova, G. V., Nyland, K. E., and Streletsckiy, D. A. (2020). Permafrost degradation in the Western Russian Arctic. Environmental Research Letters, 15(4):045001.
- Walker, A. E. and Silis, A. (2002). Snow-cover variations over the Mackenzie River basin, Canada, derived from SSM/I passive-microwave satellite data. Annals of Glaciology, 34:8–14.
- Walvoord, M. A. and Kurylyk, B. L. (2016). Hydrologic Impacts of Thawing Permafrost —A Review. Vadose Zone Journal, 15(6):0.
- Wang, K., Jafarov, E., and Overeem, I. (2020). Sensitivity evaluation of the Kudryavtsev permafrost model. Science of The Total Environment, 720:137538.
- Woo, M.-k. (2012). Permafrost Hydrology. Springer, Berlin, Heidelberg.
- Wu, Q., Hou, Y., Yun, H., and Liu, Y. (2015). Changes in active-layer thickness and near-surface permafrost between 2002 and 2012 in alpine ecosystems, Qinghai-Xizang (Tibet) Plateau, China. Global and Planetary Change, 124:149–155.
- Yang, Y., Zheng, Y., Yu, W., Chen, W., and Weng, D. (2019). Deformation monitoring using GNSS-R technology. Advances in Space Research, 63(10):3303–3314.

- Zavorotny, V. U., Larson, K. M., Braun, J. J., Small, E. E., Gutmann, E. D., and Bilich, A. L. (2010). A Physical Model for GPS Multipath Caused by Land Reflections: Toward Bare Soil Moisture Retrievals. *IEEE Journal of Selected Topics in Applied Earth Observations and Remote Sensing*, 3(1):100–110.
- Zhang, G., Nan, Z., Zhao, L., Liang, Y., and Cheng, G. (2021a). Qinghai-Tibet Plateau wetting reduces permafrost thermal responses to climate warming. *Earth and Planetary Science Letters*, 562:116858.
- Zhang, J. and Liu, L. (2020). Reflector heights in the Arctic permafrost areas measured by GNSS interferometric reflectometry. *Zenodo*.
- Zhang, J. and Liu, L. (2021). Mining noise data for monitoring Arctic permafrost by using GNSS interferometric reflectometry. *Polar Science*, page 100649.
- Zhang, J., Liu, L., and Hu, Y. (2020). Global Positioning System interferometric reflectometry (GPS-IR) measurements of ground surface elevation changes in permafrost areas in northern Canada. *The Cryosphere*, 14(6):1875–1888.
- Zhang, J., Liu, L., Su, L., and Che, T. (2021b). Three in one: GPS-IR measurements of ground surface elevation changes, soil moisture, and snow depth at a permafrost site in the northeastern Qinghai–Tibet Plateau. *The Cryosphere*, 15(6):3021–3033.
- Zhang, L., He, C., and Zhang, M. (2017a). Multi-scale evaluation of the SMAP product using sparse in-situ network over a high mountainous Watershed, Northwest China. *Remote Sensing*, 9(11).
- Zhang, S., Roussel, N., Boniface, K., Ha, M. C., Frappart, F., Darrozes, J., Baup, F., and Calvet, J.-C. (2017b). Use of reflected GNSS SNR data to retrieve either soil moisture or vegetation height from a wheat crop. *Hydrology and Earth System Sciences*, 21(9):4767–4784.
- Zhang, T., Barry, R. G., Knowles, K., Ling, F., and Armstrong, R. L. (2003). Distribution of seasonally and perennially frozen ground in the Northern Hemisphere. In *Proceedings of the 8th International Conference on Permafrost*, pages 1289–1294.
- Zhao, L., Zou, D., Hu, G., Du, E., Pang, Q., Xiao, Y., Li, R., Sheng, Y., Wu, X., Sun, Z., Wang, L., Wang, C., Ma, L., Zhou, H., and Liu, S. (2020). Changing climate and the permafrost environment on the Qinghai–Tibet (Xizang) plateau. *Permafrost and Periglacial Processes*, 31(3):396–405.
- Zwieback, S. and Berg, A. A. (2019). Fine-Scale SAR Soil Moisture Estimation in the Subarctic Tundra. *IEEE Transactions on Geoscience and Remote Sensing*, 57(7):4898–4912.

Zwieback, S., Kokelj, S. V., Günther, F., Boike, J., Grosse, G., and Hajnsek, I. (2018). Sub-seasonal thaw slump mass wasting is not consistently energy limited at the landscape scale. *The Cryosphere*, 12(2):549–564.

Zwieback, S., Liu, X., Antonova, S., Heim, B., Bartsch, A., Boike, J., and Hajnsek, I. (2016). A Statistical Test of Phase Closure to Detect Influences on DInSAR Deformation Estimates Besides Displacements and Decorrelation Noise: Two Case Studies in High-Latitude Regions. *IEEE Transactions on Geoscience and Remote Sensing*, 54(9):5588–5601.